UNIVERSITEIT VAN PRETORIA
UNIVERSITY OF PRETORIA
YUNIBESITHI YA PRETORIA

PROPERTIES OF GRAPHITIC COMPOSITES

by

PHILEMON PODILE MAGAMPA

Submitted in partial fulfilment of the requirements for the degree

DOCTOR OF PHILOSOPHY

Department of Chemistry
In the Faculty of Natural and Agricultural Sciences
University of Pretoria
Pretoria

2013

DECLARATION

I, Philemon Podile Magampa declare that the thesis/dissertation, which I hereby submit for the degree Doctor of Philosophy in Chemistry at the University of Pretoria, is my own original work and has not previously been submitted by me for a degree at this or any other tertiary institution.

SIGNED ON THIS……..DAY OF MAY2013

Philemon Podile Magampa (Student)

……

Prof. Ncholu Manyala (Supervisor)

…….

Prof. Walter Focke (Co-Supervisor)

…….

ABSTRACT

The Pebble Bed Modular Reactor (PBMR) is a high temperature graphite-moderated nuclear reactor that uses helium as a coolant. The triple coated (TRISO) particles contain enriched uranium oxide fuel which is coated with layers of various forms of pyrolytic carbon and silicon carbide. The TRISO particles are further embedded in the matrix of spherical graphite pebbles. The graphite matrix is a composite moulded from a compound containing natural flake graphite (64 wt.%), synthetic graphite (16 wt.%) and a phenolic resin binder (20 wt.%) heated to 1800 °C in inert atmosphere. The graphitic composite provides structural integrity, encasement and act as a moderator material. In this work, low density model graphite composites similar to those used in nuclear applications as encasement material in fuel pebbles were made by uniaxial cold compression moulding. The graphitic composites contained various ratios of natural flake graphite and synthetic graphite at fixed phenolic novolac resin binder content of 20 wt.% (green state). The fabrication process employed entails mixing the graphite powders, followed by addition of methanol phenolic resin solution to the graphite powder mix, drying, grinding, milling and sieving; and finally compression moulding in a stainless steel die at 13 MPa using a hydraulic press. The green moulded disc specimens were then carbonized at 900 °C in nitrogen atmosphere to remove volatiles followed by annealing at 1800 °C in helium atmosphere. The annealing step diminishes structural defects and result in densification of the composites.

The microstructure of fabricated graphitic composites was characterized using various techniques. Particle Size Distributions determined using Laser diffraction showed that the inclusion of the binder leads to agglomeration. The composite powders had larger mean particle sizes than the raw graphite powders showing the binding effect of the novolac phenolic resin. X-

ray diffraction studies showed that the graphitic composites had a hexagonal crystal structure after annealing. Raman spectroscopy revealed the presence of the structurally disordered phase derived from the resin carbon (indicated by the pronounced D-band in the Raman spectra). XRD and Raman observations were consistent with literature and gave results supporting existing knowledge base. Optical microscopy revealed a flake-like microstructure for composites containing natural graphite and needle-coke like particles for composites containing mainly synthetic graphite. Optical microscopy confirmed that the effect of the manufacturing route employed here was to align the particles in the direction perpendicular to the compression moulding direction. As a result, the graphitic composites exhibited anisotropic property behavior.

The bulk density of the composites increased with the increase in the natural graphite content due to compactability of natural flakes in the manufacturing route. Thermogravimetric analysis studies on the composites showed that they were stable in air to 650 °C. Composites containing mainly synthetic graphite were thermally more stable in air compared to their natural graphite counterparts. The linear coefficients of thermal expansion of the composites were measured using thermomechanical analysis (20-600 °C). In the moulding direction, the average CTE (α_P) values were in the range (5-9) × 10^{-6} K^{-1} and increased with increment in the natural graphite content in the composite. In the direction perpendicular to moulding direction, the average CTE (α_N) values were in the range (1.7-2.1) × 10^{-6} K^{-1} showing that the expansion was similar or constant in this direction. Therefore an anisotropic expansion ratio, i.e. α_P:α_N, of about 3 was observed in the composites. This anisotropy is attributable to the alignment of the filler particles in the manufacturing route. The thermal conductivity of the annealed composites were measured in the pressing direction from 100 to 1000 °C and the values ranged from 19 to 30 W m^{-1} K^{-1}. Anisotropy was also observed as far as strength was concerned. A composite containing

64:16:20 wt.% ratio had the best mechanical properties, high thermal conductivity and slightly high expansion coefficient. This work demonstrates the complimentary properties of the graphite fillers in the composites. It also reports for the first time, data on the effect of variation of the filler graphites on microstructure and properties of model low density compression moulded graphitic composites.

ACKNOWLEDGEMENTS

I would like to thank the following people and organizations of which without their contribution this project would not have been successful:

- My supervisor Prof. Ncholu Manyala for his continued guidance, patience, support and invaluable inputs in this work. I really appreciate what you have done for me and many thanks.
- My co-supervisor Prof. Walter Focke, your contribution in this work is much appreciated.
- The contribution by my fellow Carbon Chair students is highly appreciated especially the discussions we had during our presentations.
- SARChI Chair in Carbon Materials and Technology of the Department of Science and Technology, Republic of South Africa for funding this project.
- I would also like to thank PBMR for provision of samples and financial assistance for my studies.
- Suzette Seymore for her continued hard work with the administrative aspects of all our projects in the group, you are like a mother to all of us and thank you very much. Mr Rainer Schumacher and Mrs Isbe van der Weistuizen for their technical assistance with repairing, assembling and running all instrumentation used in this work. Rainer you are a shining star!!!
- Mr. Tshepo Ntsoane (NECSA) for assisting with XRD measurements, Dr. Linda Prinsloo (UP) for assisting with Raman measurements and Mr. Bruce Berger (CSIR) for assistance in running thermal conductivity measurements.

- I would be mistaken not to acknowledge the unwavering support I got from my family and friends throughout the entire course of this challenging project. Special thanks to my wife in the making Ms. Chalot Mmatholo Matsepe; you are a blessing to me and our two lovely kids, Oratile and Letago.
- Above all I would like to thank God almighty le badimo baeshu for protecting and giving me strength throughout the years.

CONTRIBUTIONS

Part of this work was published in a peer-reviewed journal and another part presented at the international conferences as follows:

- **Magampa**, **P.P.**, Manyala, N. and Focke, W. W., 2013, 'Properties of graphitic composites based on natural and synthetic graphite powders and novolac phenolic resin binder', *Journal of Nuclear Materials*, 436 (1-3), 76-83. http://dx.doi.org/10.1016/j.jnucmat.2013.01.315
- **P. Magampa**, N. Manyala and W. Focke, Microstructural characterisation and thermal properties of model high temperature reactor graphite composites, *Oral presentation* at the 3rd Energy Post-Graduate conference, i-Themba Labs, Cape Town, South Africa, 11th-14th August 2013.
- **P. P. Magampa**, W.W. Focke and N. Manyala, Fabrication, microstructure and thermal properties of HTR graphite composites, A *poster presentation* at the 11th ICFPAM conference, University of Pretoria, South Africa, 22nd-27th May 201.
- **P. P. Magampa**, C. Melane, N. Manyala and W.W. Focke, Microstructural characterisation of the graphite composite comprising the HTR fuel matrix, *Oral presentation* at the annual world conference on carbon 2009, Biarritz, France, 14th-19th June 2009.

DEDICATION

In loving memory of my late elder sister, Motsanape Portia Nthama Magampa, may her soul rest in peace. We as a family know you are in a safe and peaceful place. We miss you very much:

Tlou ya mmaselemela,

Tlou ye e tswago sephaku le sephakwana,

Ye e tswago mabje-maramaga,

Mabje magolo ka mabedi,

Mpedi ya seja-serema. MminaTlou

TABLE OF CONTENTS

LIST OF SYMBOLS AND ABBREVIATIONS

Å : Angstroms

d_{hkl} : Spacing between diffracting (hkl) planes

c : The lattice constant of the hexagonal graphite unit cell

p : The degree of randomness in the alignment of layers in a graphitic material

α_p : The linear coefficient of thermal expansion in the compression moulding direction

α_N : The linear coefficient of thermal expansion in the normal to compression moulding direction

λ : The wavelength of the incident radiation source used

θ : The incident beam angle in degrees

n : Order of reflection

g : The degree of graphitisation

L_c : The out of plane crystallite size of a graphitic material

L_a : The in-plane crystallite size of a graphitic material

L_0 : The initial length of the sample at some initial temperature, T_0

ß : The peak-width at half maximum intensity

K : The shape factor of the peak

1λ plate or tint: a retarder plate used to polarize light in the optical microscope

V_e : Volume of an empty expansion chamber in a helium pycnometer

V_c : Volume of a sample-containing chamber in a helium pycnometer

V_s : Volume of the sample

V_t : Total volume after displacement of the sample

V_o : The baseline volume (or zero volume)

P_1 : Absolute pressure inside the helium pycnometer

P_2 : Helium pressure in the empty chamber

T_g : Glass transition temperature

α : Thermal diffusivity in $m^2.s^{-1}$

d : The thickness of the sample in metres.

$t_{1/2}$: Time required for the pulse to reach half its maximum value

ρ : Density of the sample in $g.cm^{-3}$

C_p : Specific heat of the sample at constant pressure in $J.\ kg^{-1}.K^{-1}$

κ : Thermal conductivity of the sample in $W.m^{-1}K^{-1}$

σ : Flexural strength in Pa or MPa

σ_P : The flexural strength in the compression moulding direction

σ_N : The flexural strength in the direction perpendicular to compression moulding direction

F : Applied load at fracture in Newtons

L : Support span length in metres or length of the sample in metres where applicable

b : Sample width in metres

L_i : Load span length in metres

h_t : total height after displacement

h_0 : the baseline height

ρ_B : Bulk density in $g.cm^{-3}$

ρ_{He} : Helium density in $g.cm^{-3}$

T : Temperature in Kelvin

I_D : The intensity of the Raman D-peak

I_G : The intensity of the Raman G-peak

T_i : The onset air oxidation temperature in °C

T_e : The endset air oxidation temperature in °C

T_m : The temperature at which the sample losses maximum weight

E_P : The flexural modulus in the compression moulding direction

E_N : The flexural modulus in the direction perpendicular to compression moulding direction

TRISO : Triple coated particles containing enriched uranium oxide fuel

PBMR : The Pebble Bed Modular Reactor

NG : Natural flake graphite

SG : Synthetic or Electro graphite

Novolac : Phenolic novolac binder resin

HTRs : High Temperature Reactors

AVR : Arbeitsgemeinscharf Versuchs-Reaktor

THTR : Thorium High Temperature Reactor

XRD : X-ray diffraction

OM : Optical microscopy

SEM : Scanning electron microscopy

TGA : Thermogravimetric analysis

TMA : Thermomechanical analysis

IUPAC : International Union of Pure and Applied Chemistry

CTE, α : The linear coefficient of thermal expansion in K^{-1}.

HOPG : Highly oriented pyrolytic graphite

SWNT : Single-walled carbon nanotubes

RBM : Radial Breathing Modes

SE : Secondary electrons

BSE : Backscattered electrons

PC : Personal Computer

LVDT : Linear Variable Displacement Transducer

ASTM : American Standard Test Method

CCD : Charge-coupled device

ICDD : International Centre for Diffraction Data

LIST OF FIGURES

LIST OF TABLES

CHAPTER 1: INTRODUCTION

1.1. Background

The Pebble Bed Modular Reactor is a high temperature graphite-moderated nuclear reactor that uses helium as a coolant. The triple coated (TRISO) particles contain enriched uranium oxide fuel. The coatings, see Figure 1.1, comprise layers of various forms of pyrolytic carbon and silicon carbide (Nicholls, 2001, Nicholls, 2002). They are designed to retain any fission products released at the elevated reactor operating temperatures (Tang et al., 2002, Zhao et al., 2006).

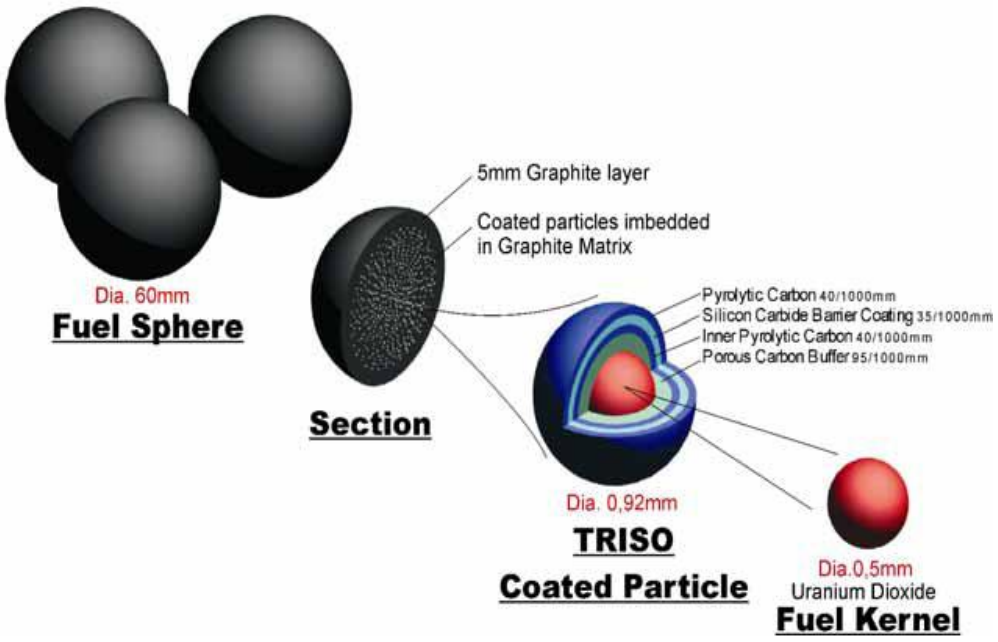

Figure 1.1: Schematic representation of the components of a fuel sphere encasing TRISO coated fuel kernel, i.e. UO_2 (Nicholls, 2002).

Large numbers of the TRISO particles are embedded in the matrix of each of the spherical graphite pebbles. These graphite composites are isostatically moulded from a compound

containing natural flake graphite (64 wt.%), synthetic graphite (16 wt.%) and a phenolic resin binder (20 wt.%). The moulded spheres are heat-treated to 1800 °C to convert the binder into a glassy carbon. This gives a strong material that provides structural integrity. It also acts as a moderator material, slowing down the speed of neutrons to thermal levels so that the fission reactions can occur. The graphite composite must possess suitable properties for this function. For example, it must possess very low impurity levels, density exceeding 1.7 g cm^{-3}, high thermal conductivity, high mechanical strength, high stability under irradiation, high oxidation resistance and low thermal expansion coefficient (Cohn et al., 2005)

Similar compositions have been used in other high temperature reactors (Zhao et al., 2006) and were judged to provide the required properties. However, little was reported in literature about the relationship between the processing method, the resulting microstructure and the final properties that can be achieved. For example, what is the microstructure of the composites? What is the spatial arrangement of the graphite fillers? What is the effect of changing the relative proportions of graphite fillers in the matrix? How are properties affected when lower density materials are fabricated? Therefore this work aims to address most of these questions.

1.2. Aims and objectives of the project

- To make fuel-free low-density model graphitic composites containing natural flake graphite (NG), synthetic graphite (SG) and a novolac phenolic resin binder by uniaxial compression moulding. To do a systematic study by varying the relative proportions of the filler raw graphites in the composites at fixed (i.e. 20 wt.%) phenolic resin binder content.

- To study the effect of changing the relative proportions of the filler graphite powders in the composites on the microstructure and properties.
- To study the microstructure of the graphite composites made using X-ray diffraction (XRD), Raman Spectroscopy, optical microscopy (OM) and scanning electron microscopy (SEM). The open porosity of these materials was measured using pycnometry.
- The thermal properties of the graphitic composites such as air oxidative stability, linear thermal expansion coefficients and thermal conductivity were measured using thermogravimetric analysis (TGA), thermomechanical analysis (TMA) and Xenon flash photolysis, respectively.
- The mechanical properties such as flexural strength and flexural modulus were measured using four-point bend loading tests.
- The main objective of this work is to understand how the microstructure changes with variation of the filler graphites in the composites and consequently, properties.

The next chapter discusses the crystalline forms of carbon of which graphite is one of them, how graphite materials are made, the graphitisation process, factors affecting graphitisation and the importance of graphite in nuclear industry.

References

COHN, J. G., STERN, E. W. & ETRIS, S. F. (2005) Graphite, Artificial IN KIRK-OTHMER (Ed.) *Kirk-Othmer Encyclopedia of Chemical Technology*. 5 ed., John Wiley & Sons.

NICHOLLS, D. R. (2001) The Pebble Bed Modular Reactor. *Transactions of the Royal Society of South Africa,* 56**,** 125-130.

NICHOLLS, D. R. (2002) The Pebble Bed Modular Reactor. *South African Journal of Science,* 98**,** 31-35.

TANG, C. H., TANG, Y., ZHU, J. G., ZOU, Y. W., LI, J. O. & NI, X. O. (2002) Design and manufacture of the fuel element for 10 MW high temperature gas-cooled reactor. *Nuclear Engineering and Design,* 218**,** 91-102.

ZHAO, H. S., LIANG, T. X., ZHANG, J., HE, J., ZOU, Y. W. & TANG, C. H. (2006) Manufacture and characteristics of spherical fuel elements for the HTR-10. *Nuclear Engineering and Design,* 236**,** 643-647.

CHAPTER 2: REVIEW ON GRAPHITE

Different graphites have distinct properties depending on their end applications; for instance, moderator graphite used for nuclear applications must contain a uniform coefficient of thermal expansion in both the a- and c-crystallographic directions as well as low boron content. This chapter discusses the crystalline forms of carbon, how graphite materials are made, the graphitisation process, factors affecting this process and the importance of graphite in nuclear industry. The graphitisation process refers to the rearrangement of carbon atoms within its matrix due to heat-treatment in inert atmosphere leading to the formation of a structure close to that of the hexagonal graphite lattice. The quality of the graphite produced depends on the quality and purity of the starting precursor or organic compound. This process depends on various factors such as heat-treatment temperature, soaking time, the type of additives used in the starting material and the kind of heteroatoms present in the carbon matrix (e.g. B, N, S or O).

2.1 Crystalline forms of carbon

Graphite, diamond and fullerenes are the crystalline forms of carbon. Diamond is a metastable crystalline form having a face-centered cubic lattice with a side 3.567 Å and interatomic distance of 1.54 Å. Diamond can be transformed to graphite by heat-treatment. Graphite is a stable crystalline form of carbon and has two polytypes, the 2H and 3H forms corresponding to the hexagonal and rhombohedral forms, respectively (see Figure 2.1). The hexagonal form is the more stable and corresponds to the hexagonal ABAB stacking as first proposed by Hull (Hull, 1917) and reported by Kelly (Kelly, 1981a). The perfect graphite lattice has a stack of parallel hexagonal planes with the interatomic distance of 1.42 Å within the layers and the interlayer

spacing of 3.35 Å. This lattice has a hexagonal unit cell containing four atoms in plane. It is interesting to note that although diamond is the hardest material known, the bond length between the carbon atoms in diamond, i.e. 1.54 Å, is longer than the in plane bond length between the carbon atoms in graphite having bond length 1.42 Å, indicating weaker directional bond strength.

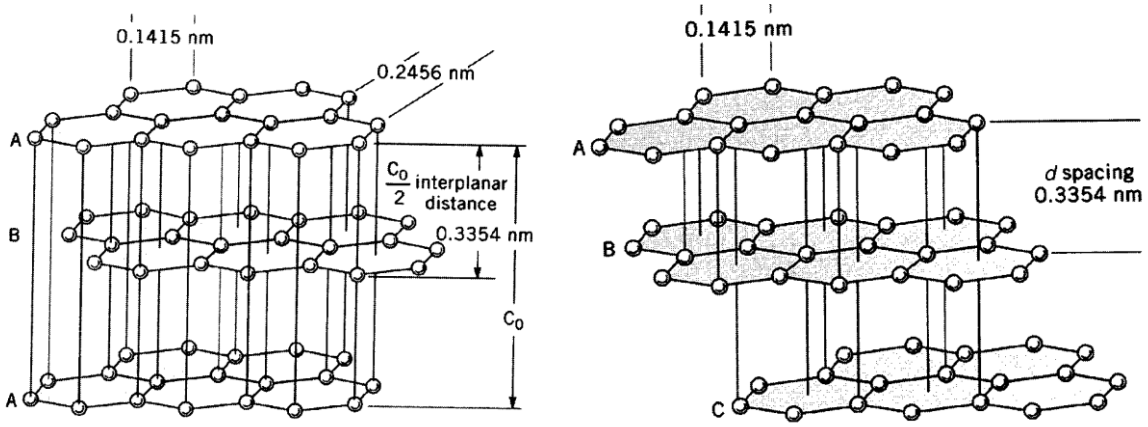

(a) (b)

Figure 2.1: The structure of graphite hexagonal (a) and rhombohedral (b) forms (Cohn et al., 2005, Kirk-Othmer, 2005, Edwards, 1989).

Various authors have reported a number of faint X-ray diffraction (XRD) lines which could not be accounted for by the hexagonal crystal structure (Laidler and Taylor, 1940, Lipson and Stokes, 1942b, Bacon, 1950a, Jagodzinski, 1949). These diffraction lines inferred a structure with a unit cell containing six atoms with an ABCABC… stacking sequence corresponding to the rhombohedral crystal structure. The occurrence of the rhombohedral crystal structure in samples of natural graphite from different origins has been reported (Lipson and Stokes, 1942a). This study concluded that the rhombohedral crystal structure accounts for faint lines observed in their X-ray patterns. The rhombohedral formed about 14 % of the usual hexagonal form in these natural graphites.

Analysis of the well-crystallized Ceylon graphite samples, one artificial and the other natural, which were ground, sieved and extruded, resulted in X-ray photographs showing samples having 17-22 % of the rhombohedral phase (Bacon, 1950a). This is in support of studies by Lipton and Stokes. On the other hand, on examination of single crystals of a graphite with a mosaic structure it was found that the rhombohedral phase is much less than the 14 % reported by Lipson and Stokes (Jagodzinski, 1949). This rhombohedral phase was also observed by electron diffraction studies on single graphite crystals in which case the proportion of this phase was 5 % (Hoerni, 1949). It is worth mentioning that the rhombohedral crystalline form is metastable and can be converted to a stable hexagonal crystalline form upon heat-treatment to 2000 °C (Kelly, 1981a). The rhombohedral phase is formed by damage to the hexagonal phase such as grinding, milling, etc.

There are many other carbon allotropes such as fullerenes (Kroto et al., 1985), carbon nanotubes (Iijima, 1991) graphene (Novoselov et al., 2004) (Geim and Novoselov, March 2007), carbon nanospheres (Miao et al., 2004), etc which possess different structures and properties. These materials are not discussed here in full since the focus of this work is in mainly on bulk graphite.

2.2 Graphite manufacture

Natural graphites are minerals that form when carbonaceous rocks undergo natural heating by geothermal gradient. These minerals are found in many parts of the world including Zimbabwe, China, India, Brazil and Sri Lanka. Natural graphites from different origins possess variable degrees of crystallinity (Bacon, 1950b). The properties of natural graphites depend mostly on their origins among other factors such as crushing, milling and purification steps employed during their processing. On the other hand, pyrolysis of suitable organic matter under inert gas flow, at a temperature up to 3200 °C, produces synthetic graphites. The properties of the

synthetic graphite depend on many factors and to understand these factors one must comprehend how these materials are made. The general manufacturing steps of synthetic graphite are shown in Figure 2.2.

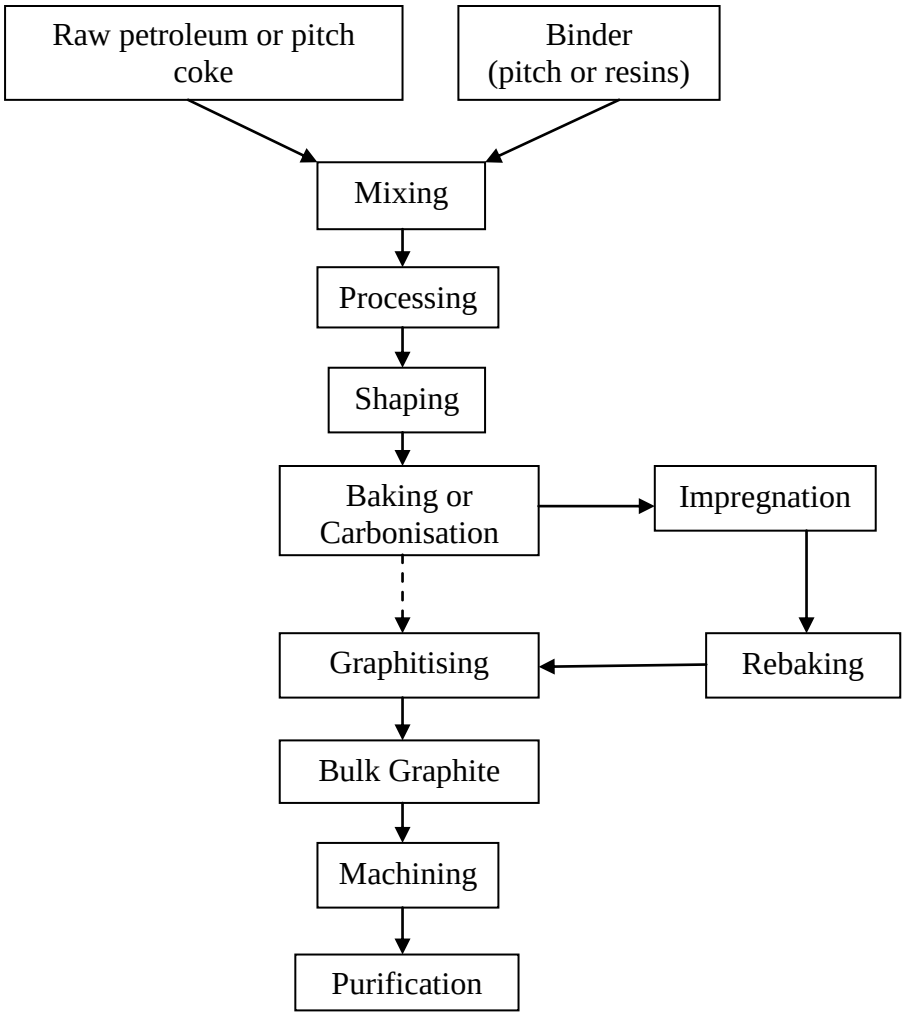

Figure 2.2: Synthetic graphite general manufacturing steps (Wolf, 2001).

Firstly, a raw filler material usually a petroleum or pitch cokes are mixed with a binder (usually a pitch or synthetic resin). The main function of the binder is to wet and plasticise the filler particles so that they can be formed into the required shape. The mixing step is followed by

processing step which involves drying, crushing, milling and sieving of the coke-binder mixture. Thereafter the powdered material is shaped either by die moulding, isostatic moulding or extrusion. The green artefact or mold is then subjected to heat treatment in inert atmosphere in the temperature range 600-1500 °C to carbonise or bake the green artefact. This step removes the volatiles (mainly CO, CO_2, CH_4, H_2) in the green artefact and transforms the binder into coke. Thereafter the carbonised material is either graphitised by heating the baked carbon material to a temperature between 2800 and 3200 °C in inert atmosphere or the baked carbon is impregnated with the binder and rebaked before it is graphitised. The impregnation step is usually performed in order to densify the baked carbon. After graphitisation, the bulk graphite can be machined and purified depending on its end application (Wolf, 2001). The graphites are in general shaped by extrusion, compression moulding and isostatic moulding.

Factors affecting the type and properties of the bulk graphite formed include (but not limited to):

- The choice of the raw material, which depends on end application
- The grain size distribution and grain shape of the coke raw material
- The carbon yield, wetting and viscosity of the binder
- The temperature, time and torque used during mixing
- The grain size distribution, apparent weight and pourability desired during processing
- The type of shaping used
- The homogeneity of pore size distribution after graphitisation, maximum graphitisation temperature used, heating rates, holding times and inert atmosphere used (Wolf, 2001).

2.3 The graphitisation process

According to the IUPAC definition graphitisation refers to the transformation in the solid state of thermodynamically unstable carbon into graphite by heat-treatment (Fitzer et al., 1995). This process is simply a progressive 3D ordering of the carbon layers upon heat-treatment of an organic precursor in an inert atmosphere. Initially, graphitisation was thought to occur by growth of small layers of carbon black by migration of carbon atoms from one layer to another forming new layer with sizes up to 100 Å but this incorrect model was overwritten by the one in which larger layers, > 100 Å, are already present in the material and graphitisation is mainly the annealing out of defects at low temperature (Houska and Warren, 1954).

In order to understand the graphitisation process, it is essential to understand the structure of unheated carbon. Warren and Gringriich have shown using X-ray diffraction that carbon black consists of aromatic layers in which the distribution of neighbouring carbon atoms in these layers was exactly the same as that of single layer of the graphite structure (Warren and Gringriich, 1934). It is worth realizing that at that time carbon black was considered completely amorphous. The concept of turbostratic order for graphitic carbons was introduced to describe the stacking arrangement of the basal planes in cokes heated to different temperatures(Biscoe and Warren, 1942). At low heat-treatment temperature, e.g. 1000 °C, the coke exhibits ‘turbostratic’ structure (i.e. random rotation of the layers around the c-axis giving no stacking sequence and hence larger interlayer spacings) with an interplanar spacing approaching 3.44 Å. This structure is 2-dimesional and the XRD profile only shows (*00l*) lines and (*hk*) lines ($h,k \neq 0$).

The concept of turbostratic order is very important and was used by Franklin to describe thermal evolution of different precursors heat-treated between 1000 and 3000 °C (Franklin, 1951a,

Franklin, 1951b). From this work, she was able to categorise these precursors into three groups, viz. graphitisable, partially graphitisable and non-graphitisable carbons.

2.2.1 Graphitising carbons

These are non-graphitic carbons by nature but when heat-treated sufficiently to high temperature, say 2600 °C, in inert conditions are converted to crystalline graphite. The organic precursors or parent material were subsequently shown to pass through a liquid crystal stage called mesophase during carbonisation (Brooks and Taylor, 1965). This is the key step in the formation of graphitic carbons in the condensed state. These carbons show a change from the turbostratic structure to a structure close to the one for ordered hexagonal crystalline graphite. However there are carbon precursors such as pyrolytic carbon which are graphitisable but do not go through the liquid crystal phase.

2.2.2 Non-graphitising carbons

On the other hand, the carbons which do not convert to graphitic carbon even when heated to high temperature are called non-graphitising. The key factor causing this behaviour is that the parent materials do not pass through a mesophase on carbonisation. Only small molecules are lost by degradation during their carbonisation causing formation of cross-links which inhibit fusion. The partially graphitisable carbons are the intermediate between the two extremes. The models representing crystalline arrangement in these categories of carbons structures are shown in Figure 2.2. Franklin has established the basis of graphitisation using XRD. She established a relationship between the basal interlayer spacing between the 002 layers, d_{002} and the lattice constant of the hexagonal graphite unit cell, c as follows:

$$d_{002} = \frac{|c|}{2} \qquad (2.1)$$

The value of c = 6.71 Å. During graphitisation of the organic precursor, the value of the basal interlayer spacing, d_{002} decreases progressively from 3.44 Å (turbostratic structure value) to 3.35 Å (graphite value). The interlayer spacing, $d_{002}$is also a measure of degree of ordering in a graphitic material and is related to the degree of randomness in the alignment of layers, p as follows (Franklin, 1951b):

$$d_{002} = 3.440 - 0.086(1 - p^2) \qquad (2.2)$$

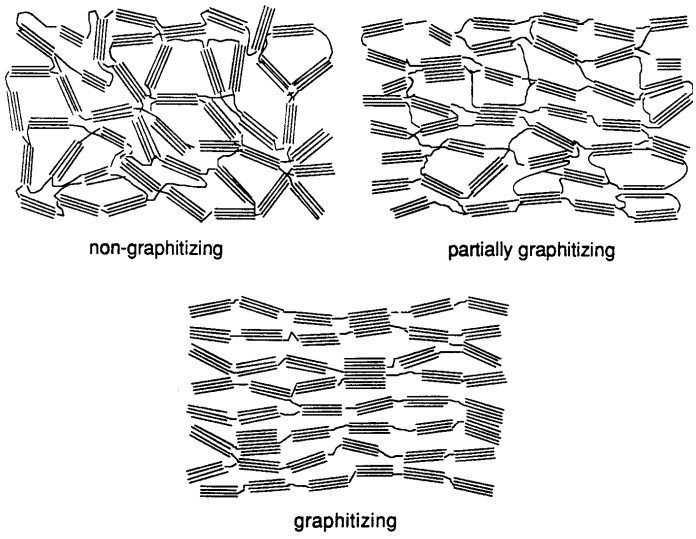

Figure 2.3: Franklin models of graphitising and non-graphitising carbon structures (Franklin, 1951b).

One must emphasize that the difference between the graphitising and non-graphitising carbons is that the latter show 2 dimensional structures in addition to the (*00l*) bands while the graphitising carbons exhibit a 3 dimensional structure. The process of graphitisation is affected by many factors of which some are discussed in the next section.

2.3 Factors affecting graphitisation

There are several factors which affect graphitisation of a pre-carbon; these include whether or not the organic precursor passes through mesophase and then a fusion state during carbonisation, heat-treatment temperature, soaking time at particular heat-treatment temperature, the kind of heteroatoms present in the carbon matrix (e.g. N, B, O or S) and/or the type of additives used in the starting material. The use of metal catalysts has proved vital for graphitisation as well.

2.3.1 Mesophase formation

When some organic precursors such as naphthalene, polyvinyl chloride, petroleum bitumen, etc are heated they melt and become an isotropic pitch-like material in plastic or liquid form and with increase in temperature spheres appear when they are observed under optical light microscope (Brooks and Taylor, 1965). With increase in temperature and soaking time, spheres become larger. This is the intermediate stage in the development of the characteristic anisotropic mosaic structure observed when some organic precursors are pyrolysed and is called mesophase. The mesophase was observed in the temperature range 400-520 °C depending on the starting organic precursor. As discussed in Section 2.2.1, mesophase formation is a key step in the formation of graphitising carbons in the condensed state. As the temperature is raised or soaking time at particular temperature is increased, the spheres grow larger (the pitch-like material

diminishes) and then start to touch each other or coalesce and begin to form ‘mosaic’ structure. After coalescence of the spheres, the mesophase solidifies into a semi-coke (Brooks and Taylor, 1965). This semi-coke is readily graphitisable upon heat-treatment to 2600 °C.

The mechanisms of the formation of semi-cokes by pitch pyrolysis have been reviewed (Marsh et al., 1999). In this study, they showed that when petroleum residues are pyrolysed semi-cokes of different properties are formed depending on factors such as type of the pitch material, viscosity of the pitch-material, heating rate, aromaticity indexes to name but a few. Mesophase is a pre-requisite for formation of these semi-cokes. These semi-cokes are precursors to different carbon artefacts including graphite. More important is that in petroleum-derived pitches mesophase was observed at temperatures as low as 350 °C. For example, in a pitch produced by high pressure pyrolysis of naphthalene, anisotropic spheres start to show up at a temperature of 350 °C (Lewis, 1971).

2.3.2 Fusion during carbonisation

Some factors affecting graphitisation of polymeric carbons have been reported (Kipling et al., 1964). This study observed that polymers which pass through the fusion stage during carbonisation (e.g. polyvinyl chloride) become graphitic when heated to graphitizing temperature, 2700 °C, while those which do not pass through the fusion stage become non-graphitic (e.g. polyvinylidene chloride). The fusion stage is the key factor for subsequent graphitisation of the polymers. Fusion during carbonisation is not the necessary and sufficient requirement for producing graphitic carbons; the other important aspect is that it must occur in a wide temperature range and the material undergoing fusion must contain varying molecular weights/complexes (Kipling et al., 1964).

2.3.3 Cross-linking

Another important factor is the type and extent of cross-linking in the parent material/precursor. There are different types of cross-links which could be found in the pre-carbon, namely cross-links in the original polymer precursor, cross-links occurring during decomposition of the parent precursor and those that are formed by the heteroatoms.

In order to form a carbon there must be a certain degree of cross-linking in a decomposing linear polymer. However extensive cross-linking may give 3 dimensional structures which could inhibit fusion during carbonisation and therefore result in a non-graphitic carbon. This phenomenon is found mostly in carbons derived from resol-type phenolic resins (Kipling et al., 1964).

Decomposition which occurs during the early stages of carbonisation can result in different types of intermediates for various precursors with different degree of cross-linking. For example, dehydration of cellulose result in the formation of ether links which is the form of cross-links that gives a non-graphitic carbon. Hydrogen-bonding in this material is also reported to inhibit fusion (Kipling et al., 1964).

Heteroatoms such as O, N, B and S which are sometimes found in the parent materials form different types of cross-links. These atoms can also be incorporated into the layer planes of a pre-carbon and are analogous to those in the heterocyclic compounds. Kipling et al. reported dehydrochlorination of polyvinyl chloride in the presence of air below 250 °C which forms a non-graphitising carbon when graphitized. It is reported that the air forms extensive cross-links which prevents occurrence of fusion. This was confirmed by the fact that pyrolysis of the same compound resulted in a graphitising carbon (Kipling et al., 1964). It has been also reported that excess amount of oxygen and/or sulphur in an organic precursor inhibits formation of mesophase spheres which is the key step in formation of graphitising carbons (Dubois et al., 1997).

It has also been reported that cumulative addition of sulphur to polyvinyl chloride before carbonisation leads to reduction in graphitisability of the polymer. About 9 % sulphur was sufficient to change this polymer from being graphitic to becoming non-graphitic when pyrolysed to 2700 °C (Kipling et al., 1964). Again, sulphur forms cross-links and inhibits fusion. Optical microscopy showed that the polymer sulphurised with 5 % S contained two regions of optical activity, one isotropic and the other anisotropic (Kipling and Shooter, 1966).

Unlike other heteroatoms, incorporation of boron into the pre-carbon has proved to improve the graphitisability of the precursor as it does not form extensive cross-links. The catalytic effect of boron on the graphitisation behavior of three different industrial carbons/cokes has been demonstrated (Murty et al., 1977). It was shown in this work that the same lattice constant, which is a measure of extent of graphitisation, was attained atmost 500 °C lower for carbons containing lower boron content (i.e. 0.5 and 1.0 wt %) than boron-free carbons. It was also shown that there is a limiting boron concentration of approximately 2.5 wt %, above which all boronated carbons show the same lattice constants values. However carbons boronated above this value show a faster graphitisation process apparently due to increase in the pre-exponential factor, a kinetic factor (Murty et al., 1977).

It has also been shown previously that substitutional incorporation of boron in the pre-carbon structure enhances its graphitisation (Hu and Chung, 1996). This particular study showed that a Boron/Carbon material synthesized from pyrolysis and subsequent graphitization at 2300 °C of the precursor 9-chloroborafluorene had X-ray diffraction parameters attainable by traditional carbons heat-treated in excess of 3000 °C. The process of graphitisation of the B/C material is apparently enhanced by in situ boron catalysis during heat-treatment. The interlayer spacing of the B/C material decreases with temperature, however, when compared to Murty's data (Murty

et al., 1977) on industrial carbons smaller interlayer spacings were attained in the B/C material for the same temperature. Unlike in Murty's data the B/C material does not show any limiting boron concentration value for the interlayer spacing, in fact at 2000 °C the minimum interlayer spacing for the B/C material is equal to that of graphite (Hu and Chung, 1996).

Enhanced diffusivity of boron is believed to be the mechanism of high temperature graphitisation of boronated carbons. Two mechanisms have been postulated by Fischbach:

- The substituted boron on the carbon matrix play the same role as vacancies, hence the boron atoms diffuse out of the matrix faster than carbon atoms thereby increasing rate of graphitisation.
- Secondly, during annealing of boronated carbons vacancy concentration in the matrix increase as excess boron diffuse out of the lattice, hence the removal of these vacancies during heat-treatment enhances graphitisation reaction (Fischbach, 1971).

Incorporation of boron into a pre-carbon can be vital or detrimental depending on the end application of the graphite. This is not desired for graphites used for nuclear reactor applications since boron has a larger absorption cross-section area for neutrons, i.e. approximately 4×10^{-21} cm^2. The heteroatoms O, B and N are removed from the precursor by heat-treatment to temperature above 1500 °C while sulphur can be entrapped into the carbon matrix up to about 2000 °C. In the next section we discuss catalytic graphitisation of organic precursors using inorganic additives/metals as catalysts.

2.3.4 Catalytic graphitisation

Graphitisation can be enhanced by addition of certain inorganic additives to the precursor carbons. The overall effect of these additives is to lower the temperature needed to achieve a certain degree of graphitisation. A review on catalytic effects of many inorganic additives on graphitisation of carbons as well as the mechanisms involved was reported (Marsh and Warburton, 1970). In this review the use of inorganic additives containing metals Al, Cu, Cr, Fe, etc were looked at.

2.4 Graphite properties applicable to nuclear industry

Graphite has many applications ranging from making pencils, electrodes, as well as lubricant for aerospace applications. In this section we focus on the properties of fuel matrix graphite used for nuclear applications as a moderator. Graphite is a suitable material for moderator and reflector in nuclear reactors because it exhibits low thermal expansion coefficients (CTE), excellent thermal shock resistance and low neutron activation (Kelly, 1981a). It is light, inexpensive, machinable and readily available. Graphite is one of the stable materials under irradiation; however its high temperature oxidation poses a problem and as such it requires oxygen protective systems for prolonged use. In pebble bed reactors, it is used as a neutron containment barrier in a UO_2-based fuel pebble wherein it encapsulates these fuel particles. It is used together with other coatings such as pyrolytic carbon and silicon carbide.

In the reactor, graphite is subjected to harsh conditions such as high neutron dosage, high temperature, fission reactions, etc. Thus the graphite used whether as moderator/reflector or encasing materials must withstand these conditions. One of the properties the graphite must possess is equal coefficients of thermal expansion in both the a-crystallographic axis and the c-crystallographic axis (see Table 2.1) to prevent the high temperature swelling of the reactor

block and therefore isotropic graphite is desirable in this instance. The other important factor is that the graphite must possess high density of at least 1.7 $g.cm^{-3}$ and hence high strength at high temperature (Cohn et al., 2005).

Table 2.1: Properties of nuclear graphite (Cohn et al., 2005)

Property	Anisotropic Graphite	Isotropic Graphite
Density($g.cm^{-3}$)	1.71	1.86
Resistance (μΩ.cm)	735	1000
Tensile strength (kPa^c)	9.93	46.172
Coefficient of thermal expansion (10^{-6}/°C)		
With grain	2.2	5.3
Against grain	2.8	5.3
Anisotropic ratio	1.73	1.0
Total ash (ppm)	740	400
Boron content (ppm)	0.4	0.3

The graphite moderator must possess a greater slow-down power for neutrons than the tendency to capture them; therefore the graphite should have low boron content (see Table 2.1) as boron has a larger absorption cross-section area for neutrons, i.e. approximately 4×10^{-21} cm^2. The boron- free graphite should have a low neutron capture cross-section of $0.0032 \pm 0.002 \times 10^{-24}$ cm^2. This factor is dependent on the purity of the starting organic precursor as well as the processing conditions of the graphite manufacture (Cohn et al., 2005).

2.5 Fabrication and properties of graphite matrix material for various high temperature gas-cooled nuclear reactors

Graphite matrix material or composites are used as fuel encasement; a neutron moderator as well as a heat conductor in high temperature reactors (Zhao et al., 2006) (Tang et al., 2002) (Tang et al., 2008) (Schulze et al., 1981) (Mehner et al., 1990). The graphite matrix is composed of natural graphite, synthetic graphite and resin in a certain proportion. The graphite matrix materials have been developed in Germany in the 1950s for the use in the German high temperature gas cooled reactors. For example, the Arbeits gemeinschaft Versuchs-Reaktor (AVR) and Thorium Hochtemperatur Reaktor (THTR) (Schulze et al., 1981) (Mehner et al., 1990) (Hoinkis and Robens, 1989) uses standard matrix graphite composites, A3-3 and A3-27. The fabrication steps for the fuel-free standard matrix graphite, A3-3 are outlined in Figure 2.4 below. The filler particles natural flake graphite (64 wt.%), graphitized coke powder (16 wt.%) were mixed to form a graphite filler which was then kneaded with phenol/formaldehyde based phenolic resin (20 wt.%) dissolved in methanol. After kneading, the mix was dried and then ground to form a resinated graphitic powder. The graphitic powder was then pre-pressed at a pressure of 30 MPa at 25 °C in a silicon rubber die, followed by quasi-isostatic cold molding at a pressure of 300-350 MPa at 25 °C in a silicon rubber mold. The fabrication steps of the A3-27 graphite matrix material (which was only used in the AVR reactor) are shown in Figure 2.5. First, the natural flake graphite (62.4 wt.%), the graphitized coke powder (15.6 wt.%) and the phenol/hexamethylenetetramine based phenolic resin (22 wt.%) were mixed together at a temperature of 130 °C. The hot mixing was then followed by grinding to form a resinated powder which was subsequently pre-pressed at a pressure of 30 MPa at 25 °C.

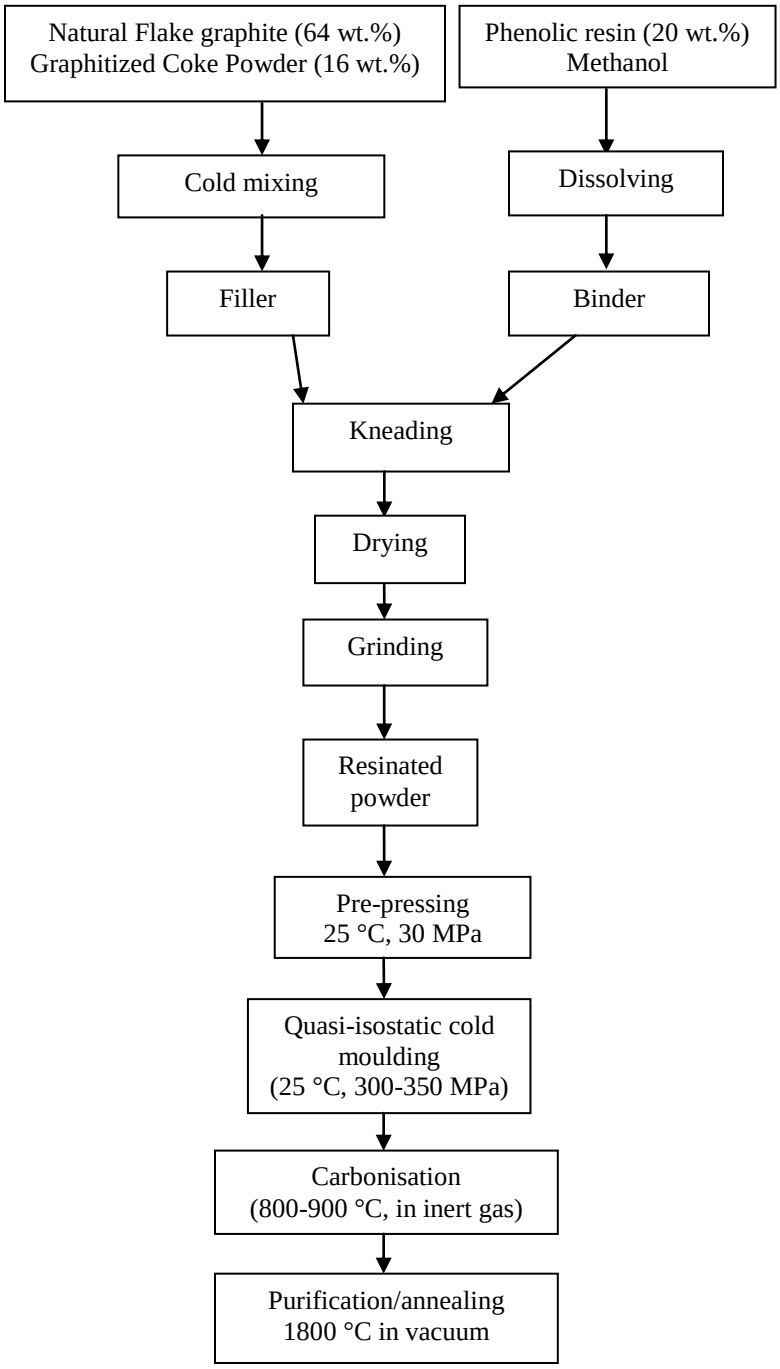

Figure 2.4: Fabrication steps of standard A3-3 graphite matrix used in the German AVR and THTR reactors (Schulze et al., 1981) (Hoinkis and Robens, 1989).

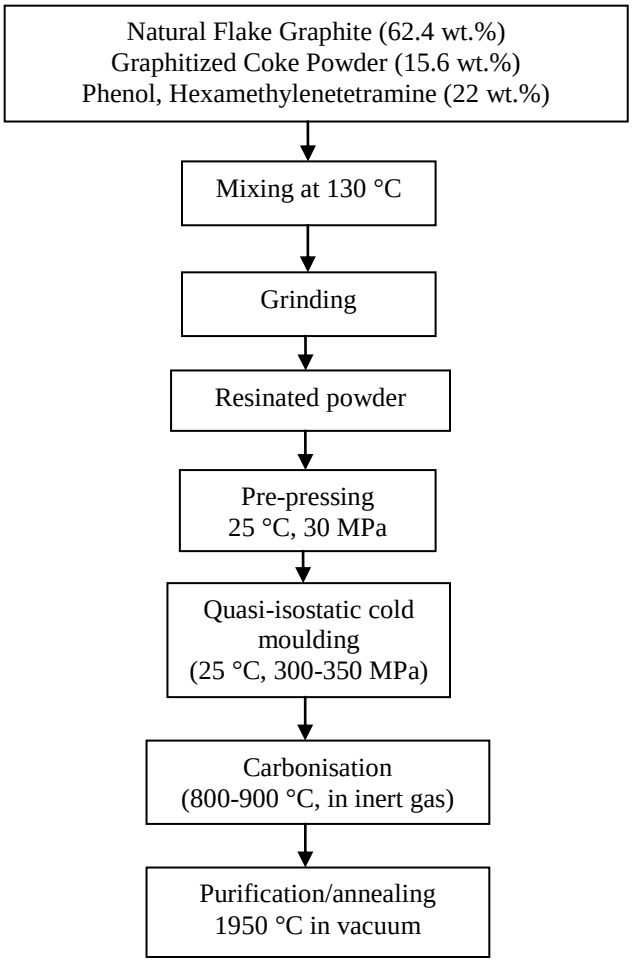

Figure 2.5: Fabrication steps of the A3-27 graphite matrix material used in the German AVR reactors (Schulze et al., 1981) (Hoinkis and Robens, 1989)

The compacts were further subjected to quasi-isostatic cold moulding at a pressure of 300-350 MPa at 25 °C in a silicon rubber mold. The compacts or spheres were then carbonized at 800-900 °C in inert atmosphere followed by purification or annealing at 1950 °C in vacuum. The main differences in the fabrication of the A3-3 and A3-27 graphite matrix materials are:

- The initial weight percentages of the raw materials are not the same.

- A phenol/formaldehyde resin was used as binder in the A3-3 matrix whilst a phenol/hexamethylenetetramine resin was used in the case of A3-27 matrix.
- The A3-3 matrix raw graphites were cold mixed first before mixing with the resin whilst in the A3-27 matrix all the raw materials were mixed at the same time and at high temperature (130 °C).
- The purification of the graphitic spheres was performed at 1800 °C for the A3-3 matrix while it was performed at 1950 °C for the A3-27 matrix.

A similar method to the one used to make A3-3 matrix was used in the manufacture of the graphite matrix used in the Chinese high temperature reactor (HTR-10), see Figure 2.6. The natural flake graphite (from Beishu mine, China) was used as filler together with electrographite. These graphites were first crushed into a suitable particle size distribution using a mill, followed by pre-mixing.

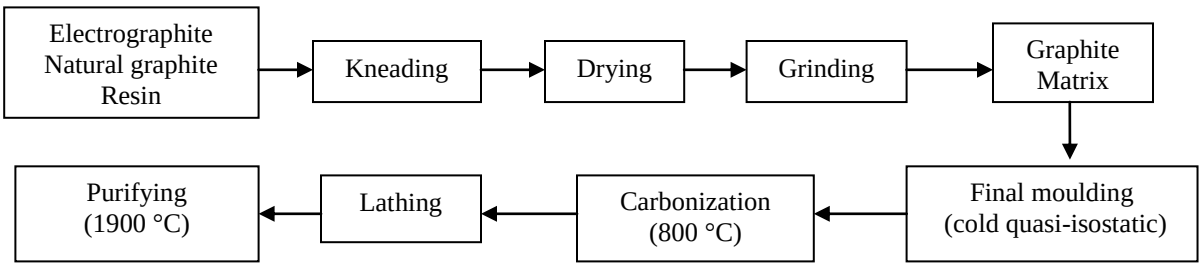

Figure 2.6: Manufacture steps of graphite matrix for Chinese HTR-10 (Zhao et al., 2006, Tang et al., 2008).

The graphite mix was then kneaded with dissolved phenolic resin binder (phenol/formaldehyde based), dried at 100 °C under vacuum and ground using a hammer mill with a sieve of 1 mm. The matrix was then moulded using cold quasi-isostatic pressing in a silicon rubber die at a

pressure up to 300 MPa. The pressing was followed by carbonisation at 800 °C to remove volatiles in the phenolic resin, lathing and purification at 1900 °C (Zhao et al., 2006) (Tang et al., 2002, Tang et al., 2008). The fabrication methods/steps used dictate the properties of these matrix graphite materials; some properties of interest are shown in Table 2.2.

Table 2.2: Properties of graphite matrix materials used in some HTRs.

Reactor	Matrix type (HTT)	Bulk density ($g.cm^{-3}$)	CTE (20-500 °C, 10^{-6} K^{-1})	Thermal conductivity, at 1000 °C ($W.m^{-1}K^{-1}$)	Reference
AVR	A3-3 (1800 °C)	1.70	∥2.80 ⊥2.92	∥26 ⊥27	(Rind, 1981) (Schulze et al., 1981) (IAEA, June 2012)
	A3-27 (1950 °C)	1.74	∥2.43 ⊥2.69	∥44 ⊥39	
THTR	A3-3 (1950 °C)	1.73	∥2.89 ⊥3.45	∥41 ⊥37	
HTR-10	A3-3 (1800 °C)	1.73	∥2.72 ⊥2.99	∥29.3 ⊥29.7	(Tang et al., 2008)

Similar graphitic composites were made by compacting graphite powders of variable grades (1645, 3610, 4012 and 4956 all from Asbury carbons; SFG-75 and KS-150 from Timacal Graphite and Carbon) ad-mixed with phenolic resin (Cunningham et al., 2005). In this study, the compaction behavior, the structure and mechanical properties of graphite and graphite-phenolic resin mixtures were characterized. This work showed that compaction of the graphites without addition of the resin did not produce adequate compacts. The graphite powders, 3610, 1645 and SFG-75 were very compactable when ad-mixed with the resin and showed green densities above 1.88 $g.cm^{-3}$ and green strength greater than 11.2 MPa. On the other hand the mixtures of the graphites 4012 and 4956 showed lower green densities and strengths. XRD analysis also showed that mixtures with high green densities and strengths exhibited highest degree of anisotropy and

their (002) diffraction planes showed preferential alignment in the direction perpendicular to compaction axis. On the other hand no preferential (002) planes alignment was observed for non-compactable 4956 graphite; Graphite 4012 showed small degree of orientation and was weak and thus classified as non-compactable (Cunningham et al., 2005).

In conclusion the graphite required for nuclear applications must meet most of the above mentioned characteristics, if not all, depending on the reactor design. The graphite manufacture and processing steps, as discussed in Section 2.2, can be quite costly. The fabrication of graphite matrix material used as encasement in fuel elements of high temperature gas-cooled reactors was discussed. In most gas-cooled HTRs, the graphite matrix is prepared by cold quasi-isostatic moulding at high pressure. The properties of the prepared matrix depend on the fabrication route employed.

References

BACON, G. E. (1950) *Acta Crystallographica,* 3**,** 320.

BACON, G. E. (1950b) *Acta Crystallographica,* 3**,** 137.

BISCOE, J. & WARREN, B. E. (1942) *Journal of Applied Physics,* 13**,** 364-371.

BROOKS, J. D. & TAYLOR, G. H. (1965) The formation of graphitising carbons from the liquid phase. *Carbon,* 3**,** 185.

COHN, J. G., STERN, E. W. & ETRIS, S. F. (2005) Graphite, Artificial IN KIRK-OTHMER (Ed.) *Kirk-Othmer Encyclopedia of Chemical Technology.* 5 ed., John Wiley & Sons.

CUNNINGHAM, N., LEFEVRE, M., DODELET, J.-P., THOMAS, Y. & PELLETIER, S. (2005) Structural and mechanical characterization of as-compacted powder mixtures of graphite and phenolic resin. *Carbon,* 43**,** 3054-3066.

DUBOIS, J., AGACHE, C. & WHITE, J. L. (1997) The carbonaceous mesophase formed in the pyrolysis of graphitisable organic materials. *Material characterisation,* 39**,** 105-119.

EDWARDS, I. A. S. (1989) Structure in Carbons and Carbon Forms. IN MARSH, H. (Ed.) *Introduction to Carbon Science.* London, Butterworths.

FISCHBACH, D. B. (1971) IN PHILIP L WALKER, J. (Ed.) *Chemistry and Physics of Carbon.* New York, Marcel Dekker, INC.

FITZER, E., KOCHLING, K. H., BOEHM, H. P. & MARSH, H. (1995) Recommended terminology for the description of carbon as a solid. *Pure and Applied Chemistry,* 67**,** 473-506.

FRANKLIN, R. E. (1951a) *Proceedings of the Royal Society,* 209**,** 196-218.

FRANKLIN, R. E. (1951b) *Acta Crystallographica,* 4**,** 253-261.

GEIM, A. K. & NOVOSELOV, K. S. (March 2007) The rise of graphene. *Nature Materials,* 6**,** 183-191.

HOERNI, J. (1949) *Nature,* 164**,** 1045.

HOUSKA, C. R. & WARREN, B. E. (1954) *Journal of Applied Physics,* 25**,** 1503.

HOINKIS, E. & ROBENS, E. (1989) Surface area and porosity of unmodified graphitic matrices A3-27 and A3-3 (1950) and oxidized matrix A3-3 (1950). *Carbon,* 27**,** 157-168.

HU, R. & CHUNG, T. C. (1996) *Carbon,* 43**,** 1181-1190.

HULL, A. W. (1917) *Physical review,* 10**,** 661.

IAEA (June 2012) Advances in High Temperature Gas Cooled Reactor Fuel Technology. Vienna, International Atomic Energy Agency. (IAEA-TECDOC-1674) p. 224-250

IIJIMA, S. (1991) Helical microtubules of graphitic carbon. *Nature,* 354**,** 56-58.

JAGODZINSKI, H. (1949) *Acta Crystallographica,* 2**,** 298.

KELLY, B. T. (1981) *Physics of Graphite,* London and New Jersey, Applied Science Publishers.

KIPLING, J. J., SHERWOOD, J. N., SHOOTER, P. V. & THOMPSON, N. R. (1964) Factors influencing the graphitization of polymer carbons. *Carbon,* 1**,** 315-320.

KIPLING, J. J. & SHOOTER, P. V. (1966) Factors affecting the graphitisation of carbon: Evidence from polarised light microscopy. *Carbon,* 4**,** 1-4.

KIRK-OTHMER (2005) Graphite, Artificial. *Encyclopaedia of Chemical Technology.*

KROTO, H. W., HEATH, J. R., O'BRIEN, S. C., CURL, R. F. & SMALLEY, R. E. (1985) C_{60}: Buckminsterfullerene. *Nature,* 318**,** 162-163.

LAIDLER, D. & TAYLOR, A. (1940) *Nature,* 141**,** 130.

LEWIS, R. T. (1971) 12th biennial conference on carbon. Pittsburg, American Carbon Society.

LIPSON, H. & STOKES, A. R. (1942) *Proceedings of the Physics Society of London.,* A181**,** 101.

MARSH, H., MARTINEZ-ESCANDELL, M. & RODRIGUEZ-REINOSO, F. (1999) Semocokes from pitch pyrolysis: Mechanisms and kinetics. *Carbon,* 37**,** 363-390.

MARSH, H. & WARBURTON, A. P. (1970) Catalysis of graphitisation. *Journal of Applied Chemistry,* 20**,** 133-142.

MEHNER, A.-W., HEIT, W., ROLLIG, K., RAGOSS, R. & MULLER, H. (1990) Spherical fuel elements for advanced HTR manufacture and qualification by irradiation testing *Journal of Nuclear Materials,* 171**,** 9-18.

MIAO, J.-Y., HWANG, D. W., NARASIMHULU, K. V., LIN, P.-I., CHEN, Y.-T., LIN, S.-H. & HWANG, L.-P. (2004) Synthesis and properties of carbon nanospheres grown by CVD using kaolin supported transition metal catalysts. *Carbon,* 42**,** 813-822.

MURTY, H. N., BIEDERMAN, D. L. & HEINTZ, E. A. (1977) Apparent catalysis of graphitisation. 3. Effect of boron *Fuel,* 56**,** 305-312.

NOVOSELOV, K. S., GEIM, A. K., MOROZOV, S. V., JIANG, D., ZHANG, Y., DUBONOS, S. Y., GRIGORIEVA, I. V. & FIRSOV, A. A. (2004) Electric field effect in atomically thin carbon films. *Science,* 306**,** 666-669.

RIND, W. (1981) Transport of fission products in matrix and graphite. IN HOINKIS, E. (Ed.) *Proceedings of a coloquim held at the Hahn-Meitner-Institut* Berlin, Germany, Hahn-Meitner-Institut fur kernforschung Berlin Gmbh.

SCHULZE, R. E., SCHULZE, H. A. & RIND, W. (1981) Report of the Keruforschungslage Julich, Graphic Matrix Materials for Spherical HTR Fuel Elements. p. 118

TANG, C. H., TANG, Y., ZHU, J. G., ZOU, Y. W., LI, J. O. & NI, X. O. (2002) Design and manufacture of the fuel element for 10 MW high temperature gas-cooled reactor. *Nuclear Engineering and Design,* 218**,** 91-102.

TANG, C., LI, Z., ZHOU, Y. & FU, X. (2008) Irradiation testing of matrix material for spherical HTR-10 fuel elements. *Nuclear Engineering and Design,* 238**,** 2886-2892.

WARREN, B. E. & GRINGRIICH, N. S. (1934) *Physical Review,* 46**,** 368-399.

WOLF, R. (2001) Manufacture of bulk carbon and bulk graphite. IN B. RAND, S. P. A., M. F. YARDIM (Ed.) *Design and Control of Structure of Advanced Carbon Materials for Enhanced Performance*

Dordrecht/Boston/London, Kluwer Academic Publishers.

ZHAO, H. S., LIANG, T. X., ZHANG, J., HE, J., ZOU, Y. W. & TANG, C. H. (2006) Manufacture and characteristics of spherical fuel elements for the HTR-10. *Nuclear Engineering and Design,* 236**,** 643-647.

CHAPTER 3: PHENOLIC RESINS

Introduction

This chapter focuses on production of phenolic resins (resols or novolacs) and their applications as binders. The main source of information on how these materials are made is described in a book by Knop and Pilato (Knop and Pilato, 1985). Phenolic resins are relatively inexpensive, light weight and have excellent insulating properties.

3.1 Raw materials for phenolic resins production

The raw materials for the synthesis of phenolic resins are phenols and aldehydes. Phenols are a class of compounds containing a hydroxyl group bonded directly to the aromatic nucleus or benzene structure. Phenols behave like weak acids and dissolve readily in aqueous sodium hydroxide and are insoluble in aqueous sodium carbonate. The simplest or pure phenol is also called hydroxybenzene; it has a molecular weight of 94.1 $g.mol^{-1}$, melting point 40.9 °C and boiling point 181.8 °C. All other types of phenol such as cresols are derived from this structure. The largest use of phenols is in the production of phenol-formaldehyde resins (Knop and Pilato, 1985). The use of formaldehyde in the synthesis of phenolic resins has attained much commercial importance than other aldehydes such as acetaldehyde and furfural. Formaldehyde is a colourless, pungent, irritating gas and it exists in aqueous solution as a mixture of oligomers of polymethylene glycol. It is used mainly in the production of thermosetting resins based on

phenol, urea and melamine (Knop and Pilato, 1985). The next section focuses on formation of different types of phenolic resins, i.e. Phenol-formaldehyde reactions.

3.2 Phenol/Formaldehyde reactions

Phenolic resins are formed by step-wise polymerisation of di-functional aldehyde monomers and phenols having more than 2 functionalities. The end characteristics of the phenolic resin depend on temperature and pH at which the reaction is carried out. There are two types of phenolic resins formed when phenol and formaldehyde react, namely, Novolacs and Resols.

3.2.1. Novolacs

Novolacs are formed from acid catalysed reaction (pH 1 to 4) of phenol and formaldehyde at a Formaldehyde-Phenol mole ratio less than 1. The reaction occurs as an electrophilic substitution reaction, see Figure 3.1. The first step entails formation of hydroxymethylenecarbonium ion from the reaction of the formaldehyde with an acid; followed by reaction of the formed carbonium ion and phenol to form o-hydroxymethylphenol. The substitution is observed at an ortho-position under acidic conditions. The o-hydroxymethylphenol formation is an intermediate step and forms a benzyliccarbonium ion in acidic medium and water as by-product. The next step involves the reaction of the benzyliccarbonium ion with phenol to form dihydroxydiphenylmethane which is a basic back-bone for a novolac-type phenolic resin(Knop and Pilato, 1985).

The reaction of phenol with formaldehyde in acidic medium does not form meta-substituted phenolics. A typical example of the novolac-type phenolic resin is shown in Figure 3.2, with only ortho-para substitutions to the phenol structure. The novolacs are linear condensation

products linked with methylene bridges and have a relatively low molecular weight (MW) of about 2000. They are soluble in alcohols, fusible and can be cured only by addition of a hardener.

3.2.2. Resoles

Resoles are formed from base catalysed reaction (pH > 5) of phenol and formaldehyde at a formaldehyde-phenol ratio more than 1. They are mono or polynuclearhydroxymethylphenols (HMP) and are stable at room temperature. Commonly used catalysts include group 1 and 2 metal hydroxides, ammonia, tertiary amines as well as transition metal hydroxides.

An example of an alkali catalysed reaction of a phenol and formaldehyde is shown in Figure 3.3. First the phenol reacts quickly with an alkali forming resonance stabilized phenoxide ion, since the hydroxyl group in phenol is an inductive electron withdrawing group and is a good ortho/para director; the reaction of these resonance stabilized ions with formaldehyde result in monomethylol phenol derivatives at ortho/para positions, see step 2 and 3. The monomethylol phenol derivatives then react with excess formaldehyde to form o,p-dihydroxymethylphenol, o,o-dihydroxymethylphenol and trihydroxymethylphenol (Sprengling and Freeman, 1950). The ortho substitution is favoured when the metal hydroxides of group 1 and 2 elements are utilised as catalysts at an intermediate pH. The mechanism by which the formaldehyde reacts with phenoxide ion is not fully understood (Knop and Pilato, 1985). Unlike the novolacs, the resoles form 3 dimensional, cross linked insoluble and infusible polymers when heat-treated under inert conditions.

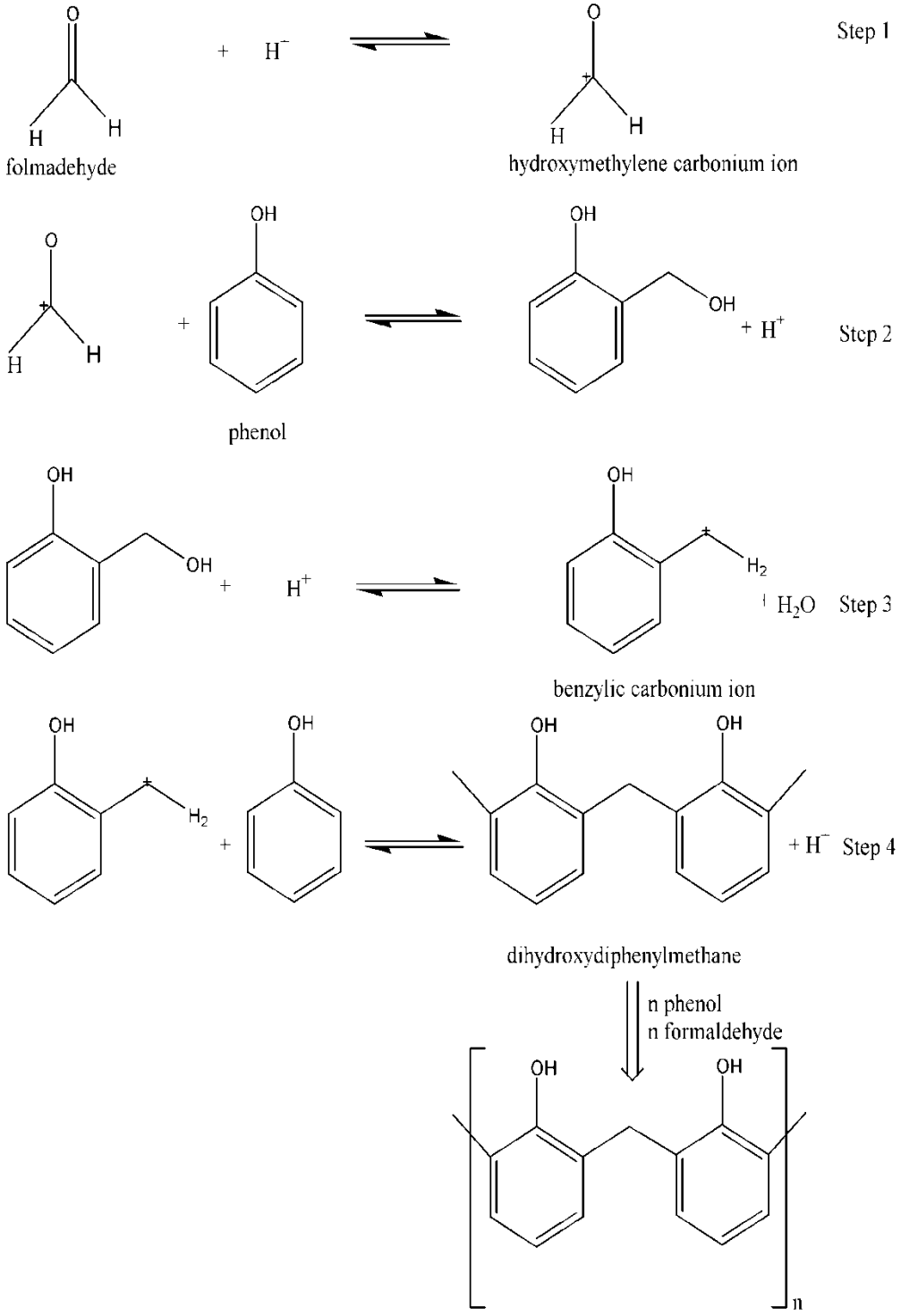

Figure 3.1: The reaction scheme for the formation of a novolac-type phenolic resin (Adopted and re-drawn from (Knop and Pilato, 1985)).

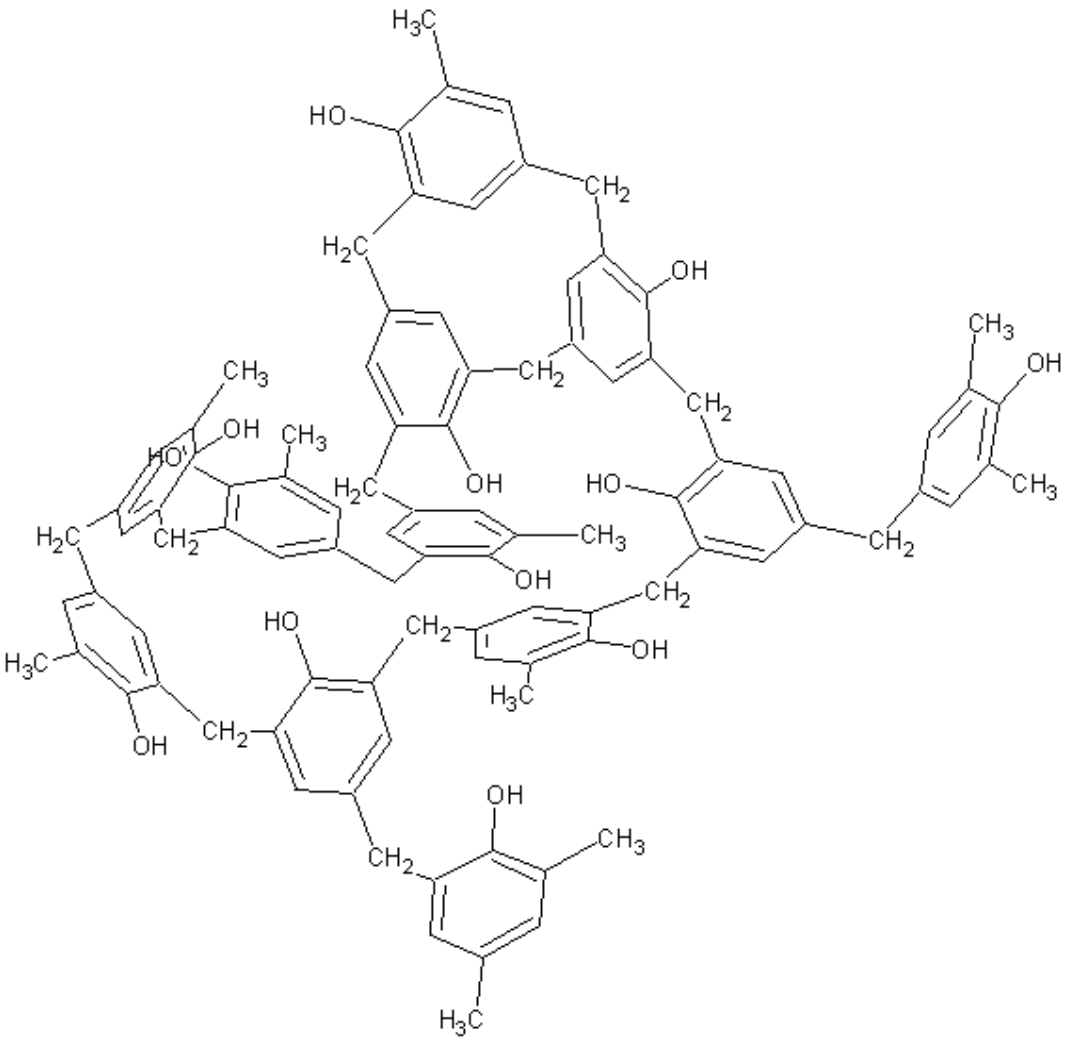

Figure 3.2: A typical example of a novolac-type phenolic resin (Knop and Pilato, 1985).

It must be clearly stated that phenol and formaldehyde are basic raw materials for the production of phenolic resins, some substituted phenols and other aldehydes (e.g. cresols and furfural) may be used for specialised applications. Therefore phenolic resins of many different forms can be produced depending on the raw starting materials, reaction conditions and their end application.

3.3 Use of phenolic resins as binders

Phenolic resins have many applications which include use as abrasives, coatings, refractory materials, rubber, adhesives, composites, etc. Phenolic resins form a non-graphitising carbon upon heat-treatment to graphitising temperatures (≥ 2800 °C). Due to their high affinity for graphitic carbon, good wettability, good molding properties, good thermosetting properties and high carbon content, phenolic resins have been used as binders for moderator matrix graphites in high temperature nuclear reactors (Zhao et al., 2006, Nicholls, 2001, Nicholls, 2002).

In this project a phenolic resin was used as a binder for two grades of nuclear graphites, i.e. natural flake graphite and synthetic or electro graphite. The resulting graphitic matrix or composite is used together with other materials as an encasement for fuel particles and serves as fast neutron moderator in the reactor.

This chapter reviewed what phenolic resins are, how they are made and how to control the type of the phenolic resin being formed. The use of these resins as binders was elucidated. In the experimental section of this thesis (Chapter 5), novolac phenolic resin was used as a binder for two graphite filler materials.

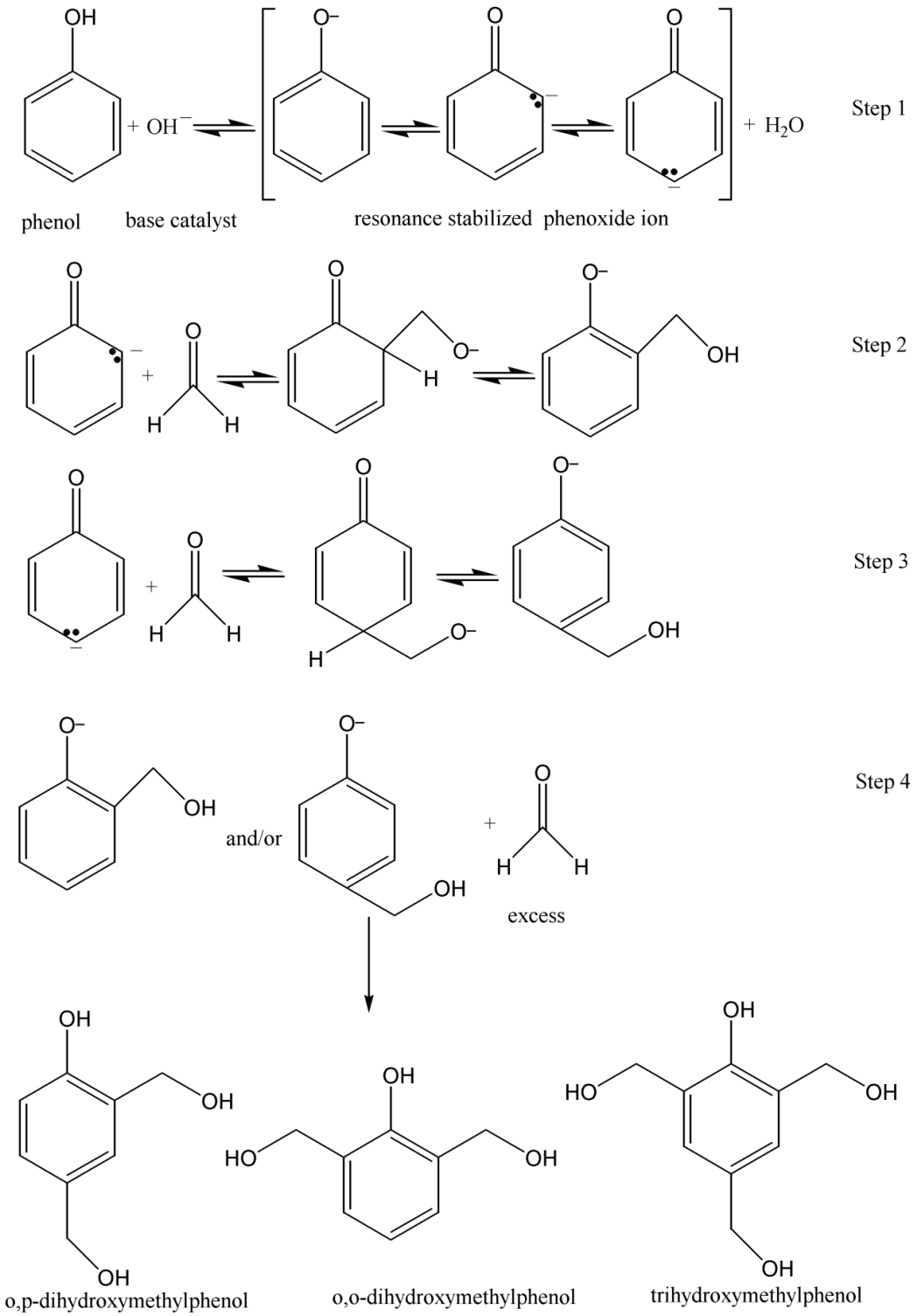

Figure 3.3: The reaction scheme for the alkali-catalysed formation of a resol-type phenolic resin (Knop and Pilato, 1985).

References

KNOP, A. & PILATO, L. A. (1985) *Phenolic Resins: Chemistry, applications and performance.* Berlin, Heidelberg, New York,Tokyo, Springler-Verlag.

NICHOLLS, D. R. (2001) The Pebble Bed Modular Reactor. *Transactions of the Royal Society of South Africa,* 56**,** 125-130.

NICHOLLS, D. R. (2002) The Pebble Bed Modular Reactor. *South African Journal of Science,* 98**,** 31-35.

SPRENGLING, G. R. & FREEMAN, J. H. (1950) The reaction of phenol with formaldehyde. *Journal of American Chemical Society,* 72**,** 1982-1985.

ZHAO, H. S., LIANG, T. X., ZHANG, J., HE, J., ZOU, Y. W. & TANG, C. H. (2006) Manufacture and characteristics of spherical fuel elements for the HTR-10. *Nuclear Engineering and Design,* 236**,** 643-647.

CHAPTER 4: THEORETICAL BACKGROUND ON TECHNIQUES

4.1. Laser diffraction

Laser diffraction is a technique used in the measurement of particle size distribution of a powdered sample dispersed in a solvent. The particulate sample must be insoluble in the solvent at room temperature. The particle size distribution is measured by passing a laser beam on particles dispersed in a solvent; the particles then scatter the laser light. The angular scattering intensity data is obtained and analysed to calculate the size of the particles based on Mie theory of light scattering (Mie, 1908, Hergert and Wriedt, 2012). The particle size is given in terms of sphere diameter, i.e. this technique assumes all particles are spherical. The advantages of this technique are that no calibration is required, it is easy to rapidly perform the measurements, it can measure sub-micron to few millimeter size range and it is repeatable.

4.2. X-ray diffraction (XRD)

X-ray diffraction is a technique used to measure the positional arrangement of atoms in a crystal lattice in crystalline materials (they possess repetitive arrangement of atoms in space). It is also useful in determining interlayer spacings, crystallite size, preferred orientation and composition. In a typical XRD measurement, a beam of monochromatic X-rays is incident on the sample surface and the X-rays are elastically scattered in various directions as shown in Figure 4.1. The scattered X-rays will interfere constructively and destructively, the latter ones will cancel out while those that interfere constructively will satisfy Bragg condition below:

$$2d \sin\theta = n\lambda \tag{4.1}$$

where d is the spacing between diffracting layer planes, θ is the incident beam angle, n is an integer representing order of the reflection and λ is the wavelength of the radiation source used.

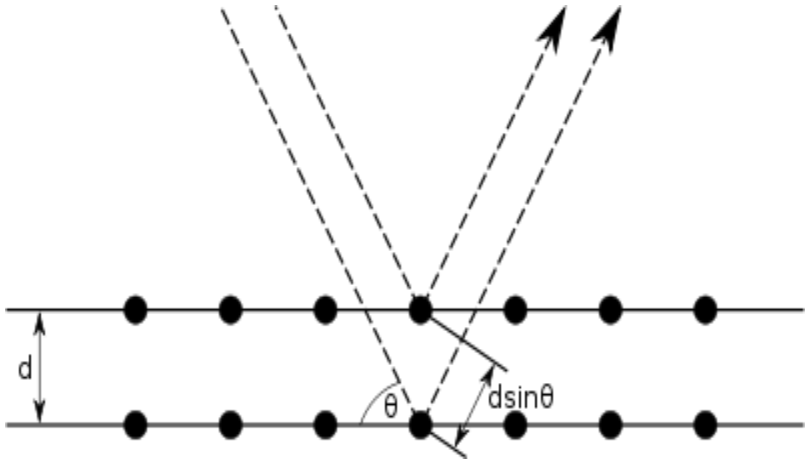

Figure 4.1: Schematic representation of the diffraction of X-rays beam on the sample surface (Cullity, 1978).

It is these X-rays which are then diffracted, detected and recorded as intensity versus scattering angle (2θ). These intensities are due to diffraction in various lattice planes in a crystalline material. An example of a XRD pattern for hexagonal synthetic polycrystalline graphite is shown in Figure 4.2 below. The attained spectrum is then fitted with the reported literature patterns in the International Centre for Diffraction Data (ICDD) database. After the fitting procedure, the lattice planes as well as the phase are indentified consistent with reported data.

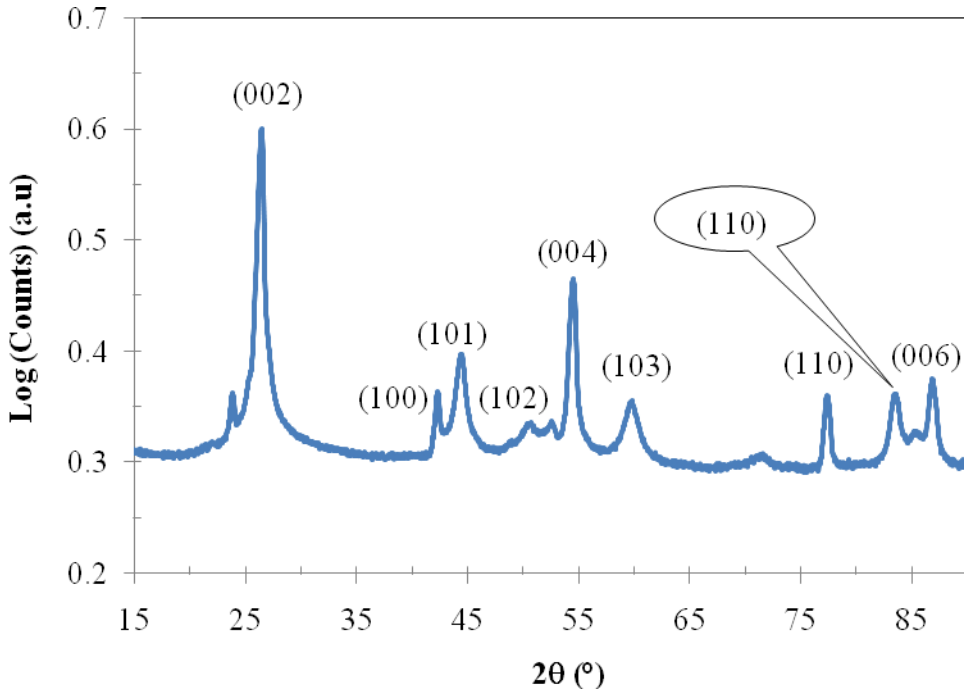

Figure 4.2: The X-ray diffraction pattern of a hexagonal synthetic graphite crystal used in this work.

For example the synthetic graphite pattern shown in Figure 4.2 fitted exactly with the hexagonal crystalline phase of graphite (Trucano and Chen, 1975). The (002) peak which is observed around 2θ~26 ° (if CuK_{α} source is used) is the most dominant and very crucial in graphite characterization as it is used in calculating interlayer spacing using equation (4.1), the degree of graphitization, g, which is a measure of how close to the ideal single crystalline hexagonal crystalline graphite, is calculated using the following equation (Nightingale, 1962):

$$g = \frac{3.44 - d_{002}}{3.44 - 3.354} \qquad (4.2)$$

where 3.44 is by definition the interlayer spacing of a turbostratic carbon in Å, d_{002} is the observed interlayer spacing in the material and 3.354 is the interlayer spacing of the ideal single crystalline graphite in Å.

The out of plane (L_c) and in-plane (L_a) crystal sizes can be calculated using the Scherer equation shown below (Scherer, 1918):

$$L = \frac{K\lambda}{\beta \cos\theta} \tag{4.3}$$

where L is the crystal size, θ is the incident angle of the beam, λ is the wavelength of the radiation source used, β is the peak width at half maximum intensity and K is the shape factor. The shape factor K equal to 0.9 is utilized when determining the out of plane crystal size, L_c together with angular position of the (002) peak (Klug and Alexander, 1954). When calculating the in-plane crystallite size, $L_a$the K factor value of 1.84 is utilized together with (110) diffraction peak (Warren, 1941). XRD method has been extensively utilized in the characterization of carbon materials more than 100 years ago. For example Bragg used it to determine the crystal structure of diamond (Bragg and Bragg, 1913). This technique has also been used to characterize graphites of different origins (Trucano and Chen, 1975, Lipson and Stokes, 1942a, Kelly, 1981b, Parthasaray et al., 2006, Ruland, 1965).

4.3. Raman Spectroscopy

This is a spectroscopic technique which measures vibrational, rotational and low-frequency modes in the system or sample by using inelastic scattering of photons resulting from interaction of laser (in the visible, infrared or near ultraviolet region) with sample or system. In a typical

Raman spectroscopy measurement, a sample is incident with a monochromatic laser beam and then light from the illuminated spot is collected with a lens and sent through a monochromator whereby wavelengths closer to that of the laser are filtered out while the rest is collected into a detector. Typically, a monochromatic laser beam is incident on a molecule and interacts with the electron cloud and bonds of the molecule and as a result a laser photon excites the molecule from the ground to the virtual energy state. This is called spontaneous Raman effect. This molecule will emit a photon and returns to a different vibrational or rotational state during its relaxation. The difference in energy between the new vibrational or rotational state and the ground state result in the shift in the frequency of the emitted photon relative to the laser excitation wavelength. This shift is called Raman shift wave number and is characteristic of the sample or system under study and serves as its finger print of the sample. This technique has been used extensively in carbon science to characterize different types of materials such as graphite (Tuinstra and Koenig, 1970, Nakamizo et al., 1974a, Wang et al., 1990), diamond (Prawer and Nemanich, 2004, Ferrari and Robertson, 2004), carbon nanotubes (Dresselhaus et al., 2004, Hodkiewicz, 2013), fullerenes (Schettino et al., 2002), grapheme (Dresselhaus et al., 2010a, Dresselhaus et al., 2010b) and others. The Raman spectra of different carbon materials are shown in Figure 4.3 and Figure 4.4below. Figure 4.3shows the Raman spectra of diamond and graphite on silicon substrate, the diamond spectra exhibit a single band around 1332 cm^{-1}due to vibration of the C-C single bonds in the tetrahedral crystal structure of diamond. The graphite on silicon substrate spectrum shows bands around 520 and 950 cm^{-1} characteristic of silicon, a 1^{st} order band around 1582 cm^{-1} (called G band) attributtable to the vibration of the C-C double bonds (sp^2) and a 2^{nd} order peak around 2650 cm^{-1}. In Figure 4.4the spectra of graphene, highly oriented pyrolytic graphite (HOPG), single-walled carbon nanotubes (SWNT) and amorphous

carbon are shown; due to their different vibrational modes or Raman signatures these materials can be distinguished with ease. Graphene comprise two main bands around 1580 and 2650 cm^{-1} due to C-C double vibrations (sp^2); the latter is the second order peak also called G' band. The HOPG has a similar Raman signature as the graphene except that it's G' band is of low intensity. On the other hand SWNT possess additional peaks around 250 cm^{-1} and 1340 cm^{-1} due to radial breathing modes (RBM) of the tubes and disorder induced D-band, respectively. The RBM is very important in calculating the diameter of the SWNT. The amorphous carbon spectrum consist of mainly two bands, i.e. the D- and the G-bands, which are characteristic of C-C single (sp^3) and double (sp^2) vibrations, respectively. In amorphous carbon, the D-peak is more intense than the G-peak showing high degree of disorder or high fraction of sp^3 carbon atoms. This illustrates the power of Raman spectroscopy as a characterization tool.

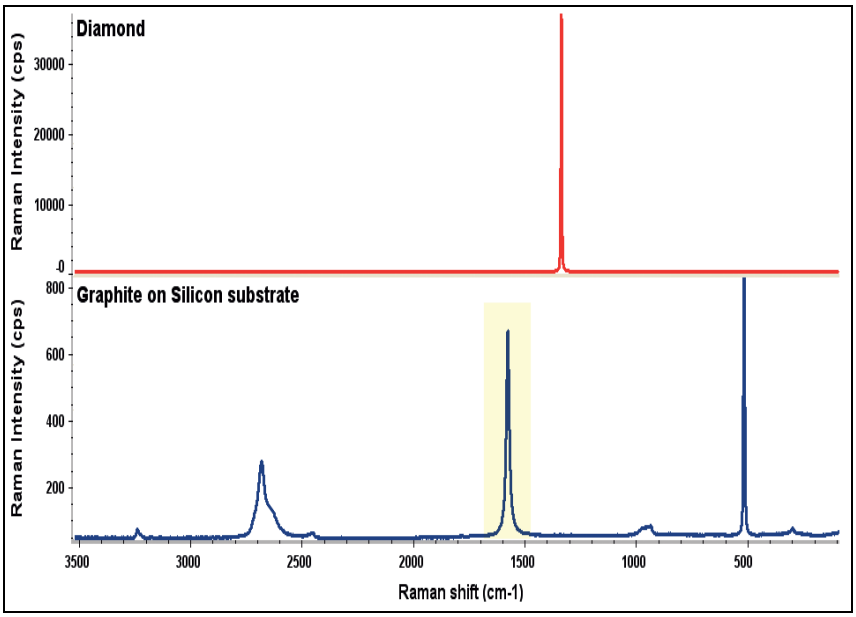

Figure 4.3: The Raman spectra of diamond and graphite on Silicon substrate. (Hodkiewicz, 2013)

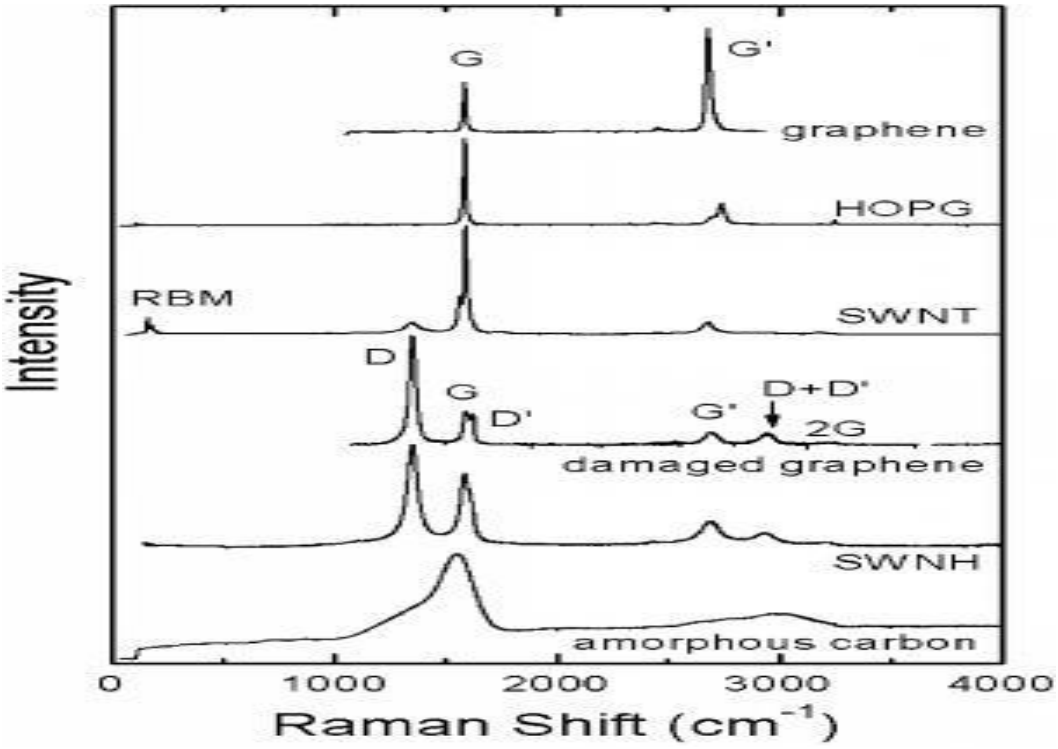

Figure 4.4: The Raman spectra of various carbon materials. (Dresselhaus et al., 2010a)

The advantages of using this technique are it is non-destructive and requires no or little sample preparation. It can also be utilized to determine parameters such as crystallite size and perfection, stress evaluation and structural defects.

4.4. Optical Microscopy (OM)

Optical microscopy is a technique which uses visible light together with a system of lenses and cameras to magnify the image of small specimens. An example of a modern optical microscope is shown in Figure 4.5 below. It typically consists of structural components such as an eyepiece (1) used for bringing the sample image under view into focus to the eye; an objective turret or revolver (2) which is used to hold and change between different objective lenses (3). Objective lenses are usually cylindrical and contain a glass single or multi-element lens. They are

characterized by mainly two parameters, magnification and numerical aperture; the former ranges from 5× to 100× while the latter ranges from 0.14 to 0.7. Objectives having higher magnification normally possess higher numerical aperture and shorter focal lengths.

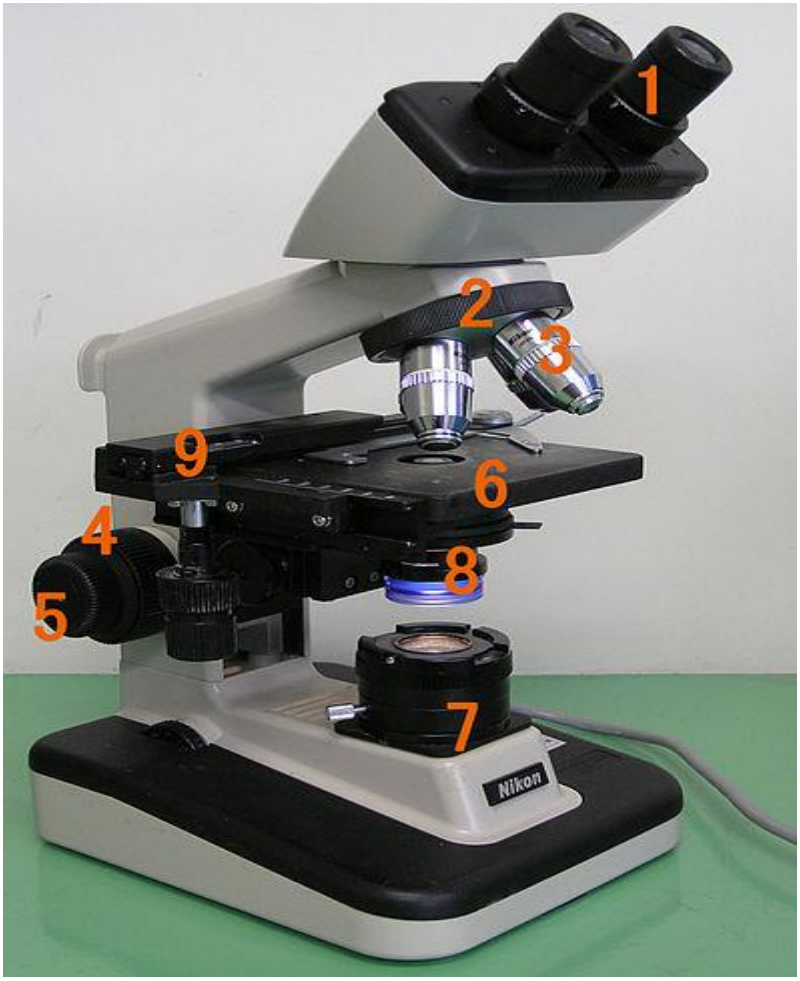

Figure 4.5: A typical optical microscope showing various components of the instrument. (www.en.wikipedia.org/wiki/Optical_microscope; 2013-09-30)

Some optical microscopes use oil-immersion or water-immersion objectives so as to improve resolution at higher magnification. This is because the refractive index of the oil or water is higher than that of air and therefore allows the objective to have larger numerical aperture (> 1)

so that the light is transmitted from the specimen to the outer face of the objective lens with minimal refraction. This allows for detection of smallest microstructural details in the sample. The adjustment knobs (fine knob (4) and coarse knob (5)) are used to move the stage (6) up and down, this operation helps to fine tune the clarity of the sample image under view. Below the objective is a stage which serves as a support platform for the specimen under view. The stage also possesses a hole at its centre to which light passes through to illuminate the sample. The light source (7) is commonly made of a halogen lamp although LEDs and lasers could also be utilized. The light passes through the diaphragm and condenser (8) which is effectively a lens designed to focus the illuminated light on to the sample. The condenser may include features such as filters to control the quality and intensity of the incident light (Richardson, 1971, Haynes, 1927-, Murphy, 2001). Illumination techniques such as cross-polarized light, dark field and phase contrast and others can be utilized to improve contrast of the image from the sample.

In carbon science, this technique is very vital in the microstructure studies of carbon materials especially graphite. This is because under polarized light the anisotropy of the graphitic lamellar structure can be detected using this technique. When visible polarized light interact with the graphite lamellar structure, it produces interference colours. These interference colours are significant because they inform about the orientation of graphite basal planes with respect to incident polarized light. When the retarder plate (1λ-plate) is inserted in the optical path, the basal planes appear in different colours as follows:

- basal planes aligned perpendicular to plane of polarization appears purple.
- basal planes oriented at an angle to the plane of polarization appear blue or yellow (the blue or yellow particles being indicative of filler particles perpendicular to each other) (Edwards, 1989).

The mounting resin which fills the pores of the filler particles appears purple under polarized light because it is optically non-textured. It does not change colour under polarized light when the stage is rotated. Poorly aligned region do not change colour as well (Nightingale, 1962).

4.5. Scanning Electron Microscopy (SEM)

This technique is used to characterize the microstructure of many materials including graphite and its composites. With SEM, a sample surface is scanned with high-voltage or energy beam of electrons. These electrons interact with electrons in the sample and the output thereof is a scan image revealing the microstructural features as well as composition of the sample. This technique also enables detection of surface impurities on samples. The disadvantage of this technique is that it requires the sample to be electrically conductive; otherwise the sample understudy should be coated with carbon coating or metal coating such as Gold or Platinum prior scanning to make it conductive. Secondary electrons (SE) and backscattered electrons (BSE) are the main signals produced by SEM. The latter are beam electrons that are reflected by sample by elastic scattering; the BSE is very useful in determination of elemental distribution in the sample surface. More information on this technique can be read in these references (McMillan, 1995, McMillan, 1988, Smith and Oatley, 1955).

4.6. Pycnometry

Pycnometry is a technique used in measuring the density and porosity of a solid material by either solid or gas displacement. There are three types of pycnometers, namely glass pycnometer, envelope pycnometer and gas pycnometer. The two latter ones were used in this work and more

focus was given to them. An envelope pycnometer measures the envelope/bulk density of the material by measurement of the bulk volume of the sample using displacement in a certain dry medium, e.g. dryflo medium (or sand). The envelope/bulk density of the material is calculated as the mass of the sample divided by the bulk volume. This method is non-destructive of the sample, is easily performed and it uses non-hazardous materials. However this method is inapplicable to powdered samples. Some instrument manufacturers refer to this method as Geopyc method (this method is also discussed in detail in Section 5.2.6).

On the other hand, the gas pycnometer determines the skeletal volume (and hence enables skeletal density calculation) of the solid or powdered sample by measuring the pressure change of gas in a calibrated volume. Gases such as nitrogen, helium, etc are used in these pycnometers. In this work Helium pycnometer was employed in measuring skeletal density. It is a constant-volume pycnometer consisting of essentially two inter-connected chambers (see Figure 4.5)one chamber is empty (expansion chamber, V_e) and the other one is having a sample of interest (sample chamber V_c having sample of volume V_s). The following steps are followed in principle to determine the volume of a sample:

- The sample of volume V_s is put in the sample chamber of volume, V_c
- The valve X and valve Y (gas supply valve) are open and the pycnometer is filled with helium

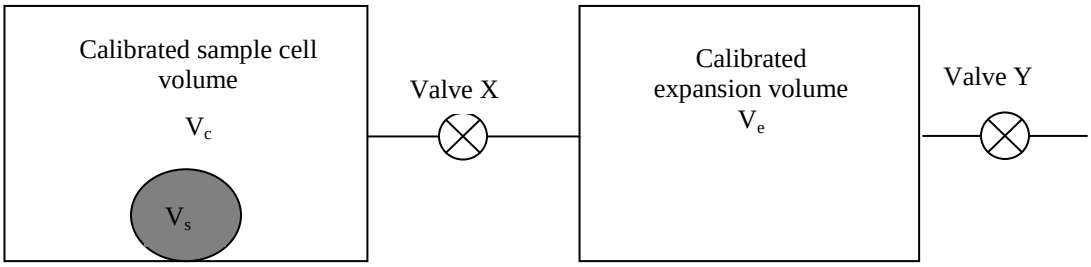

Figure 4.6: Simplified schematic diagram of a Helium pycnometer.

- The gas supply valve (valve Y) is closed and the absolute pressure (P_1) inside the pycnometer is measured using a transducer
- The valve X is then closed to isolate the sample chamber
- Valve Y is opened and the helium gas flows into the calibrated empty chamber
- Valve Y is closed again and the helium pressure in the empty chamber is measured (P_2)
- Valve X is opened and the gas expands into the sample chamber or vice versa
- When the expansion is finished, the final gas pressure is measured.

From these steps the volume of the sample is measured using pycnometer working equation as shown in equation (4.4):

$$V_s = V_c - \frac{V_e}{P_1 / P_2 - 1} \qquad (4.4)$$

This equation assumes the Helium gas behaves ideally; is not adsorbing on solid surface and is not compressible. To test whether the instrument works perfectly, standard steel balls of known volume are used to calibrate the volume at ambient temperature. More information on gas

pycnometers can be attained in these references (Tamari, 2004, Webb, 2001 , Micromeritics, 2009).

4.7. Thermogravimetric analysis

Thermogravimetric analysis (TGA) is a thermal analysis technique utilised to study the changes in physical and chemical properties of a material as a function of temperature at constant heating rate; or as a function of time at a constant temperature and/or mass loss (Wendlandt, 1964, Brown, 2001). The resulting information from TGA scan is, for example, a residual mass loss vs. temperature curve which provides information regarding thermal stability, air oxidation and composition of the original sample, intermediates and residue. The sample weight/mass change in the instrument is monitored using a thermobalance which consist of electronic microbalance, a furnace, a temperature controller, an atmospheric controller and a connected PC which records the output from these devices (Brown, 1988, Wendlandt, 1964). In this project, a mettler Toledo A851 TG/SDTA machine was used during air oxidation measurements on raw graphite and composite samples.

4.8. Thermomechanical analysis

Thermomechanical analysis (TMA) is a thermal analysis technique which studies the properties of materials when they are subjected to a change in temperature. The primary signal in this technique is the dimension change in the sample as it is heated or cooled (Haines, 1995). A schematic diagram of a typical TMA instrument is shown in Figure 4.6 below. Basically a sample is placed on top of a support material and a probe (both made of a quartz glass) sits on top of the sample. Quartz glass is preferably used due to its low thermal conductivity and

expansion. The geometry of both the sample and probe are such that they are placed within the furnace as shown. Next to the sample is a temperature monitoring device, a thermocouple, which measures the temperature of the sample during heating or cooling. The probe is connected to a Linear Variable Displacement Transducer (LVDT) which monitors and records the dimension changes in the sample (Fifield and Kealey, 1995). Measurements are normally performed under the flow of an inert gas such as nitrogen or helium gas to prevent air oxidation during the heat-treatment or cooling. The probe should at least touch the sample in order to obtain error-free data. To do this, the measurements are performed under zero load or under very negligible load. Various types of probes can be used: expansion, penetration, tension, flexure, etc; depending on what the user intends to measure (Brown, 1988), (Fifield and Kealey, 1995). For example, an expansion probe is used when one is interested in measuring linear coefficient of expansion whilst the penetration probe is utilized when one measures the glass transition temperature (also called T_g) of a material. A calibration with a material(s) of known CTE or T_g value is required prior to analysis. TMA instruments are capable of taking measurements in the temperature range -100 to 1000 °C. The measurements can also be obtained at variable loads.

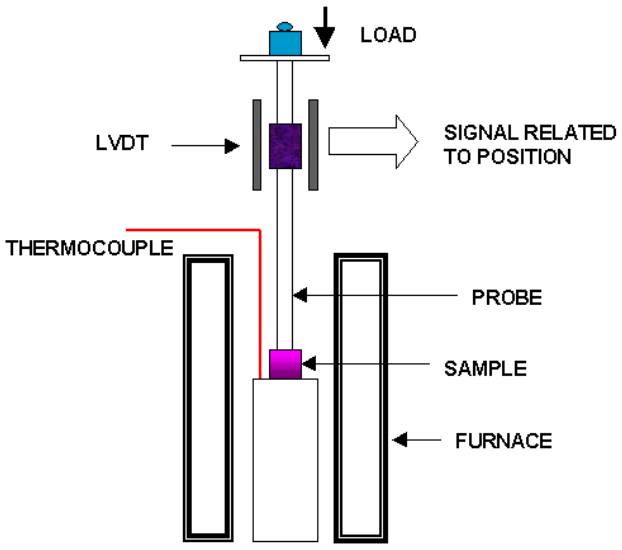

Figure 4.7: A schematic diagram of a typical TMA instrument.

4.9. Xenon Flash Photolysis

Xenon flash photolysis is a specialized laser flash method used to measure thermal diffusivity of a sample subjected to a high energy Xenon pulse on one end and monitoring the temperature rise of the sample on the other end (Parker et al., 1961, Clark and Taylor, 1975b). In principle, an energy pulse is incident on one side of the sample (as shown in Figure 4.7) and the time dependent temperature signal is detected on the back side of the sample. If the measurement is performed in one-dimension as shown in Figure 4.7 and under constant pressure, the thermal diffusivity of the sample can be calculated as follows:

$$\alpha = 0.1388\frac{d^2}{t_{1/2}} \qquad (4.5)$$

where α is the thermal diffusivity, d is the sample thickness and $t_{1/2}$ is the time required for the pulse to reach its half maximum value.

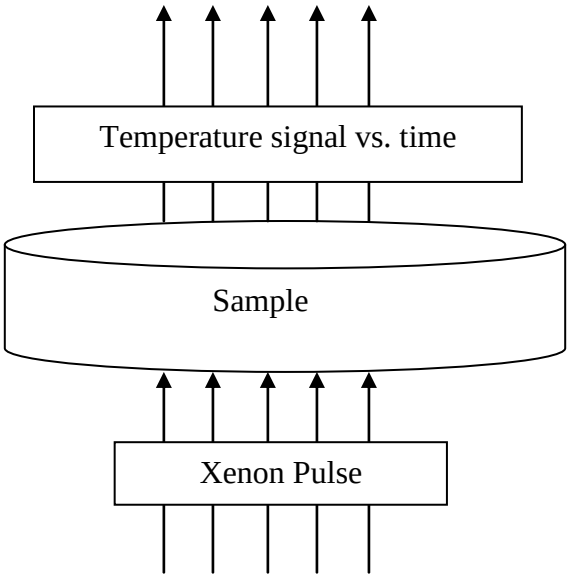

Figure 4.8: A diagram showing how Xenon Flash measurement works.

This technique requires the sample to be homogeneous; the energy pulse input must also be uniform and very short (typically in micro-seconds). Thermal diffusivity measurements are very helpful in the indirect measurement of the thermal conductivity of a material. The relationship between these properties is as follows:

$$\kappa = \rho C_p \alpha \tag{4.6}$$

where κ is the thermal conductivity in W m^{-2} K^{-1}, α is the thermal diffusivity in m^2 s^{-1}, ρ is the density in kg m^{-3} and C_p is the specific heat in J kg^{-1} K^{-1}. Combining equations (4.5 and 4.6) gives the thermal conductivity expression as follows:

$$\kappa = 0.1388 \frac{d^2 \rho C_p}{t_{1/2}} \tag{4.7}$$

4.10. Four-point bending

The four-point bending test method is used to test the flexural or bending strength of brittle materials. Flexural strength is defined as the ability of the material to resist deformation when a load is applied on it. It represents the highest stress it experiences at the moment of rupture. It is measured as force per unit area or simply it is expressed in pressure units such as MPa. Figure 4.8 below shows a four-point loading beam of a rectangular sample. When the load is applied on the sample, it experiences various stresses, i.e. compressive stress on the loaded side (top side) and a tensile stress on the other side (below the sample). Most materials fail under tensile stress than compressive stress.

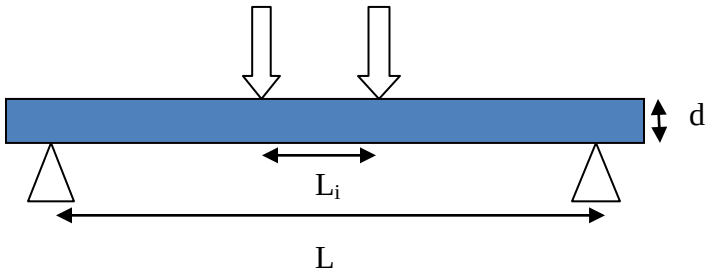

Figure 4.9: Beam with four-point loading.

For a rectangular sample under four-point bending load the strength is calculated as follows:

$$\sigma = \frac{FL}{bd^2} \tag{4.8}$$

where σ is the flexural strength in Pa, F is the applied load at fracture in N, L is the support span length in m, b and d are the sample width and thickness, respectively, in m. The formula in equation (4.8) applies only if the load span length (L_i) is one-third of the support span length (L). If the load span is half the support span, the flexural strength is given by:

$$\sigma = \frac{3FL}{4bd^2} \tag{4.9}$$

If the load span is neither one-third nor half of the support span then the strength is given by:

$$\sigma = \frac{3F(L - L_i)}{2bd^2} \tag{4.10}$$

A different formula for calculating strength applies for samples tested using three point bending fixtures and this can be attained in literature (Hodgkinson, 2000). Factors affecting strength and modulus are defects in the material, its porosity, particle size, inter-particulate binding, etc. In this work the graphitic composites samples tested were in accordance with an ASTM standard C651-91 (Reapproved 2000).

References

BRAGG, W. H. & BRAGG, W. L. (1913) The structure of the diamond. *Nature,* 91**,** 557.

BROWN, M. E. (1988) *Introduction to thermal analysis,* New York, Chapman & Hall.

BROWN, M. E. (2001) *Introduction to thermal analysis: techniques and Applications,* Dordrecht/ Boston/ London, Kluwer Academic Publishers.

CULLITY, B. D. (1978) Diffraction I: Directions of Diffracted Beams. IN COHEN, M. (Ed.) *Elements of X-ray diffraction.* Second Edition ed. Reading, Massachusetts, Menlo Park, California, London, Amsterdam, Don Mills, Ontario, Sidney Addison-Wesley Publishing Company, INC.

CLARK, L. M. & TAYLOR, R. E. (1975) Radiation loss in the flash method for thermal diffusivity. *Journal of Applied Physics,* 46**,** 714-719.

DRESSELHAUS, M. S., DRESSELHAUS, G., SAITO, R. & JARIO, A. (2004) Raman spectroscopy of carbon nanotubes. *Physics Reports,* 409**,** 47-99.

DRESSELHAUS, M. S., JORIO, A., HOFMAN, M., DRESSELHAUS, G. & SAITO, R. (2010a) Perspectives on carbon nanotubes and graphene Raman spectroscopy. *Nanoletters,* 10 751-758

DRESSELHAUS, M. S., JORIO, A. & SAITO, R. (2010b) Characterizing graphene, graphite and carbon nanotubes by Raman Spectroscopy. *Annual Review of Condensed Matter Physics,* 1**,** 89-108.

EDWARDS, I. A. S. (1989) Structure in Carbons and Carbon Forms. IN MARSH, H. (Ed.) *Introduction to Carbon Science.* London, Butterworths.

FERRARI, A. C. & ROBERTSON, J. (2004) Raman spectroscopy of amorphous, nanostructured, diamond-like carbon, and nanodiamond. . *Philosophical Transactions of Royal Society A.*, 362**,** 2477-2512.

FIFIELD, F. W. & KEALEY, D. (Eds.) (1995) *Principles and Practice of Analytical Chemistry*, Glasgow, Blackie Academic and Professional.

HAINES, P. J. (1995) *Thermal methods of analysis; Principles, Applications and Problems,* Glasgow, Blackie Academic and Professional.

HAYNES, R. (1927-) *Optical microscopy of Materials*, Glasgow International.

HERGERT, W. & WRIEDT, T. (2012) *The Mie Theory*, Berlin Heidelberg, Springer-Verlag.

HODGKINSON, J. M. (2000) Flexure. IN HODGKINSON, J. M. (Ed.) *Mechanical Testing of Advanced Fibre Composites.* London, Cambridge: Woodhead Publishing, Ltd.

HODKIEWICZ, J. (2013) Characterizing carbon materials with Raman Spectroscopy. Madison WI, USA, Thermo Fischer Scientific Inc.

KELLY, B. T. (1981) Physics of Graphite. London and New Jersey, Applied Science Publishers.

KLUG, H. P. & ALEXANDER, L. E. (1954) *X-ray procedures for polycrystalline material,* New York, Wiley.

LIPSON, H. & STOKES, A. R. (1942) *Procedings of the Physics Society of London,* A181**,** 101.

MCMILLAN, D. (1988) Von Ardenne and the scanning electron microscope. *Proceedings of the Royal Microscopy Society*.

MCMILLAN, D. (1995) Scanning Electron Microscopy 1928-1965. *Scanning,* 17**,** 175-185.

MICROMERITICS (2009) Micromeritics Accupyc II 1340 Pycnometer. www.youtube.com. (2010-09-16)

MIE, G. (1908) Beiträge zur Optik trüber Medien, speziell kolloidaler Metallösungen. *Annalen der Physik,* 330**,** 377-445.

MURPHY, D. B. (2001) *Fundamentals of Light Microscopy and Electronic Imaging*.

NAKAMIZO, M., KAKKERECK, R. & P.L., W. (1974) Laser Raman studies on carbons. *Carbon,* 12**,** 259-267.

NIGHTINGALE, R. E. (1962) *Nuclear graphite,* London, Academic press.

PARKER, W. J., JENKINS, R. J., BUTLER, C. P. & ABBOT, G. L. (1961) Flash method of determining thermal diffusivity, heat capacity and thermal conductivity. *Journal of Applied Physics,* 32**,** 1679-1684.

PARTHASARAY, G., SREEDHAR, B. & CHETTY, T. R. K. (2006) Spectroscopic and X-ray diffraction studies on fluid deposited rhombohedral graphite from the Eastern Ghats mobile belt, India. *Current Science,* 90**,** 995-1000.

PRAWER, S. & NEMANICH, R. J. (2004) Raman spectroscopy of diamond. *Philosophical Transactions of Royal Society A.,* 362**,** 2537-2565.

RICHARDSON, J. H. (1971) *Optical Microscopy for the Materials Sciences,* New York, MARCEL DEKKER, INC.

RULAND, W. (1965) X-ray studies on the structure of graphitic carbons. *Acta Crystallographica,* 18**,** 992-996.

SCHERER, P. (1918) Bestimmung der Größe und der inneren Struktur von Kolloidteilchen mittels Röntgenstrahlen. . *Göttinger Nachrichten,* 2**,** 1.

SCHETTINO, V., PAGLIAI, M. & CARDINI, G. (2002) The Infrared and Raman spectra of fullerene C70. DFT calculations and correlation with C60. *Journal of Physical Chemistry A.,* 106**,** 1815-1823.

SMITH, K. C. A. & OATLEY, C. W. (1955) The scanning electron microscope and its field of application. *British journal of applied physics* 6**,** 391-399.

TAMARI, S. (2004) Optimum design of constant-volume gas pycnometer for determining the volume of solid particles. *Measurement Science and Technology,* 15**,** 549-558.

TRUCANO, P. & CHEN, R. (1975) *Nature,* 258**,** 136.

TUINSTRA, F. & KOENIG, J. L. (1970) Raman spectrum of graphite. *Journal of Chemical Physics,* 53**,** 1126-1130.

WANG, Y., ALSMEYER, D. C. & MCCREERY, R. L. (1990) Raman spectroscopy of carbon materials: structural basis of observed spectra. *Chemistry of Materials,* 2**,** 557-563.

WARREN, B. E. (1941) X-ray diffraction in random layer lattices. *The Physical Review,* 59**,** 693-698.

WEBB, P. A. (2001) Volume and Density Determinations for Particle Technologists. Micromeritics Intruments Corporation.

WENDLANDT, W. W. (1964) *Thermal methods of analysis,* New York, Interscience Publishers.

CHAPTER 5: EXPERIMENTAL

5.1. Raw Materials

The raw materials used to fabricate graphitic composites in this work were natural graphite (NG), synthetic graphite (SG) or electro graphite and a phenolic resin binder. These materials were supplied to our laboratory by PBMR (Pty) Ltd and their origin and manufacture are proprietary and therefore information as to how they were made and their grades was not available due to confidentiality agreement with their suppliers.

5.2. Fabrication

Graphite composites containing a fixed amount of novolac phenolic resin binder (20 wt.%) were fabricated according to the procedure outlined in Figure 5.1. The compositions of the graphite composites made are shown in Table 5.1. They were labelled according to the proportions of natural flake graphite (NG), synthetic graphite (SG) and novolac binder in wt.%. For example, the composite containing 64 wt.% natural graphite, 16 wt.% synthetic graphite and 20 wt.% phenolic resin was labelled 64:16:20, etc.

The appropriate amounts of the natural flake graphite (NG) and synthetic graphite (SG) powders were mixed in a Z-blade mixer (Jones Mixers, South Africa) for one hour. A methanol solution of the phenolic novolac resin was then added. Just sufficient methanol was used to ensure a flowable paste. This resinated paste was dried at 70 °C for 6 h in a convection oven. The resulting rigid residue was then ground into a powder using a carbon steel ring mill and sieved through 212 μm mesh using electromagnetic shakers (Labotec, South Africa). About 120 g sieved powder was placed in a 100 mm ϕ cylindrical stainless steel die. Disc-shaped test

specimens were compression moulded for 1 h at 13 MPa in a hydraulic press (Vertex Automation Pty (Ltd)).An example of the green graphite composite sample attained after pressing is shown in Figure 5.2. The green moulded specimens were then carbonised at 900 °C in N_2 atmosphere to remove all volatiles. This was followed by an annealing step at 1800 °C in a helium atmosphere using a graphitising furnace (Thermal Technology Inc., USA). The samples were maintained at this temperature for 2 h and then allowed to cool to ambient conditions. Depending on the measurement to be made, the samples were cut to the required dimensions with an Isomet 4000 linear precision diamond saw (Buehler, Germany).

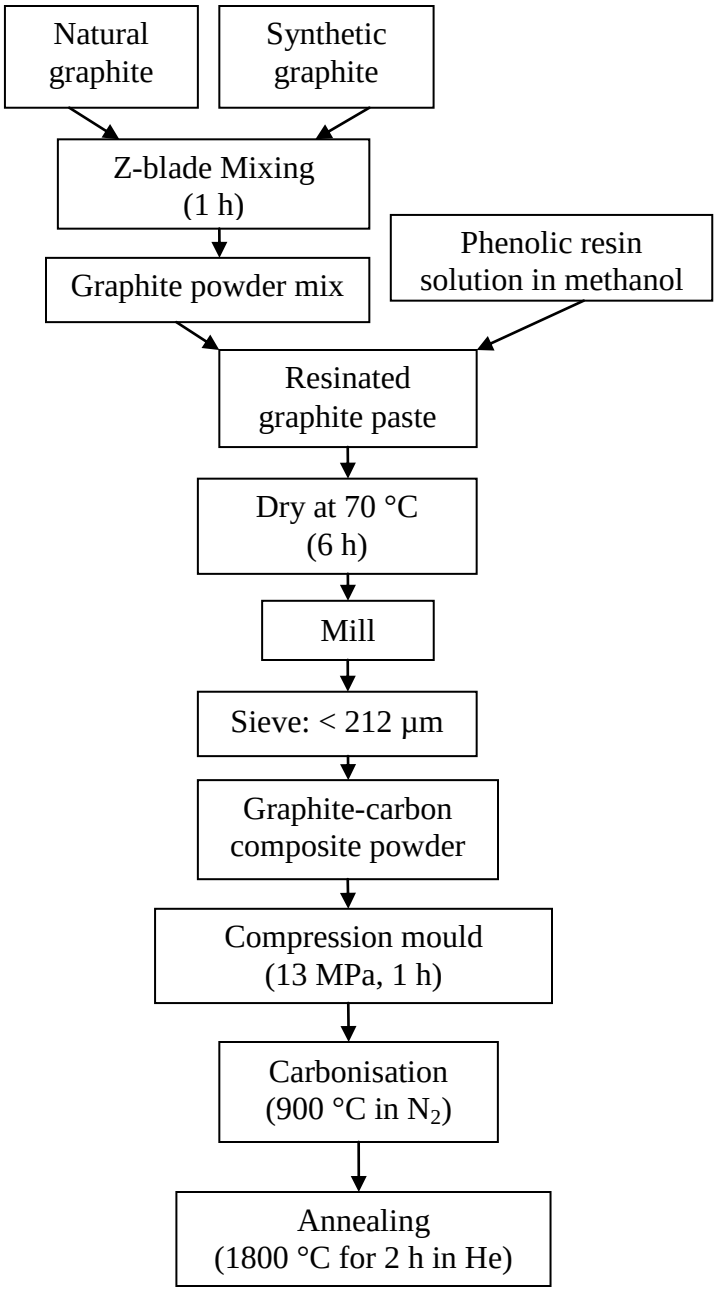

Figure 5.1: Fabrication scheme of the graphite-carbon composites.

Table 5.1: Graphite-carbon resin composites fabricated in this work.

Composition (NG:SG:novolac)	**Natural graphite (NG) content (wt.%)**	**Synthetic graphite (SG) content (wt.%)**	**Phenolic resin content (wt.%)**
0:80:20	0	80	20
16:64:20	16	64	20
40:40:20	40	40	20
64:16:20	64	16	20
80:0:20	80	0	20

Figure 5.2: A disc-shaped unheated or green test sample obtained after uniaxial compression moulding.

5.3. Characterisation of the graphite composites.

The crystal structure, microstructure and properties of the raw materials and moulded annealed graphite samples were characterised using various techniques. The methodologies employed in the characterisation were outlined as follows.

5.2.1 Particle Size Distribution

The particle size distribution of the sieved (<212 µm) powdered graphite composites and the precursor graphites were measured by a mastersizer2000 from Malvern instruments using distilled water as dispersing medium. The instrument uses a blue laser source having power of 0.3 mW.

5.2.2 X-ray diffraction

The diffraction patterns were recorded using a BRUKER's D8 ADVANCE powder diffractometer. Measurements were done using CuKα radiation, with the generator operated at 40 kV and 40 mA. Detection of the diffracted beam was done using 1 D Position Sensitive Detector (Lynx eye detector). The samples were loaded into the sample holders and flattened (X-ray beam was incident on flat pressed sample surface). Measurements were performed in the range 15-90° in 2θ with 0.04° step size, counting time 0.2 s. Phase identification was done using EVA's [ref: Diffrac^{plus} Basic evaluation Package User manual release 1998] SEARCH & MATCH in conjunction with ICDD 2007 PDF-2 database. The peak widths were calculated using TOPAS v4.2 [ref: Diffrac^{plus} TOPAS User manual]. The interlayer spacing (d_{002}) and the

degree of graphitisation (g) were calculated using the Bragg equation (4.1) and equation (4.2), respectively. A copper radiation source of wavelength, λ equal to 0.15418 nm was used.

5.2.3 Raman Spectroscopy

The Raman spectra were recorded with the T64000 series II triple spectrometer system from HORIBA Scientific, Jobin Yvon Technology using the 514.3 nm laser line of a coherent Innova®70 Ar^+ laser with a resolution of 2 cm^{-1}in the wavenumber range 1200 to 1750 cm^{-1}. The samples were recorded in a backscattering configuration with an Olympus microscope attached to the instrument (using a LD 50× objective). A liquid nitrogen-cooled CCD detector was used with the laser power of 6 mW at the sample. The accumulation time was 120 s and the spectra were baseline corrected with the use of the LabSpec software program. All the spectra were collected at a spot scale of 2 µm.

5.2.4 Optical microscopy

The microstructure of the raw graphite samples and heat-treated moulded graphite composites was studied by optical microscopy (OM) under reflected and polarised light. The samples were mounted in an epoxy resin and hardener (5:1v/v, respectively), they were then vacuumed out for 10 minutes to remove the air from the sample and to allow the resin to penetrate the sample. The samples were polished with a Buehler Alpha 2 speed grinder-polisher with a continuous flow of water for 1 min for each of the silicon carbide grinding papers (400, 600, 1200 grits).The samples were then successively polished with Buehler Metadi polishing suspensions of size 1.0

μm and 0.05 μm. This was done for 3 and 5 min, respectively. This polishing methodology yielded very smooth sample surfaces. All the polishing equipments were supplied by Buehler®. The polished samples were then mounted on the glass slide with plasticine using a manual mounting press to obtain surface evenness; the polished surface was protected by a lens tissue during pressing. The samples were analysed using a Leica DM 2500 M microscope under reflected and polarized light at different magnifications.

5.2.5 Scanning electron microscopy

The graphite samples were mounted on an aluminium holder as follows; first, the carbon double-sided adhesive tape was placed onto the holder and another single-sided adhesive tape was used to mount the graphite. This was then adhered to the tape already on the aluminium holder, the excess powdered graphite particles which did not adhere to the tape were removed. The solid samples adhered onto the carbon tape with ease. A conductive carbon paint made of colloidal graphite mixed with isopropyl alcohol was applied on the samples adhered onto the tape to make the samples conductive. The morphology of the samples was determined using an ultrahigh field emission SEM (HR FEGSEM Zeiss Ultra Plus 55) with an InLens detector at an acceleration voltage of 2 kV.

5.2.6 Pycnometry

The bulk density of the pre-weighted moulded annealed graphite composite samples was measured using a Geopyc 1360 pycnometer purchased from Micromeritics Instruments

Corporation, USA. The Geopyc 1360 uses the displacement of a sample in a dry medium to determine the bulk volume of the test sample, see Figure 5.3. First the zero-volume baseline was determined by applying a force of 145 N to a precision glass cylinder containing only the dry medium (dryflo). This was done in 3 cycles (i.e. three times). Thereafter a pre-weighted sample was placed in the dryflo and the same amount of force was applied in 3 cycles (three times). The volume of the displaced medium relative to the baseline gives the bulk volume of the inserted sample as follows:

$$V_s = V_t - V_0 = \pi r^2 (h_t - h_0) \qquad 5.1$$

where V_s = sample volume, V_t = total volume after displacement, V_0 = baseline volume, h_t = total height after displacement and h_0 = baseline height.

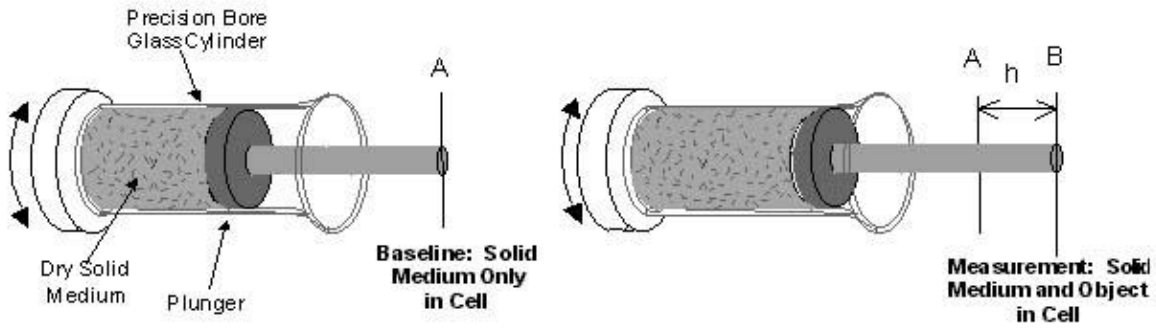

Figure 5.3: Determination of bulk volume by displacement of dry medium (Webb, 2001).

The apparent skeletal (or Helium) density of the moulded annealed graphite samples was measured using an Accupyc II 1340 V1.03 He pycnometer purchased from Micromeritics Instruments Corporation, USA. The volume of the sample cup was calibrated prior analysis by

filling it with He gas until it reaches a pressure of 134.45 kPa, this was done in 5 cycles. Thereafter two standard steel balls of known volume were inserted into the sample chamber and the same amount of pressure was applied in 5 cycles. After the calibration the pre-weighed sample was placed into the sample cup and the same pressure was applied same number of times. The sample volume was measured by displacing the He gas until it reaches a pressure of 134.45 kPa; the volume of the sample was calculated as the volume of He gas displaced in the sample cup. The apparent density (or He density) of the sample was then calculated from its mass and the measured volume (Micromeritics, 2009). The percentage open porosity was calculated using the following equation:

$$\%Openporosity = \left(1 - \frac{\rho_B}{\rho_{He}}\right) \times 100\% \qquad (5.2)$$

where ρ_B is the bulk density and ρ_{He} is the helium density.

Triplicate measurements were performed per sample and three samples were measured per type or composition (therefore 9 measurements per composition).

5.2.7 Thermogravimetric analysis (TGA)

The air oxidation behaviour of the powdered raw graphite samples, the novolac phenolic resin and the annealed graphite composites was determined by TG analysis using a mettler Toledo A851 TG/SDTA machine. About 20 mg samples were placed in a 70 µl alumina pan and heated from 18 to1000 °C at scan rate of 5 °C/min in instrument grade air flowing at 50 ml/min. No sample pre-treatment was performed.

5.2.8 Thermomechanical (TMA) analysis

The linear coefficients of thermal expansion (CTE) of the annealed solid composites were determined in expansion mode with a TA Instruments TMA Q400 V22.1 analyser. The runs were made on a quartz stage from 20 to 600 °C at a heating rate 5 °C/min in N_2 flowing at a rate 50 ml/min and applying a force of 0.05 N. The dimensions of the samples used were 10 mm × 5 mm × 5 mm. The true or instantaneous thermal expansion coefficient, CTE was calculated as follows:

$$CTE, \alpha = \frac{1}{L_0}\frac{\partial L}{\partial T} \tag{5.3}$$

where L is the length of the sample in m, T is the temperature in K and L_0 is the initial length of the sample in m at some initial temperature T_0 (Hacker et al., 2000). The instantaneous CTE value is in principle the slope of the tangent at a particular temperature in the length change vs. temperature curve. The mean or average linear thermal expansion coefficient was calculated as the slope of the chord in the length change vs. temperature curve between 20 and 600 °C. At least three measurements per sample were done both parallel (∥) and perpendicular (⊥) to the direction of the pressing force. The instrument was calibrated using a copper sample with known linear CTE ($17\times10^{-6}K^{-1}$).

5.2.9 Xenon Flash Photolysis

The thermal conductivity of the annealed graphite composites samples were indirectly measured using the Xenon flash method. The thermal diffusivity was measured at each temperature using the Clark and Taylor analysis of a back face thermogram generated from a Xenon flash on the

front face(Clark and Taylor, 1975a). Samples of 20 mm in diameter and 2 mm in thickness were used in an Anter Flashline 3000 with a Xenon flash under nitrogen flow. A thermographite sample was used as a reference. The thermal conductivity of the samples was calculated from measured thermal diffusivity, density and specific heat of the samples at each temperature using equation (4.6).

5.2.10 Four-point bending tests

Rectangular annealed graphite composite samples were cut to the specifications of ASTM Standard C651-91 (Reapproved 2000). The length of the samples were 40.00±0.02 mm, their widths were 10.00±0.02 mm and had thickness of 5.00±0.02 mm. The samples were polished on their faces with 1200 silicon carbide paper grit to make them smooth and free of visible defects. The samples were loaded onto a tensile tester (LRX plus tensile tester, LLOYD Instruments); the support and loading spans used were 30 and 10 mm, respectively. A loading rate of 1 mm/min was utilised. All samples tested were unnotched. The flexural strength was calculated using equation (4.8). At least triplicate measurements were performed for each composition.

References

CLARK, L. M. & TAYLOR, R. E. (1975) Radiation loss in the flash method for thermal diffusivity. *Journal of Applied Physics*, 714-719.

HACKER, P. J., NEIGHBOUR, G. B. & MCENANEY, B. (2000) The coefficient of thermal expansion of nuclear graphite with increasing thermal oxidation. *Journal of Physics D: Applied Physics*, 33, 991-998.

MICROMERITICS (2009) Micromeritics Accupyc II 1340 Pycnometer. www.youtube.com. (04-November-2009)

NIGHTINGALE, R. E. (1962) *Nuclear graphite*, London, Academic press.

WEBB, P. A. (2001) Volume and Density Determinations for Particle Technologists. Micromeritics Intruments Corporation.

CHAPTER 6: RESULTS AND DISCUSSION-CHARACTERISATION

6.1. Fabrication

The moulded graphite composites having various weight ratios of natural flake and synthetic graphites were fabricated. Sample discs of diameter 100 mm were made; see an example in Figure 5.2. The incorporation of novolac phenolic resin binder is essential because compression moulding of the graphite powders or their mixtures without it did not yield monolithic structures. Similar behavior for such graphite composites has been reported, although a lower binder level (10 wt %) was used (Cunningham et al., 2005). The addition of the novolac phenolic resin in the form of a methanol solution ensured a more uniform distribution of the resin in the graphite than would have been possible by dry solid addition. The milling of the dried samples also aided, to some extent, homogeneous distribution of the binder resin and graphite powder particles.

The fabrication steps of the graphite matrix composites used in this work is different from those used in gas cooled reactors, as discussed in Section 2.5. For example, the matrix material used in the German AVR (A3-3 or A3-27) was made using cold quasi-isostatic pressing at high pressure of approximately 300 MPa, carbonization at a temperature of 800 °C and annealing in vacuum at 1800 °C (Schulze et al., 1981) (Hoinkis and Robens, 1989) whislt the matrix developed in this work was cold compression molded at 13 MPa, carbonized at 900 °C in N_2 and then annealed in vacuum at 1800 °C for 2 h. Also the Chinese HTR-10 which uses the A3-3 matrix was made using a method similar to that of the German AVR (Tang et al., 2012) (Tang et al., 2008) (Tang et al., 2002). These differences in the processing steps and parameters would lead to different

properties in the composites. The differences in fabrication steps of the graphite composites made in this work and those reported in literature will in fact result in different properties.

Having made the samples it was very critical to characterise them in order to check their quality and structural features. Graphite composites characterisation is very essential because it gives one the sense of what is the quality of the samples made in any manufacturing or processing. In this chapter, the focus was on the quality assessment of the raw materials and the graphitic composites fabricated. Techniques used for characterisation were X-ray diffraction (XRD), Raman Spectroscopy, Optical Microscopy (OM), Scanning Electron Microscopy (SEM) and Pycnometry.

6.2. Particle Size Distribution of the graphite composites

The particle size distribution of the graphite powders and annealed graphite composite powder mixtures are shown in Figure 6.1. The natural graphite powder (100:0:0) showed lower particle size distribution than other materials. Its particle sizes range from 0 to 150 µm and it had mean particles size of 30.6 µm, see Table 6.1. On the other hand, the particle sizes for the raw synthetic graphite powder (0:100:0) ranged from 0 to 200 µm having a mean particle size of 48.8 µm. The particle size distributions of the graphite composites were broader than those of the graphite precursors. There was a shift in particle size range towards larger values for composites compared to the raw graphite powders. For example, a greater volume percentage of particles having particle sizes greater than 75 µm were mainly observed in the graphitic composites. This showed that some agglomeration of the particles has occurred.

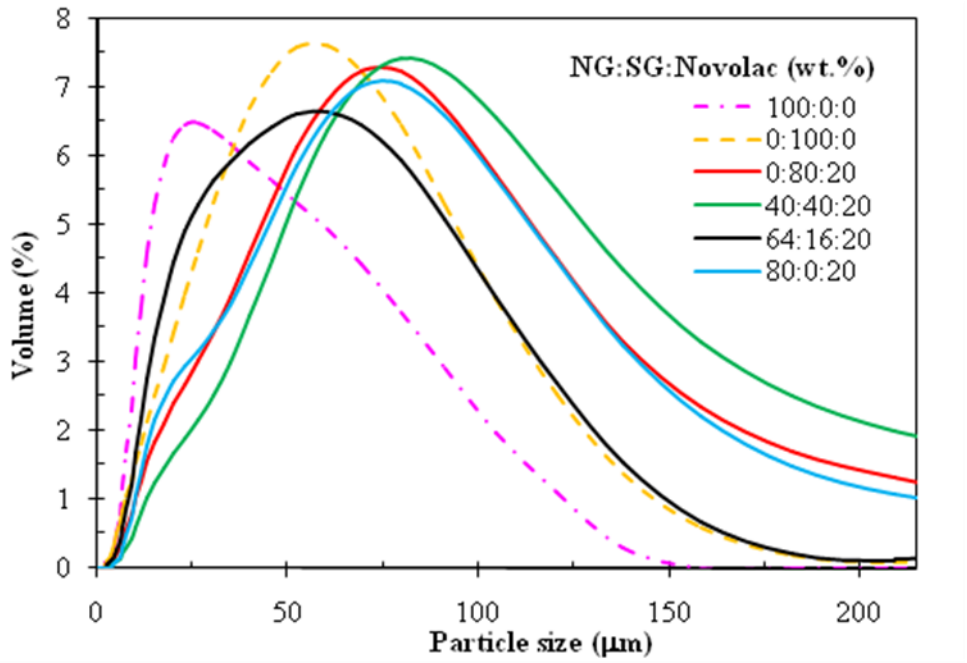

Figure 6.1: Particle Size Distribution of the precursor graphites and annealed graphite composite powders.

Addition of the novolac phenolic resin to the natural graphite powder sample resulted in the increase in the mean particle size to 70.8 µm. The synthetic graphite sample showed a similar increase to 70.6 µm. This increase in the mean particles sizes confirms that the addition of the binder resin to the graphites result in the agglomeration of the graphite particles. A composite containing equal amount of the graphite fillers and binder showed larger mean particle size value of 87.7 µm. It is interesting to note that the composite containing 64:16:20 wt.% ratios had smaller mean particle size.

Table 6.1: The mean particle sizes of raw graphites and annealed graphite composites.

Composition NG:SG:Novolac (wt.%)	Mean particle size (µm)
100:0:0	30.6
0:100:0	48.8
0:80:20	70.6
40:40:20	87.6
64:16:20	43.9
80:0:20	70.8

6.3. X-Ray Diffraction analysis of the graphite composites

The crystal structure and the degree of graphitisation are very key aspects/parameters in the characterisation of graphitic materials. One requirement for use of graphites or graphite composites in high temperature nuclear reactor applications is that it must be highly crystalline. The X-ray diffraction patterns of the as-received graphite powders and the solid annealed graphite composites are shown in Figure 6.2. The patterns for all the annealed composites, as well as that of the SG (0:100:0), were consistent with the hexagonal crystalline phase of graphite (Trucano and Chen, 1975). The NG (100:0:0) pattern corresponded to the graphite-3R pattern which contains both the hexagonal and rhombohedral crystalline phases. The latter phase possesses additional peaks at 2θ = 43.4, 46.2 and 56.6° (Lipson and Stokes, 1942a). It is well known that the hexagonal phase is the more stable phase and that the rhombohedral phase is thermodynamically unstable (Kelly, 1981a). The presence of the latter phase in the NG could have been caused by the milling operation used during its comminution. The rhombohedral phase results from stacking faults of the hexagonal phase (Kelly, 1981a, Parthasaray et al., 2006). Owing to an annealing effect, this phase did not appear in the profiles of the heat-treated composites, especially those containing mainly NG and the binder (Kelly, 1981a). All the

composites showed a hexagonal crystal graphite structure after annealing. The reflection at $2\theta \approx 30°$ could not be assigned but may be an instrument artefact. This reflection did not appear in the patterns of the raw graphite samples and in the annealed graphite composite powders (see Figure 6.3). The interlayer spacing (d_{002}) values and the degree of graphitisation (g) of the graphite powders and the annealed graphite composites calculated using equation (4.1) and (4.2); respectively, are shown in Table 6.2.

The interlayer spacing (d_{002}) of the raw natural flake and synthetic graphites as determined by XRD were 0.3357 and 0.3354 nm, respectively. Their degree of graphitisation was 0.96 and 0.99, respectively. Thus the raw graphite powders featured interlayer spacing values close to that of the ideal single crystal graphite (Ruland, 1965). In fact these graphites were very crystalline when compared to other nuclear grade graphites such as PGA, IG110 and UcarC; their degree of graphitisationwere reported as 0.91, 0.74 and 0.84, respectively (Fazluddin, 2002). The annealed graphite composites showed larger average interlayer spacing values (i.e. 0.3364 to 0.3371 nm) than the raw graphite powders.

This is attributed to defects introduced during the milling of the green compound and the high pressure moulding process used to make the samples. The presence of the non graphitic phenolic resin carbon also resulted in the increase in the interlayer spacing in the composites even though they were heat-treated to 1800 °C. This is clearly confirmed by the decrease in the degree of graphitisation of the graphite powders upon addition of the novolac phenolic resin binder and subsequent heat-treatment. The SG is the most affected in this case because its degree of graphitisation decreased by 19 % whilst that of the NG decreased by 7 %.

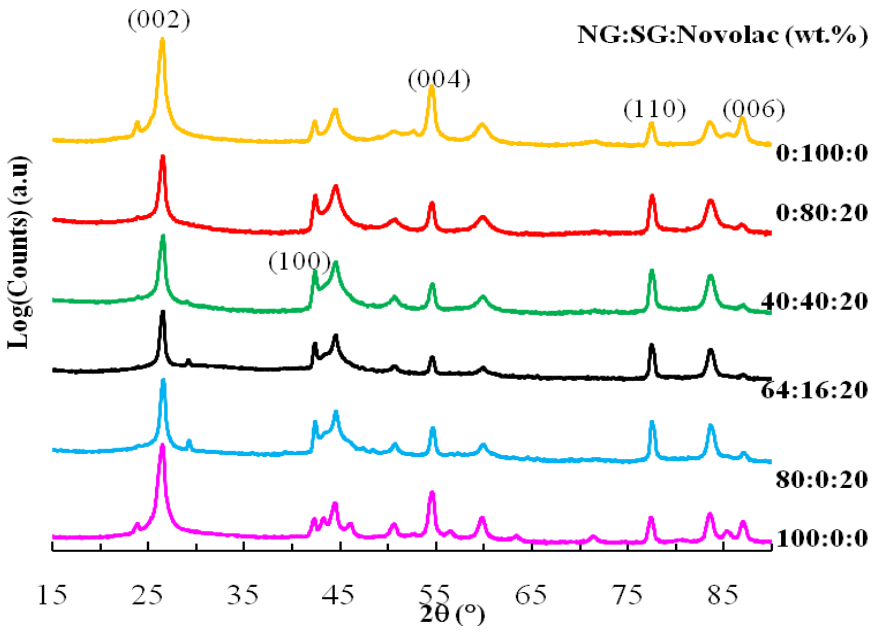

Figure 6.2: The X-ray diffraction patterns of raw graphite powders and solid annealed graphite-resin composites of various compositions heat-treated to 1800 °C in a helium atmosphere.

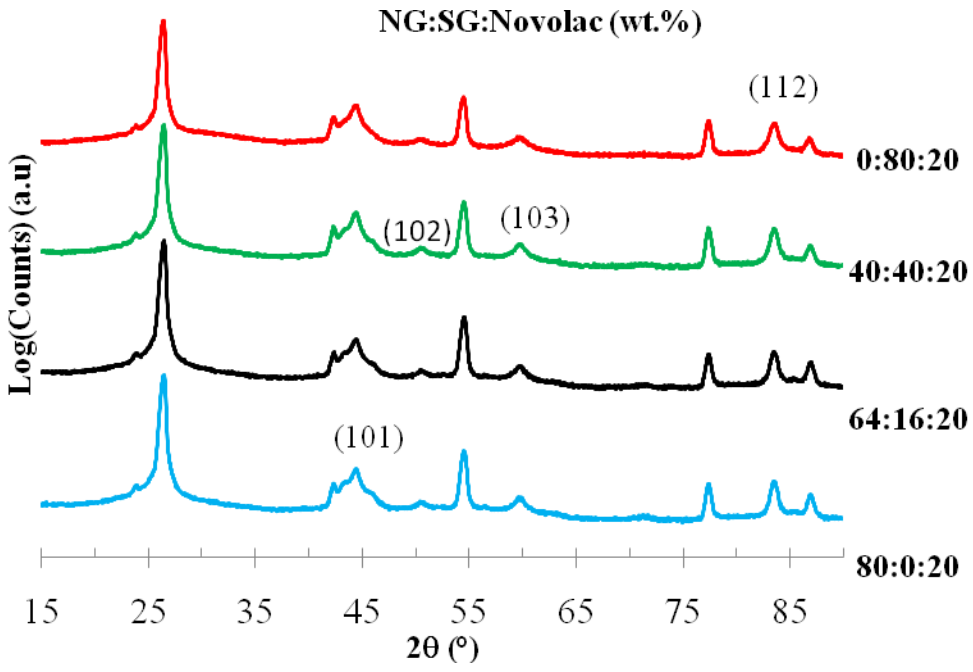

Figure 6.3: The X-ray diffraction patterns of the annealed graphite-resin powdered composites heat-treated at 1800 °C in He atmosphere.

Table 6.2: The interlayer spacing (d_{002}) and degree of graphitization (g) of the raw graphites and annealed graphite composites.

Composition (NG:SG:Novolac)	**2θ (°)**	**d_{002} (nm)**	**g -**
100:0:0	25.539	0.3357	0.96
0:100:0	26.562	0.3354	0.99
0:80:20	26.437	0.3371	0.80
40:40:20	26.443	0.3370	0.81
64:16:20	26.438	0.3371	0.80
80:0:20	26.497	0.3364	0.89
PGA[a]	26.492	0.3362	0.91
IG110[a]	26.375	0.3376	0.74
UcarC[a]	26.442	0.3368	0.84

[a]reported literature values of nuclear graphites (Fazluddin 2002)

Important to emphasize is that the XRD studies have shown that the graphitic composites made in this work were similar to other reported nuclear graphites in terms of their degree of graphitisation.

6.4. Raman analysis of the graphite composites

The Raman spectra of the raw graphite powders and the annealed graphite composites were collected on the filler phase spot (G) and binder phase spot (B) as shown in Figure 6.4. The Raman spectra collected on the filler phase spot (G) are shown in Figure 6.5. The spectra exhibit two distinct peaks. The disorder induced Defect ‘D’ band is located at approximately 1350 cm^{-1}

and the structural order induced Graphite 'G' band at approximately 1580 cm^{-1}. These two peaks are a result of vibrations of the sp^3 (C-C) and sp^2 (C=C) carbon atoms in the carbon material, respectively. The intensity ratio of the 'D' peak (I_D) to the 'G' peak (I_G) provides an indication of the degree of structural ordering in the carbon material. Pure crystalline graphite features a very low intensity D-peak and the intensity ratio is close to zero (Tuinstra and Koenig, 1970, Ko et al., 2001, Nakamizo et al., 1974b).

The neat resin was Raman inactive as it did not show any Raman peaks consistent with literature (Ko et al., 2001). The Raman Spectrum of the novolac phenolic carbonized to 1000 °C in nitrogen atmosphere is shown in Figure 6.6. It exhibited two peaks of almost equal intensities confirming its non-graphitic nature and that it is highly disordered. The estimated intensity ratios of the raw graphite powders, carbonised phenolic resin as well as annealed graphite composites are shown in Table 6.3. The intensity ratio of the NG, SG and carbonised resin obtained were 0.18, 0.12 and 0.9 (see Table 6.3); respectively.

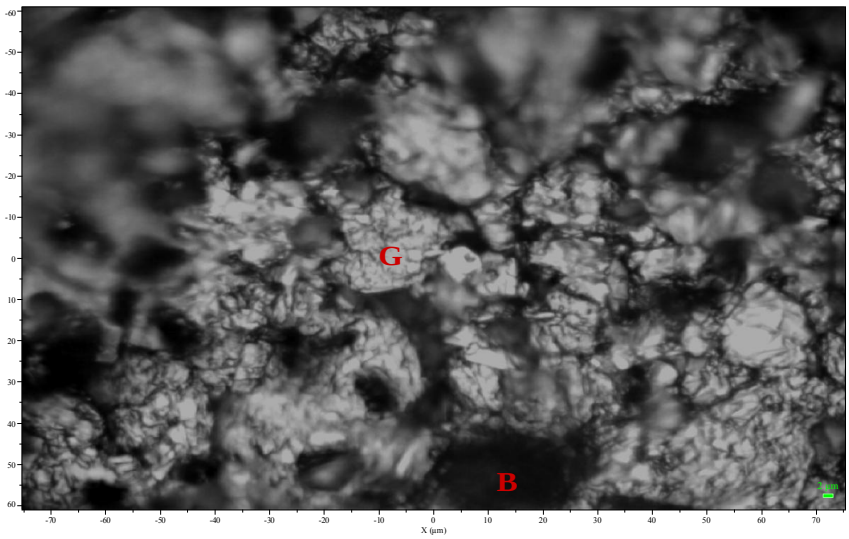

Figure 6.4: The micrograph of annealed graphite composite containing 64 wt.% NG (64:16:20) showing local spots under focus.

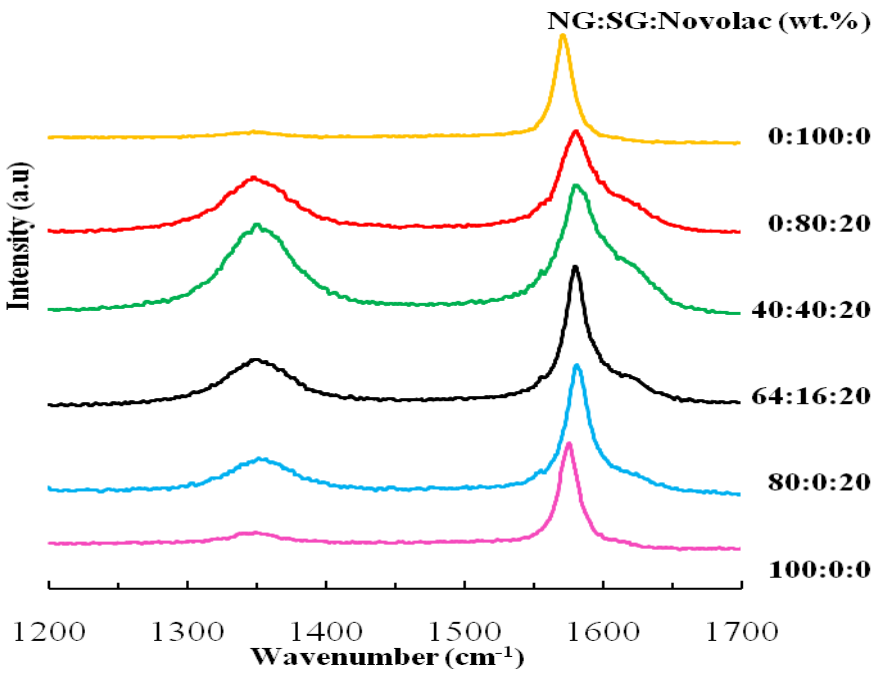

Figure 6.5: The Raman spectra of neat graphite powders and annealed carbon-graphite composites.

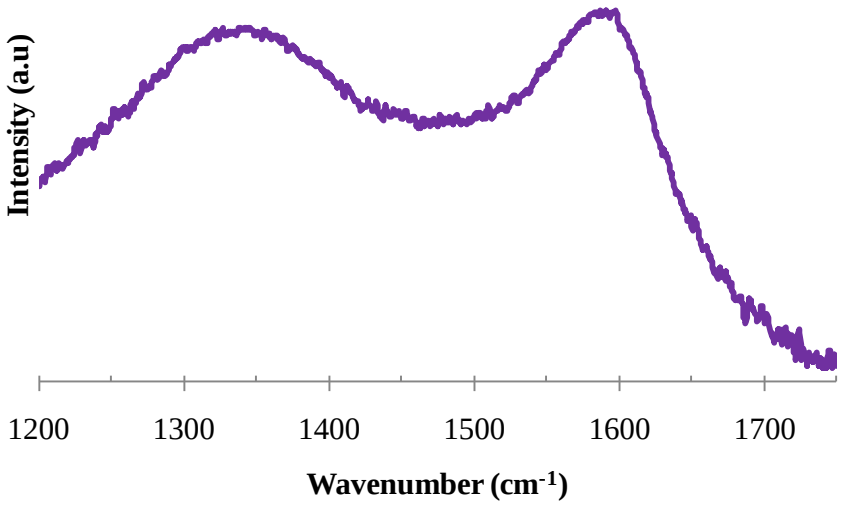

Figure 6.6: The Raman spectrum of the novolac phenolic resin carbonized to 1000 °C in nitrogen atmosphere.

Therefore the degree of structural ordering was in the order:

Carbonised resin < NG < SG.

The disorder in the NG could be due to the presence of impurities or the rhombohedral crystal forms. It has been observed in literature that disordered carbon materials have a broader and intense D-peaks relative to defective graphitic materials (Kudin et al., 2008). This was also observed in this work because the D-peak of the carbonised resin was broader than those of the raw graphite powders for example. The annealed graphite composites showed more intense and broad 'D' peaks than the raw graphite powders. This was due to the presence of the highly disordered residue from the resin binder and, to a less extent, to defects induced during the milling of the samples. The intensity ratio for the composite containing only SG and binder, (i.e. 80:0:20) is 0.59 while the one containing NG and binder, (i.e. 0:80:20), is 0.37. Thus the incorporation of the resin and milling resulted in more structural defects in the SG composite than in other composites. This is surprising as, according to the XRD and Raman results, the raw NG powder was less perfect than the synthetic one.

However these results suggest that annealing improved the perfection of the NG. Another observation is that the addition of the binder resin and subsequent annealing result in the shifting of the G-peak to a higher frequency especially for a composite containing no NG, i.e. 0:80:20 composite, which had shifted from ca. 1575 cm^{-1} to 1580 cm^{-1}. The Raman spectra were also collected on the binder phase (spot B in Figure 6.4). The Raman spectra are shown in Figure 6.7. The D-peaks of the spectra collected in the binder phase were broader and more intense than those observed in the filler phase; the G-peaks were also broad and less intense than those obtained for the filler phase.

Table 6.3: The relative intensity, I_D/I_G, of the raw graphites and annealed graphite composites.

Composition NG:SG:novolac (wt.%)	I_D (a.u)	I_G (a.u)	Relative intensity I_D/I_G
100:0:0	41.4	230.6	0.18
0:100:0	33.9	291.8	0.12
0:0:100	127.8	140.6	0.91
0:80:20	574.2	981.4	0.59
40:40:20	680.4	939.3	0.72
64:16:20	539.3	1363.2	0.40
80:0:20	490.7	1325.6	0.37

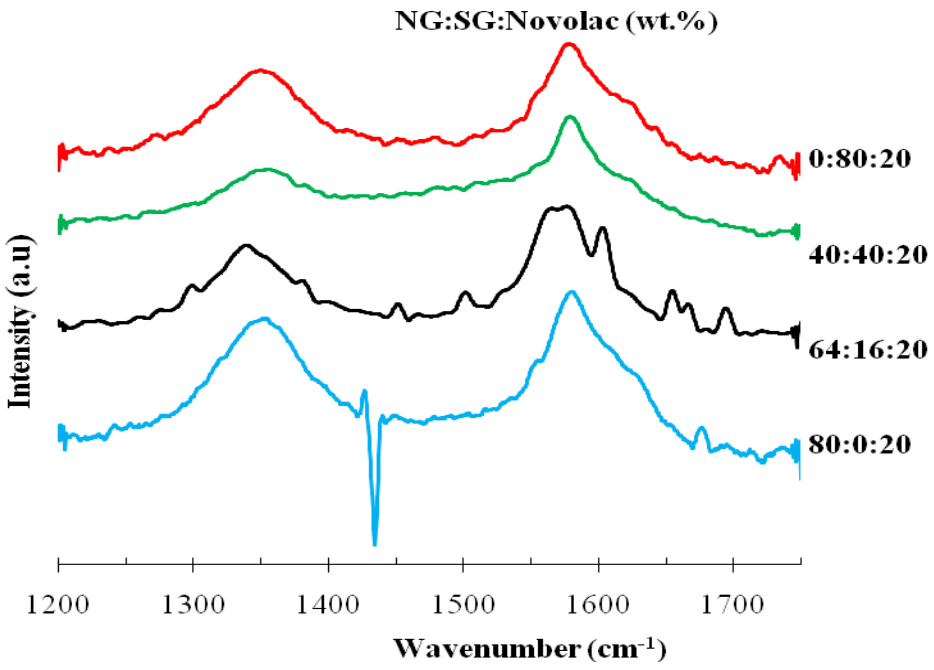

Figure 6.7: The Raman spectra of annealed graphite composites attained on the graphite binder phase (spot B in Figure 6.4).

Table 6.4: The relative intensity, I_D/I_G, of the annealed graphite composites attained on the binder phase (spot B in Figure 6.4).

Composition NG:SG:Novolac (wt.%)	**I_D (a.u)**	**I_G (a.u)**	**Relative intensity I_D/I_G**
0:80:20	177.8	257.8	0.69
40:40:20	280.2	596.0	0.47
64:16:20	237.9	413.5	0.58
80:0:20	222.6	325.5	0.68

This suggests that the binder phase had more disordered regions than the filler particles which was understandably due to the non-graphitic nature of the binder. The relative intensities of the D- to G-peaks for the spectra attained at the binder phase ranged from 0.47-0.69 (see Table 6.4) showing the high degree of disorder compared to the ones for the filler phase or particles.

6.5. Microstructure analysis of the graphite composites

The previous sections focused on the determination of the crystal structure of the annealed graphite composites as well as their degree of structural ordering. In this section we focus on the microstructural characteristics of the annealed graphite composites when they interact with different light conditions. Optical microscopy and scanning electron microscopy are the two principal techniques used to study these microstructural features.

6.5.1 Optical and scanning electron microscopy

It is well known that the interaction of polarised light with graphite lamellae produce different interference colours. The basal planes oriented perpendicular to the plane of polarization of the incident light appears purple when the retarder plate (1 λ tint) is inserted into the optical path. Whilst those oriented at an arbitrary angle to incident polarized light appear blue or yellow. The planes or grains that appear yellow and blue are aligned perpendicular to each other. The planes which are oriented at intermediate angles between planes appearing blue and yellow appear pink. This is not the case when viewed under reflected light (Edwards, 1989).

The reflected light, polarised light and scanning electron micrographs of the raw NG powder are shown in Figure 6.8(a), (b) and (c), respectively. The reflected light micrograph shows that the NG consists of flake-like particles (F) of different sizes with some pores (P) observed between and within the particles. Under the polarised light (see Figure 6.8(b)), the grains within the flakes showed different colors consistent with literature (Edwards, 1989) as mentioned above. The scanning electron micrograph of the NG shown in Figure 6.8(c) clearly shows the flake-like particles even though it was attained at higher magnification. The porosity (P) was more clearly visible in the SEM image of the NG consistent with OM observations. The microstructure of the SG powder is different from that of the NG powder. The reflected and polarised micrographs are shown in Figure 6.9(a) and (b), respectively; it consists of very thin needle-coke particles (NC) and some fine grained particles (FG). However the SEM image of the SG as shown in Figure 6.9(c) showed that the particles are more compact relative to the NG powder. Being optically non-textured, the raw and carbonized resin could not be examined using optical microscopy. The optical micrographs of moulded annealed graphite composites with various compositions are shown in Figure 6.10.

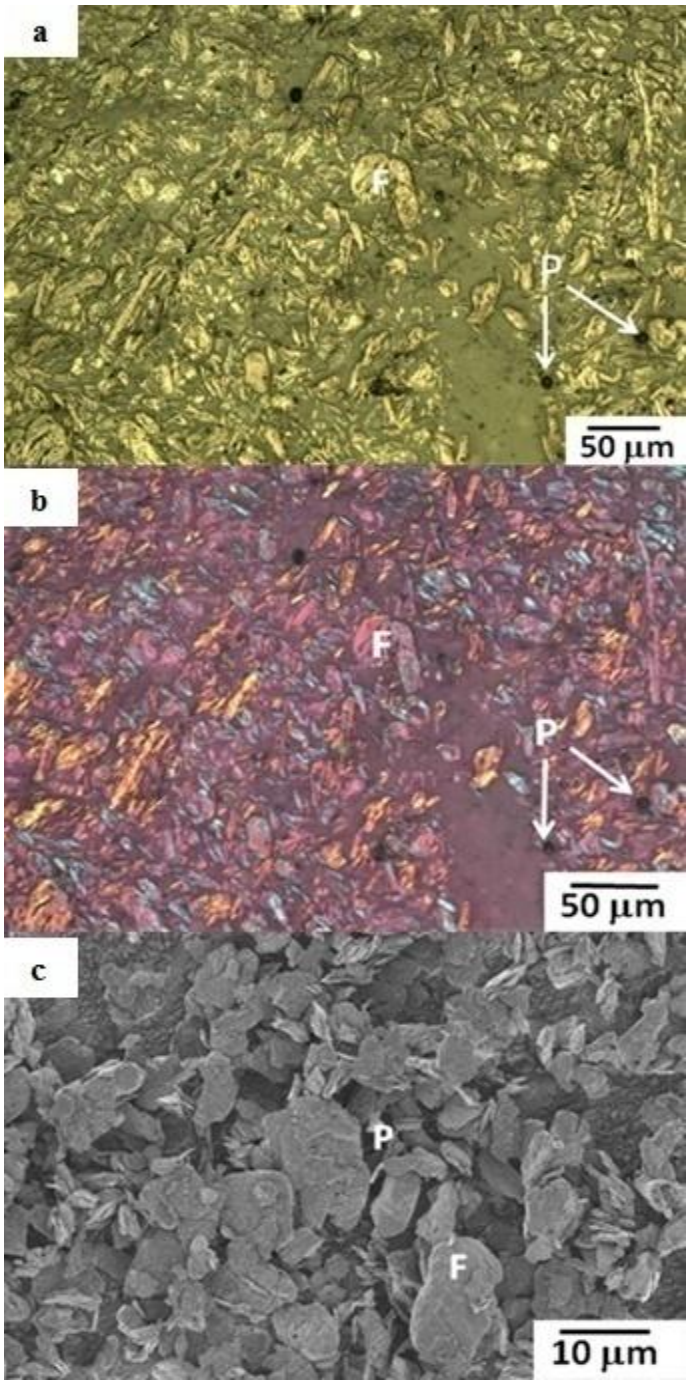

Figure 6.8: The micrographs of the NG under: (a) reflected light, (b). polarised light and (c) the SEM image.

The micrographs were taken in the direction perpendicular to pressing direction. The white thick arrow in the micrographs shows the pressing direction. Clearly the annealed graphitic composites showed very compacted particles relative to the raw graphite powders due to pressing and the binding effect of the resin. A composite containing only SG and binder, see Figure 6.10(a) and (b), showed a microstructure having compacted needle-coke particles (NC) and fine-grained mosaics inherent from the SG powder. Some porosity (P) and the resin carbon (R) were also seen. Under the polarised light (see Figure 6.10(b)), the resin carbon (R) appears blurry because it is optically non-textured and the pores appear black. The observed porosity resulted from volatilization of the phenolic resin during heat-treatment.

When viewed under the polarised light (with 1λ retarder plate or tint inserted in the optical path), see figure 6.10(b), different interference colours were observed as in the raw graphites showing different orientations of the filler particles within the grains. The optical micrographs of a composite containing equal amount of the graphite fillers are shown in Figure 6.10(c) and (d). The microstructure of this composite appeared more flake-like (F) and it is challenging to distinguish individual filler particles from the both graphites in this micrograph. Some particles showed to be cracked (C), these type of cracks could have arise from the processing of the graphites or from mechanical stresses applied on the graphite during compaction. The filler particles also showed different colours as observed for the composite having 0 wt.% NG (0:80:20). The composites containing mostly NG and binder, Figure 6.11, showed more compacted flake-like particles (F) and appear to be less porous than the other compositions although they were pressed at the same pressure for equal duration.

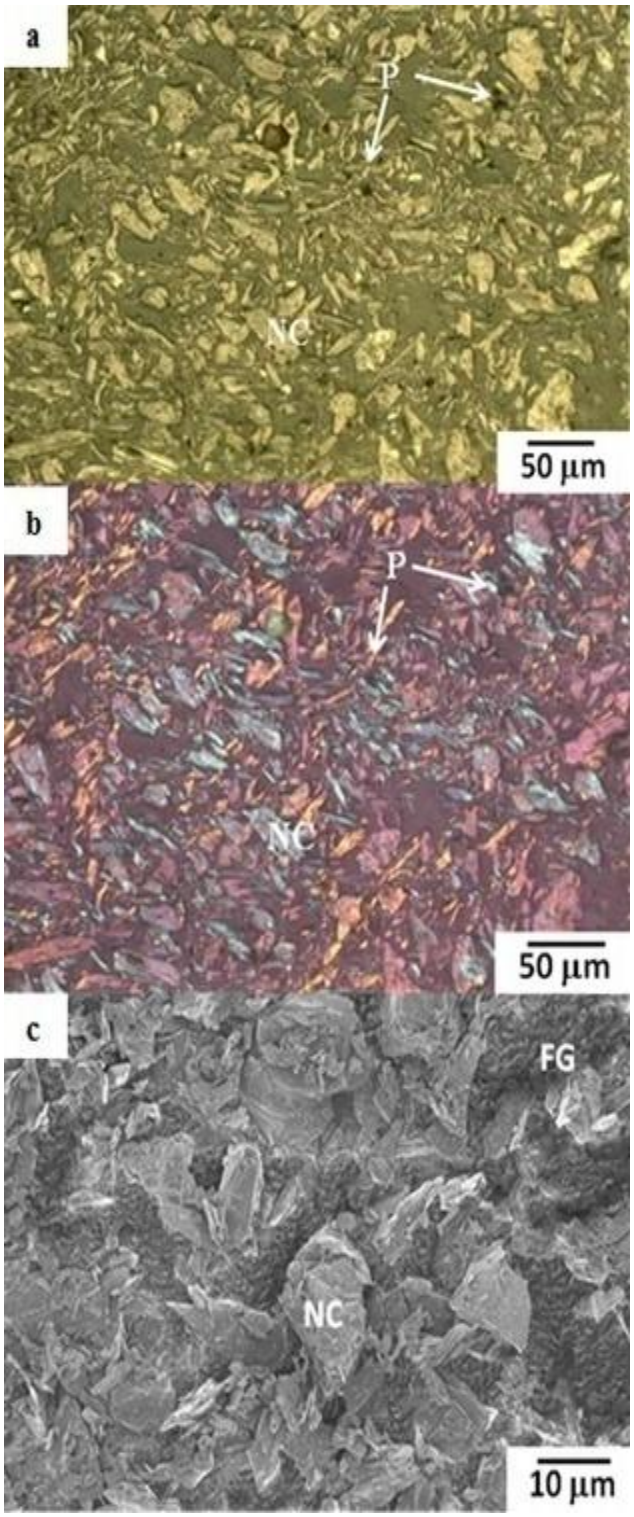

Figure 6.9: The micrographs of raw SG under: (a) reflected light, (b) polarised light and (c) SEM image.

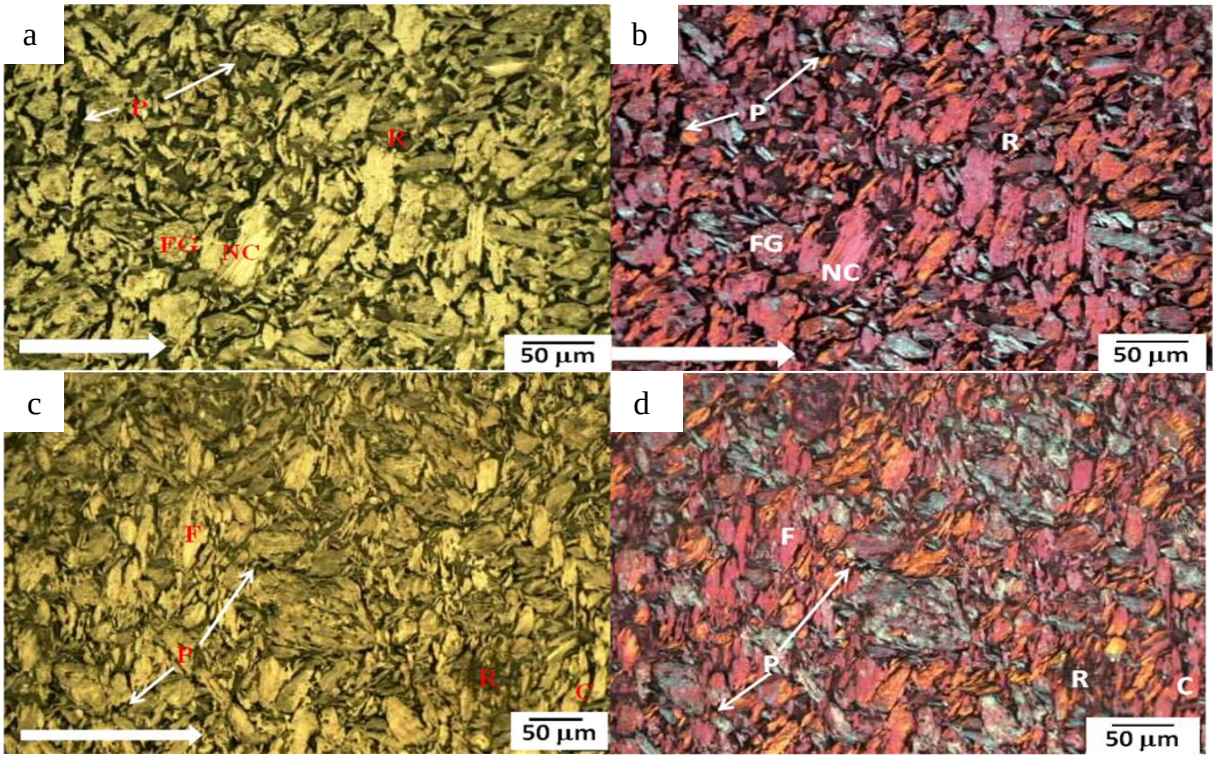

Figure 6.10: The optical micrographs of annealed graphite composites containing 0 wt.% NG (0:80:20) under: (a) reflected light and (b) polarised light. Micrographs for the composite containing 40 wt.% NG (40:40:20) under: (c) reflected light and (d) polarised light.

All the graphite particles in the annealed composites studied showed to be preferentially aligned perpendicular to the uniaxial pressing direction; an example is shown in Figure 6.12 wherein the graphite particles are shown at higher magnification. This type of particle alignment has also been observed in literature (Mariner and Sayir, 1999). However, the crystallites within the particles are oriented differently as shown by the different interference colours.

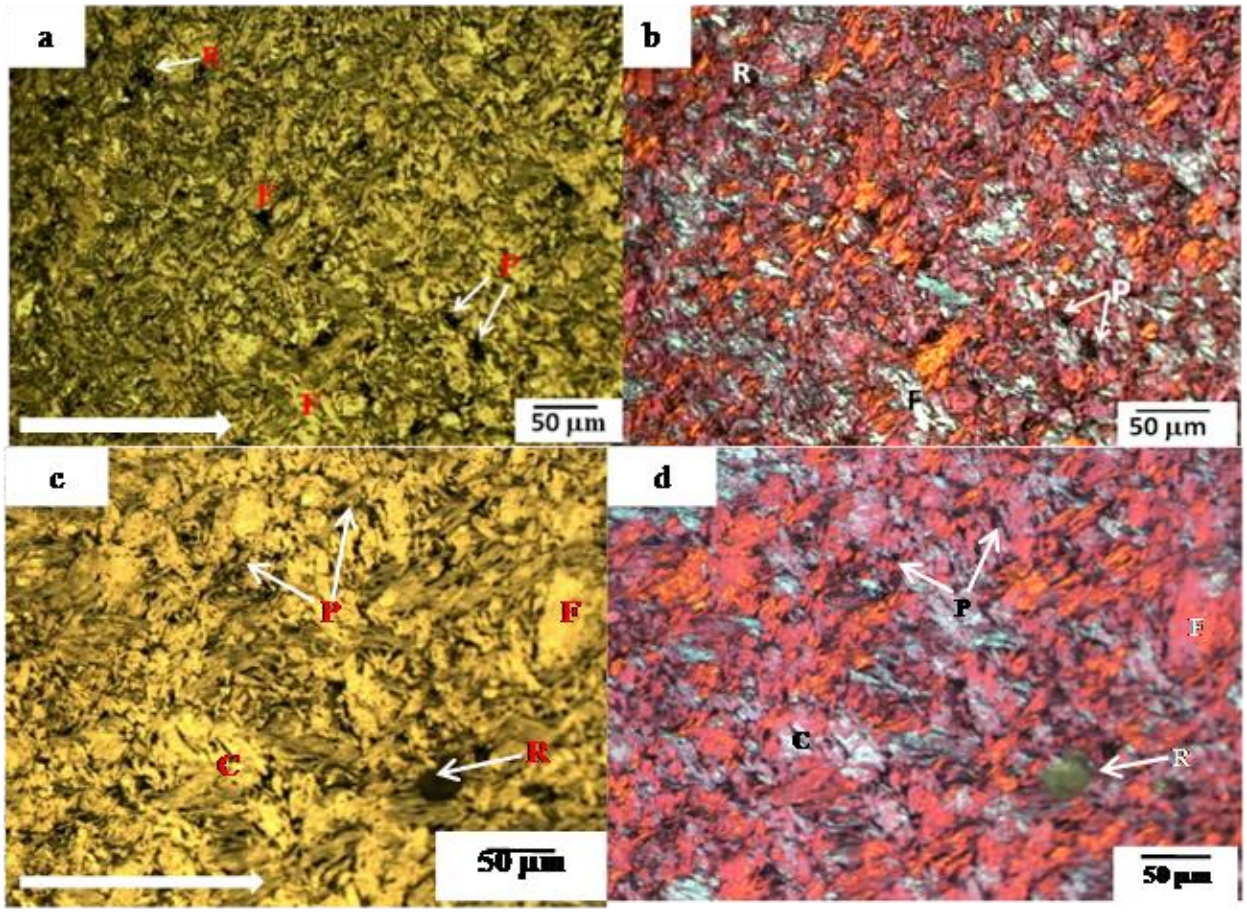

Figure 6.11: The optical micrographs of annealed graphite composites containing 64 wt.% NG (64:16:20) under: (a) reflected light and (b) polarised light. Micrographs for the composite containing 80 wt.% NG (80:0:20) under: (c) reflected light and (d) polarised light.

As the amount of the natural flake graphite filler increased (i.e. Figure 6.10 and 6.11), the flake-like particles (F) appeared more compacted. In all the composites studied, there was small porosity within some particles and not only between the particles as depicted on the micrographs. This was clearly seen under the reflected light. From this study it is clear that the annealed graphite composites clearly possess different microstructures, with more flake-like particles seen on the optical micrographs of composites containing mostly NG and the needle-like particles on optical micrographs containing mainly SG.

The morphologies of the annealed graphite composites were studied by SEM. The SEM micrographs of the annealed graphite composites are shown in Figure 6.13. All the composites showed similar morphologies; they showed compacted graphite filler particles with some voids between them. All composites had very smooth surfaces. The resin carbon (R) was also observed as black blurry spots on all the samples. A composite containing only SG and binder, Figure 6.13(a), appeared more porous than other composites consistent with OM observations.

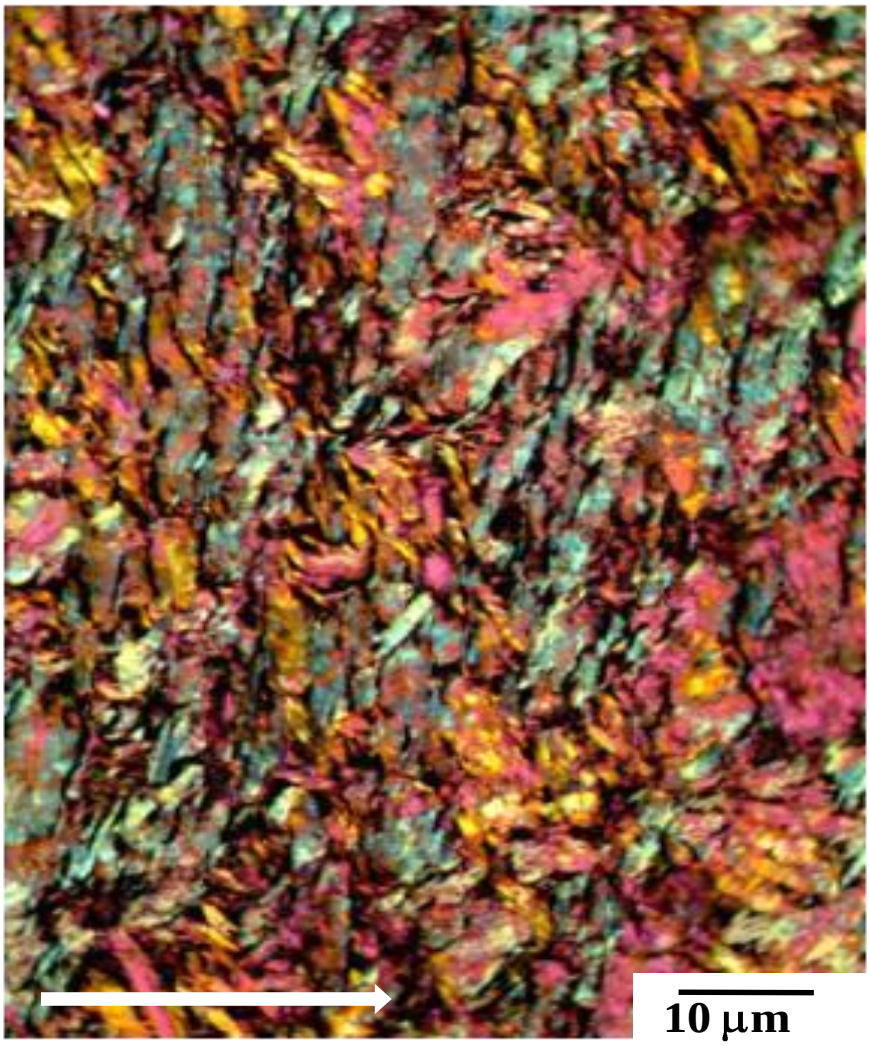

Figure 6.12: The optical micrograph of the annealed graphite composite (64:16:20) at high magnification showing preferred particle orientation.

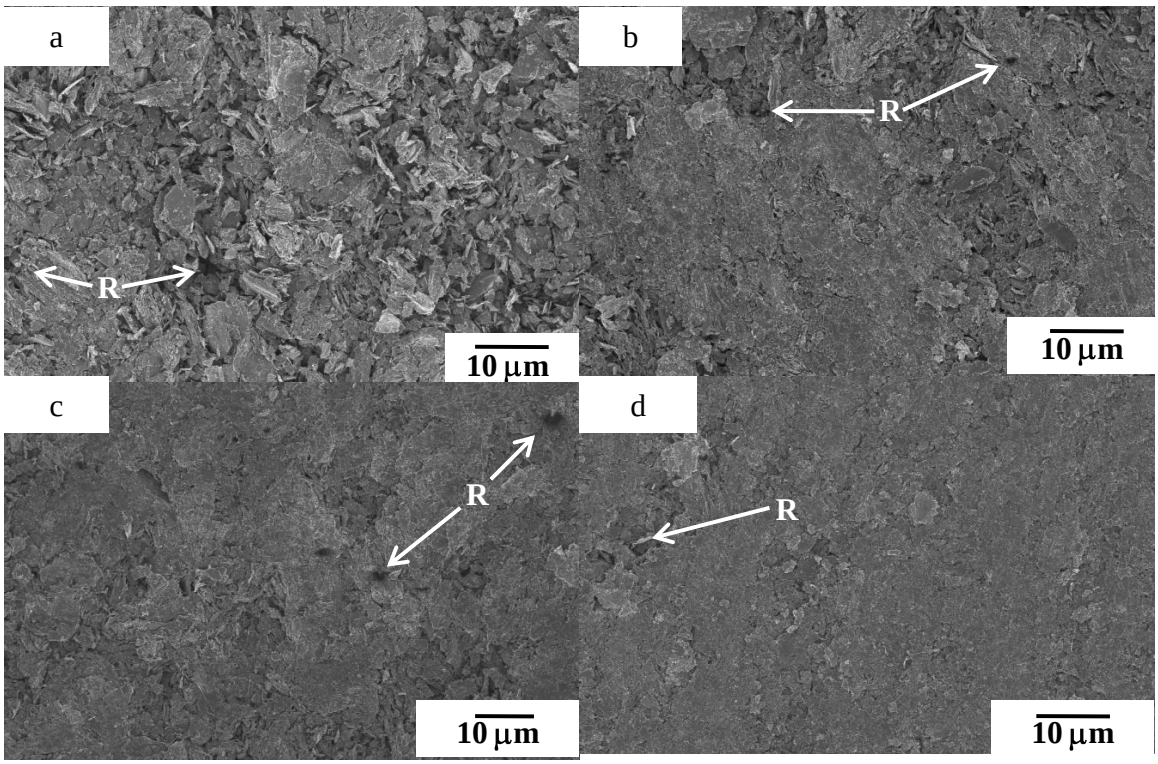

Figure 6.13: Scanning electron micrographs for annealed graphite composites containing: (a) 0 wt.% NG (0:80:20), (b) 40 wt.% NG (40:40:20) , (c) 64 wt.% NG (64:16:20) and (d) 80 wt.% NG (80:0:20).

6.6. Density measurements by Pycnometry

Characterization of annealed graphite composites using optical and scanning electron microscopy showed that these composites were porous. Porosity is a crucial feature or parameter which affects properties such as oxidative stability, thermal expansion, thermal conductivity and strength of the materials. The open porosity of the annealed graphite composites was measured and quantified using a pycnometer. The bulk and helium densities of the annealed graphite composites as well as graphite powders are presented in Table 6.5.

Table 6.5: The bulk and helium densities of the annealed graphite composites made in this work.

Composition (NG:SG:Novolac)	Sample ID no.	Bulk density ($g.cm^{-3}$)	Helium density ($g.cm^{-3}$)	Open porosity (%)
100:0:0	_	_	2.2529±0.0009	_
0:80:20	S1	1.2318±0.0024	2.1295±0.0005	
	S2	1.2406±0.0048	2.1296±0.0004	
	S3	1.2402±0.0016	2.1314±0.0008	
	Average	**1.2375±0.0029**	**2.1302±0.0005**	**41.9**
16:64:20	S1	1.5058±0.0034	2.0549±0.0008	
	S2	1.4948±0.0012	2.0546±0.0007	
	S3	1.5151±0.0001	2.0516±0.0009	
	Average	**1.5052±0.0015**	**2.0537±0.0008**	**26.7**
40:40:20	S1	1.4013±0.0027	2.0663±0.0005	
	S2	1.3743±0.0020	2.0671±0.0003	
	S3	1.3410±0.0037	2.0703±0.0006	
	Average	**1.3722±0.0028**	**2.0679±0.0004**	**33.6**
64:16:20	S1	1.4622±0.0032	2.0811±0.0006	
	S2	1.3987±0.0019	2.0858±0.0010	
	S3	1.4354±0.0075	2.1047±0.0011	
	Average	**1.4321±0.0042**	**2.0905±0.0009**	**31.5**
80:0:20	S1	1.5268±0.0026	2.0968±0.0008	
	S2	1.5316±0.0037	2.0918±0.0007	
	S3	1.4898±0.0050	2.0958±0.0011	
	Average	**1.5161±0.0038**	**2.0948±0.0008**	**27.6**
0:100:0	_	_	2.3070±0.0014	_
A3-3 (AVR)[a]	_	1.70	_	_
A3-3 (THTR & HTR-10)[a,b]	_	1.73	_	_
A3-27[a]	_	1.74	_	_

[a](Rind, 1981, Schulze et al., 1981, IAEA, June 2012) [b](Tang et al., 2008)

Triplicate measurements were performed per sample and three samples were measured per type or composition (therefore 9 measurements per composition). It is quite clear from this table that the pycnometers were very precise as shown by the lower standard deviations on the density values. The helium density of the SG and NG were 2.2529±0.0009 g.cm^{-3} and 2.3010±0.0014 g.cm^{-3}, respectively. The helium density value of the NG was peculiar; it was more than the theoretically accepted value of graphite (2.26 g.cm^{-3}). It is not known what causes this at present as at least 9 measurements were done and similar values were obtained. The average density results are better presented graphically as shown in Figure 6.14. The average bulk density increased as the NG content in the composites increased (from 1.2375 to 1.5161 g.cm^{-3}).

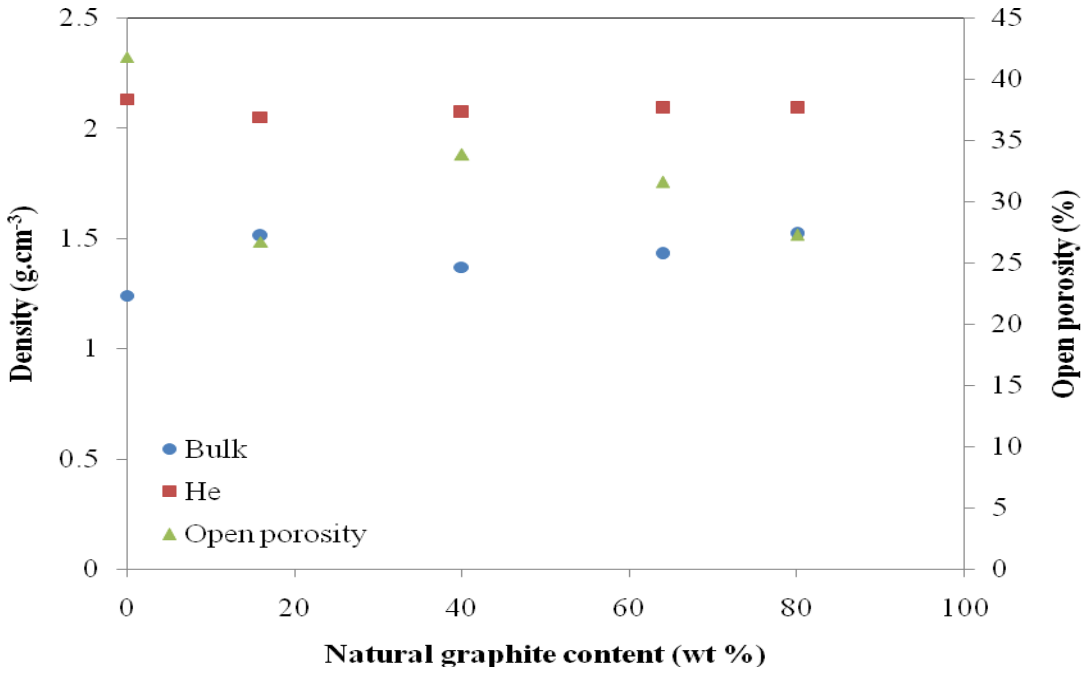

Figure 6.14: The bulk and helium densities vs. the NG content in the annealed graphite composites as well as open porosity calculated using equation (5.4).

The bulk density values of the graphite composites made in this work were lower than those of the graphite matrix composites (A3-3 and A3-27, i.e. 1.70-1.74 $g.cm^{-3}$) reported in literature (Rind, 1981) (Schulze et al., 1981) (IAEA, June 2012) (Tang et al., 2008). This is due to mainly low pressure used during cold compression molding of the composites used in this work, in fact the pressure used (13 MPa) is less than the pre-molding pressure (30 MPa) of the matric composites used in literature. Factors such as the mixing, carbonisation temperature, annealing temperature, holding time and the method used to measure bulk density also have the effect on bulk density. The helium density (a measure of skeletal densities excluding closed pores) values of the composites were constant; the values agreed with each other to within 1.6 %. The helium densities of the composites were expectedly lower than those of the raw graphite powders due to the presence of the non-graphitising resin carbon. The open porosity, calculated using equation (5.2), decreased with the increase in the NG content in the composite. This is consistent with the microstructural observation that the composite containing no NG (0:80:20) appeared more porous (see Figures 6.10(a) and 6.13(a)). The decrease in open porosity as the NG increased could be attributed to the malleability of the NG flakes particles. During the pressing they deform more readily to form dense structures. The average open porosity in the composites is approximately 28%.

This characterisation study showed that the annealed graphite composites were polycrystalline materials having hexagonal crystal structure. Microstructurally, the graphite composites containing mainly NG possessed flake-like particles while those containing mainly SG possessed needle-like particles. These particles were aligned in the direction perpendicular to uniaxial compression direction. The composite containing only SG and binder was the most porous (41 %) of the materials.

References

BACON, G. E. (1950) *Acta Crystallographica,* 3**,** 320.

BISCOE, J. & WARREN, B. E. (1942) *Journal of Applied Physics,* 13**,** 364-371.

BROOKS, J. D. & TAYLOR, G. H. (1965) The formation of graphitising carbons from the liquid phase. *Carbon,* 3**,** 185.

CLARK, L. M. & TAYLOR, R. E. (1975) Radiation loss in the flash method for thermal diffusivity. *Journal of Applied Physics***,** 714-719.

COHN, J. G., STERN, E. W. & ETRIS, S. F. (2005) Graphite, Artificial IN KIRK-OTHMER (Ed.) *Kirk-Othmer Encyclopedia of Chemical Technology.* 5 ed., John Wiley & Sons.

CUNNINGHAM, N., LEFEVRE, M., DODELET, J.-P., THOMAS, Y. & PELLETIER, S. (2005) Structural and mechanical characterization of as-compacted powder mixtures of graphite and phenolic resin. *Carbon,* 43**,** 3054-3066.

DUBOIS, J., AGACHE, C. & WHITE, J. L. (1997) The carbonaceous mesophase formed in the pyrolysis of graphitisable organic materials. *Material characterisation,* 39**,** 105-119.

EDWARDS, I. A. S. (1989) Structure in Carbons and Carbon Forms. IN MARSH, H. (Ed.) *Introduction to Carbon Science.* London, Butterworths.

FAZLUDDIN, S. (2002) Crack Growth Resistance in Nuclear Graphite *Department of Materials, School of Process, Materials Engineering.* Leeds, The University of Leeds.

FISCHBACH, D. B. (1971) IN PHILIP L WALKER, J. (Ed.) *Chemistry and Physics of Carbon.* New York, Marcel Dekker, INC. .

FITZER, E., KOCHLING, K. H., BOEHM, H. P. & MARSH, H. (1995) Recommended terminology for the description of carbon as a solid. *Pure and Applied Chemistry,* 67**,** 473-506.

FRANKLIN, R. E. (1951a) *Acta Crystallographica,* 4**,** 253-261.

FRANKLIN, R. E. (1951b) *Proceedings of the Royal Society,* 209**,** 196-218.

HACKER, P. J., NEIGHBOUR, G. B. & MCENANEY, B. (2000) The coefficient of thermal expansion of nuclear graphite with increasing thermal oxidation. *Journal of Physics D: Applied Physics,* 33**,** 991-998.

HOERNI, J. (1949) *Nature,* 164**,** 1045.

HOINKIS, E. & ROBENS, E. (1989) Surface area and porosity of unmodified graphitic matrices A3-27 and A3-3 (1950) and oxidized matrix A3-3 (1950). *Carbon,* 27**,** 157-168.

HOUSKA, C. R. & WARREN, B. E. (1954) *Journal of Applied Physics,* 25**,** 1503.

HU, R. & CHUNG, T. C. (1996) *Carbon,* 43**,** 1181-1190.

HULL, A. W. (1917) *Physical review,* 10**,** 661.

IAEA (June 2012) Advances in High Temperature Gas Cooled Reactor Fuel Technology. Vienna, International Atomic Energy Agency.

JAGODZINSKI, H. (1949) *Acta Crystallographica,* 2**,** 298.

KELLY, B. T. (1981) *Physics of Graphite,* London and New Jersey, Applied Science Publishers.

KIPLING, J. J., SHERWOOD, J. N., SHOOTER, P. V. & THOMPSON, N. R. (1964) Factors influencing the graphitization of polymer carbons. *Carbon,* 1**,** 315-320.

KIPLING, J. J. & SHOOTER, P. V. (1966) Factors affecting the graphitisation of carbon: Evidence from polarised light microscopy. *Carbon,* 4**,** 1-4.

KIRK-OTHMER (2005) Graphite, Artificial. *Encyclopaedia of Chemical Technology*.

KNOP, A. & PILATO, L. A. (1985) *Phenolic Resins: Chemistry, applications and performance.* Berlin, Heidelberg, New York, Tokyo, Springler-Verlag.

KO, T.-H., KUO, W.-S. & CHANG, Y.-H. (2001) Microstructural Changes of phenolic resin during pyrolysis. *Journal of Applied Polymer Science,* 81**,** 1084-1089.

KUDIN, N. K., OZBAS, B., SCHNIEPP, H. C., PRUD'HOMME, R. K., AKSAY, I. A. & FERRARI, R. (2008) Raman Spectra of Graphite Oxide and Functionalized Graphene Sheets. *Nano Letters,* 8**,** 36-41.

LAIDLER, D. & TAYLOR, A. (1940) *Nature,* 141**,** 130.

LEWIS, R. T. (1971) 12th biennial conference on carbon. Pittsburg, American Carbon Society.

LIPSON, H. & STOKES, A. R. (1942a) *Procedings of the Physics Society of London,* A181**,** 101.

LIPSON, H. & STOKES, A. R. (1942b) *Proceedings of the Physics Society of London.,* A181**,** 101.

MARINER, J. T. & SAYIR, H. (1999) High thermal conductivity composite and method. IN PATENT, U. S. (Ed.). United States of America, Advanced Ceramics Corporation, Lakewood, Ohio.

MARSH, H., MARTINEZ-ESCANDELL, M. & RODRIGUEZ-REINOSO, F. (1999) Semocokes from pitch pyrolysis: Mechanisms and kinetics. *Carbon,* 37**,** 363-390.

MARSH, H. & WARBURTON, A. P. (1970) Catalysis of graphitisation. *Journal of Applied Chemistry,* 20**,** 133-142.

MICROMERITICS (2009) Micromeritics Accupyc II 1340 Pycnometer. www.youtube.com.

MURTY, H. N., BIEDERMAN, D. L. & HEINTZ, E. A. (1977) Apparent catalysis of graphitisation. 3. Effect of boron *Fuel,* 56**,** 305-312.

NAKAMIZO, M., KAMMERECK, R. & P.L. WALKER, J. (1974) Laser Raman studies on carbons. *Carbon,* 12**,** 259-267.

NICHOLLS, D. R. (2001) The Pebble Bed Modular Reactor. *Transactions of the Royal Society of South Africa,* 56**,** 125-130.

NICHOLLS, D. R. (2002) The Pebble Bed Modular Reactor. *South African Journal of Science,* 98**,** 31-35.

NIGHTINGALE, R. E. (1962) *Nuclear graphite,* London, Academic press.

PARTHASARAY, G., SREEDHAR, B. & CHETTY, T. R. K. (2006) Spectroscopic and X-ray diffraction studies on fluid deposited rhombohedral graphite from the Eastern Ghats mobile belt, India. *Current Science,* 90**,** 995-1000.

RIND, W. (1981) Transport of fission products in matrix and graphite. IN HOINKIS, E. (Ed.) *Proceedings of a coloquim held at the Hahn-Meitner-Institut* Berlin, Germany, Hahn-Meitner-Institut fur kernforschung Berlin Gmbh.

RULAND, W. (1965) X-ray studies on the structure of graphitic carbons. *Acta Crystallographica,* 18**,** 992-996.

SCHULZE, R. E., SCHULZE, H. A. & RIND, W. (1981) Report of the Keruforschungslage Julich, Graphic Matrix Materials for Spherical HTR Fuel Elements.

SPRENGLING, G. R. & FREEMAN, J. H. (1950) The reaction of phenol with formaldehyde. *Journal of American Chemical Society,* 72**,** 1982-1985.

TANG, C., FU, X., ZHU, J., ZHAO, H. & TANG, Y. (2012) Comparison of two irradiation testing results of HTR-10 fuel spheres. *Nuclear Engineering and Design,* 251**,** 453-458.

TANG, C., LI, Z., ZHOU, Y. & FU, X. (2008) Irradiation testing of matrix material for spherical HTR-10 fuel elements. *Nuclear Engineering and Design,* 238**,** 2886-2892

TANG, C. H., TANG, Y., ZHU, J. G., ZOU, Y. W., LI, J. O. & NI, X. O. (2002) Design and manufacture of the fuel element for 10 MW high temperature gas-cooled reactor. *Nuclear Engineering and Design,* 218**,** 91-102.

TRUCANO, P. & CHEN, R. (1975) *Nature,* 258**,** 136.

TUINSTRA, F. & KOENIG, J. L. (1970) Raman spectrum of graphite. *Journal of Chemical Physics,* 53**,** 1126-1130.

WARREN, B. E. & GRINGRIICH, N. S. (1934) *Physical Review,* 46**,** 368-399.

WEBB, P. A. (2001) Volume and Density Determinations for Particle Technologists. Micromeritics Intruments Corporation.

ZHAO, H. S., LIANG, T. X., ZHANG, J., HE, J., ZOU, Y. W. & TANG, C. H. (2006) Manufacture and characteristics of spherical fuel elements for the HTR-10. *Nuclear Engineering and Design,* 236**,** 643-647.

CHAPTER 7: RESULTS AND DISCUSSION-PROPERTIES

Introduction

In the previous chapter, a report and discussion on how the model graphite composites were made, their microstructure, particles orientation and porosity characterized were elucidated. The focus in this chapter was on the properties of these composites and discusses the effect of changing the ratio of the graphite powders in the composite on properties. It is also shown how cold uniaxial pressing result in anisotropy in properties in the fabricated composites. The properties of interest were air oxidative stability, thermal expansion, thermal conductivity, bending strength and modulus.

7.1 Thermogravimetric analysis (TGA)

The non-isothermal air oxidative stability of the raw materials (i.e. NG, SG and novolac phenolic resin) in air, as well as that of the annealed graphite composites, was studied by thermogravimetric analysis. The TGA profiles of the natural graphite, synthetic graphite and novolac phenolic resin are shown in Figure 7.1. The onset (T_i) and endset (T_e) air oxidation temperature were determined using intersection of the segments before and after inflection points (Brown, 2001). The temperature at which the sample loses maximum weight was denoted T_m. The neat phenolic resin had a lower stability than the other raw materials. It started to lose mass at a T_i value of approximately 120 °C due to the loss of moisture, followed by loss of volatiles in the temperature range 340-510 °C.

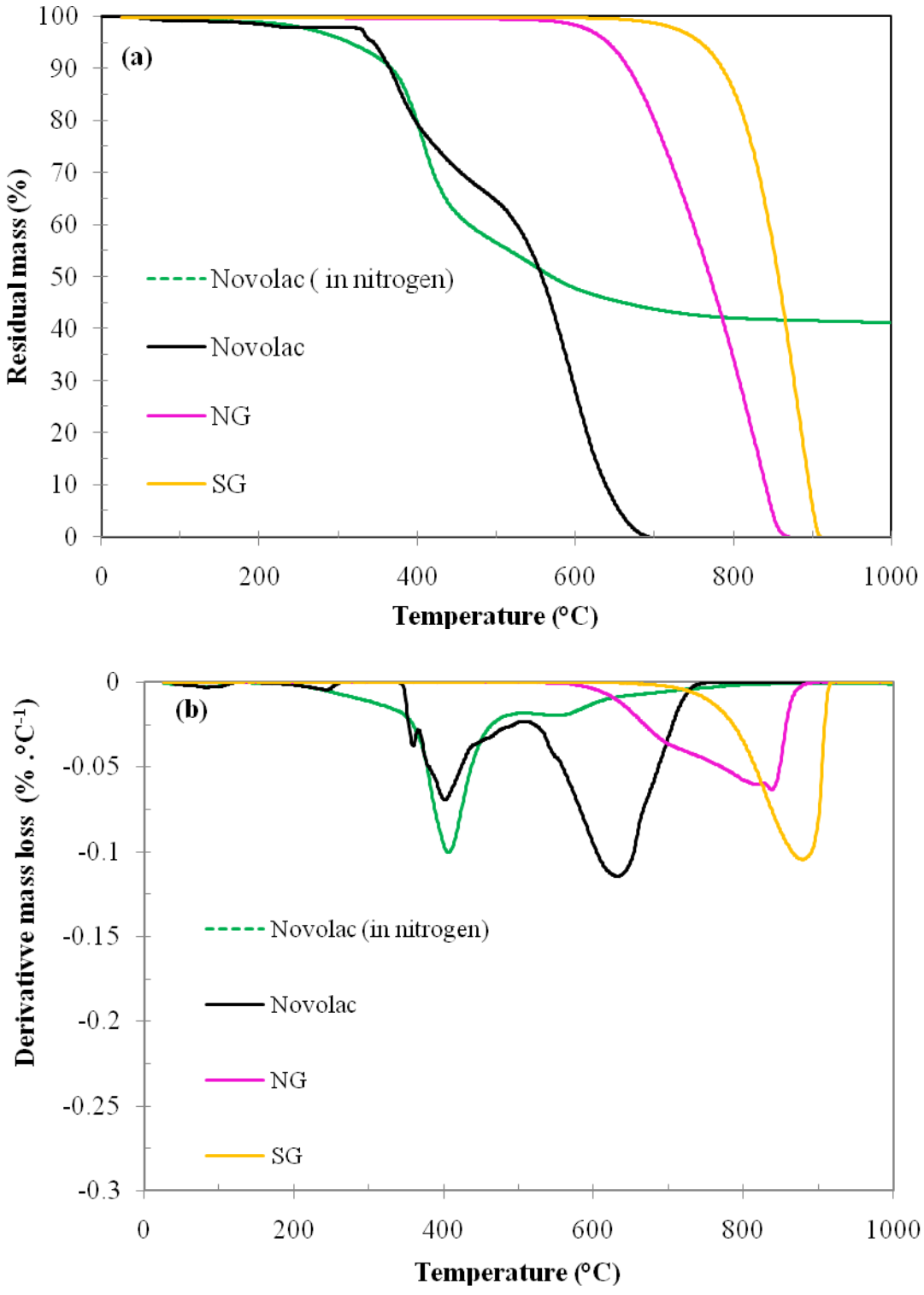

Figure 7.1: (a) TGA profiles of the novolac phenolic resin, NG and SG heated at 5 °C/min in air. (b) The derivative mass loss curves for materials in (a).

The loss of carbonaceous matter was observed above 510 °C and the endset air oxidation was reached at a T_e of about 700 °C. The weight losses associated with moisture, volatiles and resin carbon oxidation were 0.89 %, 31.4 % and 67.2 %, respectively. The phenolic resin had an ash content of 0.5 %. The derivative mass loss curve of the phenolic resin heated in air (see Figure 7.1 (b)) revealed that the mass loss occurred in 5 steps. The maximum mass loss rate was observed at about 631 °C. The profile of the phenolic resin heated in nitrogen (see Figure 7.1(a)) has shown that it contains 41 % carbon. The NG was less reactive than the novolac phenolic resin as it started to oxidise at higher temperatures, i.e. about 600 °C. The endset oxidation temperature (T_e) of the NG was about 860 °C. The TG profile of the SG showed that it was most stable against oxidation with a T_i value of about 750 °C and the T_e of about 900 °C. The graphite powders contained negligible ash. The lower onset temperature of the neat NG can be attributed to the presence of catalytic impurities such as Fe and Na in the sample (Badenhorst et al., 2010) and having more reactive edge sites. The heat-treatment at 1800 °C is expected to partially deactivate these impurities. In addition, the raw NG had structural defects (rhombohedral crystalline phase as evidenced by XRD) which made them more susceptible to oxidation. These observations are consistent with reports in literature (Welham and Williams, 1998) that air oxidation of carbonaceous materials depend on parameters such as crystal structure and surface area. The bimodal response in the DTG curves (see Figure 7.1(b)) indicated that the oxidation of NG proceeded in two overlapping steps. It is expected that the defective sites in the NG would oxidise first, followed by carbon atoms in the graphite hexagonal lattice. In contrast, the oxidation of the SG was a single-step reaction. The SEM image of the NG in Figure 6.8(c) showed the sample to be more porous than that of the synthetic graphite, see Figure 6.9(c), this could also be one of the reasons why the NG was more reactive in air. The air oxidative stability

of the SG could also be related to how it was made especially if it was somewhat purified. Another important point is that the NG had a mean particle size of 30.6 μm while that of the synthetic graphite was about 48.8 μm, this also contributed to lower reactivity in air for the SG.

It is well known that the larger the average particle size, the more resistant to air oxidation the graphitic material becomes (Jiang et al., 2000, Honda et al., 1972). The TGA profiles of the annealed graphite composites are shown in Figure 7.2. These composites showed pronounced air oxidation stability with an onset temperature (T_i) at approximately 650 °C. The endset oxidation temperature (T_e) of these composites was approximately 940 °C. However the composite containing only SG and binder (0:80:20) showed slightly higher onset and endset air oxidation temperatures, i.e. about 670 and 980 °C, respectively. The lower reactivity of the annealed composites in air is attributed to the heat-treatment which annealed some structural defects and deactivated catalytic impurities especially in the composites containing mainly NG as a major component (i.e. 64:16:20 and 80:0:20 composites). These composites were observed to be oxidatively less stable than the other composites (i.e. 0:80:20 and 40:40:20 composites) but the difference was approximately 50 °C. The mass loss rate curves for the annealed samples appeared bimodal as shown in Figure 7.2(b). The first step around 700 °C was due to the loss of resin-derived carbon which oxidizes first, followed by loss of graphitic carbon around 850 °C. The loss of resin-derived carbon appeared to wane with increasing NG content. The reason for this is not understood at this point. These graphitic composites were oxidatively stable below 650 °C and therefore in the absence of air and thermal gradients, they should be able to withstand high temperature nuclear reactor conditions where they could be applied or used as moderator or reflector.

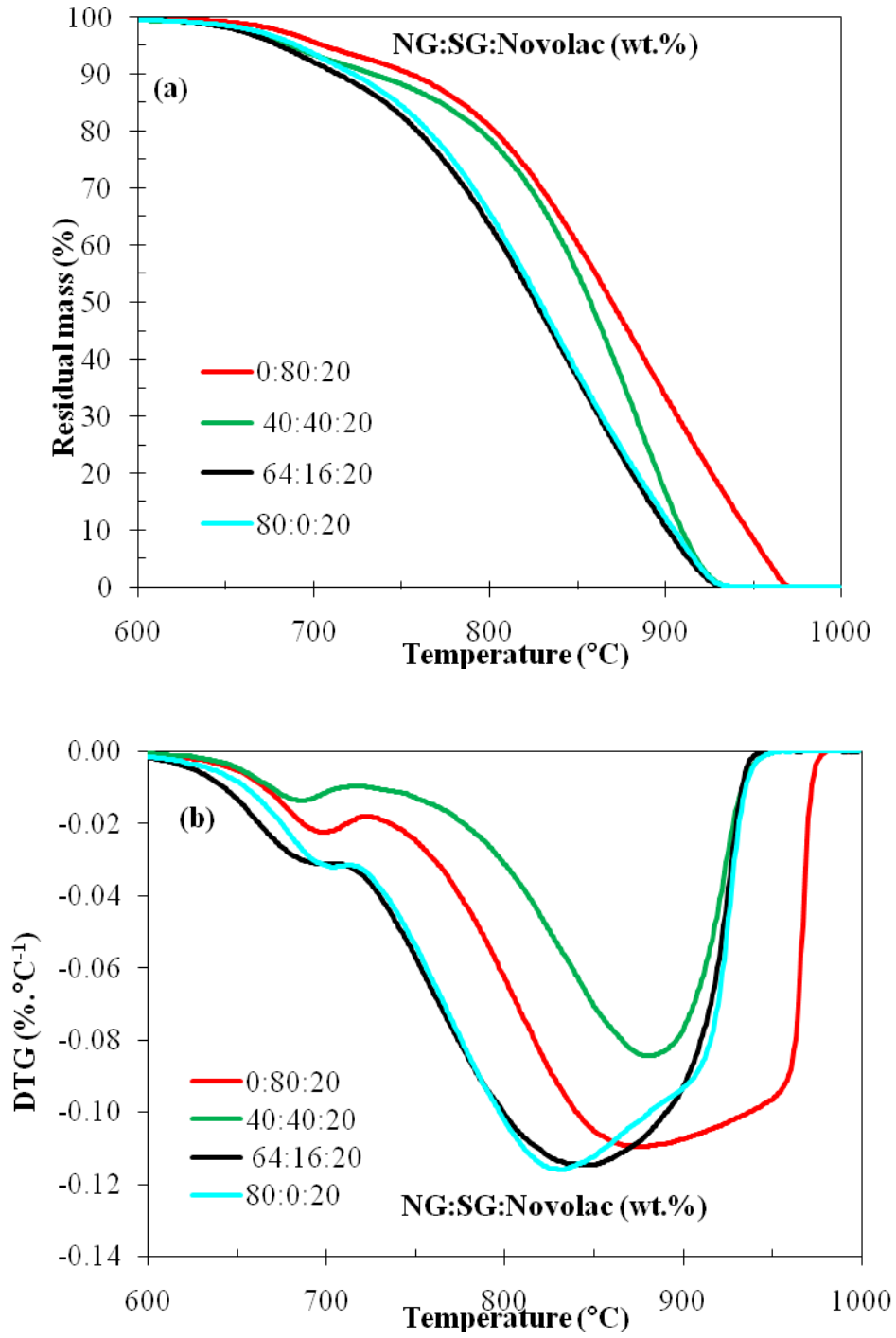

Figure 7.2: (a) The TGA profiles of the annealed graphite composites heat-treated to 1800 °C (in a helium atmosphere) at 5 °C/min and soaked for 2 hours. (b) the derivative mass loss curves for materials in (a).

7.2 Thermomechanical analysis (TMA)

The expansion behaviour of the annealed graphite composites was studied using thermomechanical analysis. The linear expansion coefficients (CTE) measured in the direction parallel to compression moulding direction were denoted, α_P whilst those measured in the direction normal to compression moulding direction were denoted, α_N (N.B. the direction parallel to compression moulding is from top to bottom of the disc surface shown in Figure 5.2 while the direction normal to compression moulding direction is from side to side of the disc). The length change and CTE, α_P as a function of temperature for the composite containing only synthetic graphite and binder (0:80:20) is shown in Figure 7.3. The expansion behaviour of the annealed graphite composite as shown in Figure 7.3 (a) was linear throughout the temperature range studied (20-600 °C). The maximum length change in the direction parallel to pressing was approximately 38 µm for this composite. The instantaneous CTE value at a particular temperature is defined as a slope of the tangent of the length change vs. temperature curve at that particular temperature. On the other hand, the mean or average CTE is defined as a slope of the chord between two points in the length change vs. temperature curve. The instantaneous CTE, α_P (20-600 °C) values, calculated using equation (5.3), are shown in Figure 7.3(b) and were in the range (2.4-11.2) $\times 10^{-6}$ K^{-1} for this composition. The average CTE, α_P for the three runs performed in this temperature range was (6.25±0.89) $\times 10^{-6}$ K^{-1} as shown in Table 7.1.

A composite containing 16 wt.% NG (i.e. 16:64:20) showed expansion behaviour similar to the synthetic graphite-binder composite; the maximum length change in the pressing direction for this composition was approximately 37 µm (see Figure 7.4(a)). The instantaneous α_P (20-600 °C) values were in the range (1.7-9.1) $\times 10^{-6}$ K^{-1}. The average α_P (20-600 °C) value for this composite

was (5.70±0.80) $\times 10^{-6}$ K^{-1}. A composite containing equal amount of the filler graphites, i.e. 40:40:20, was no different in expansion behaviour as shown in Figure 7.5 (a).

Table 7.1: Average linear coefficients of thermal expansion of the annealed graphite composites obtained in the temperature range 20 to 600 °C and their anisotropic ratios.

Composition (NG:SG:Novolac) wt.%	Open porosity (%)	Length change, ΔL_p (µm)	Length change, ΔL_N (µm)	CTE, α_P ($\times 10^{-6}$) (K^{-1})	CTE, α_N ($\times 10^{-6}$) (K^{-1})	α_P:α_N
0:80:20	41.9	38	13	6.25±0.89	2.06±0.50	3.0
16:64:20	26.7	37	10	5.70±0.80	1.74±0.31	3.3
40:40:20	33.6	34	12.5	5.82±0.75	2.08±0.44	2.8
64:16:20	31.5	51	15	7.88±1.40	2.00±0.17	3.9
80:0:20	27.6	45	15	6.58±0.71	1.91±0.45	3.4
A3-3 (AVR)[a]		-	-	2.80	2.92	1.0
A3-3(THTR)[a]		-	-	2.89	3.45	0.8
A3-3 (HTR-10)[b]		-	-	2.72	2.99	0.9
A3-27(AVR)[a]		-	-	2.43	2.69	0.9

[a](Rind, 1981, Schulze et al., 1981, IAEA, June 2012) [b](Tang et al., 2008)

The maximum length change on heat-treatment to 600 °C was approximately 34 µm. The instantaneous α_P values obtained, as shown in Figure 7.5 (b), were in the range (1.7-10.2) $\times 10^{-6}$ K^{-1} in the temperature range 20-600 °C. The average α_P value for this composite was (5.82±0.75) $\times 10^{-6}$ K^{-1}. The average α_P values for the composites containing 0 wt.% NG, 16 wt.% NG and 40 wt.% NG were very close or similar.

On the other hand, composites containing mainly natural graphite, i.e. 64:16:20 and 80:0:20, as shown in Figure 7.6 and 7.7, respectively, showed maximum length change of approximately 51 and 45 µm, respectively. The instantaneous α_P values ranged from (4.3-15.7) $\times 10^{-6}$ K^{-1} for the 64:16:20 composite. The average α_P value was (7.88±1.40) $\times 10^{-6}$ K^{-1}. The α_P values for a composite containing only natural graphite and binder (i.e. 80:0:20) ranged from (1.5-8.5) $\times 10^{-}$

$^{6}K^{-1}$. The average α_P value for this composite was (6.58±0.71) $\times 10^{-6}$ K^{-1}. All the annealed graphite composites expanded linearly and uniformly in the temperature range 20-600 °C in the compression moulding direction.

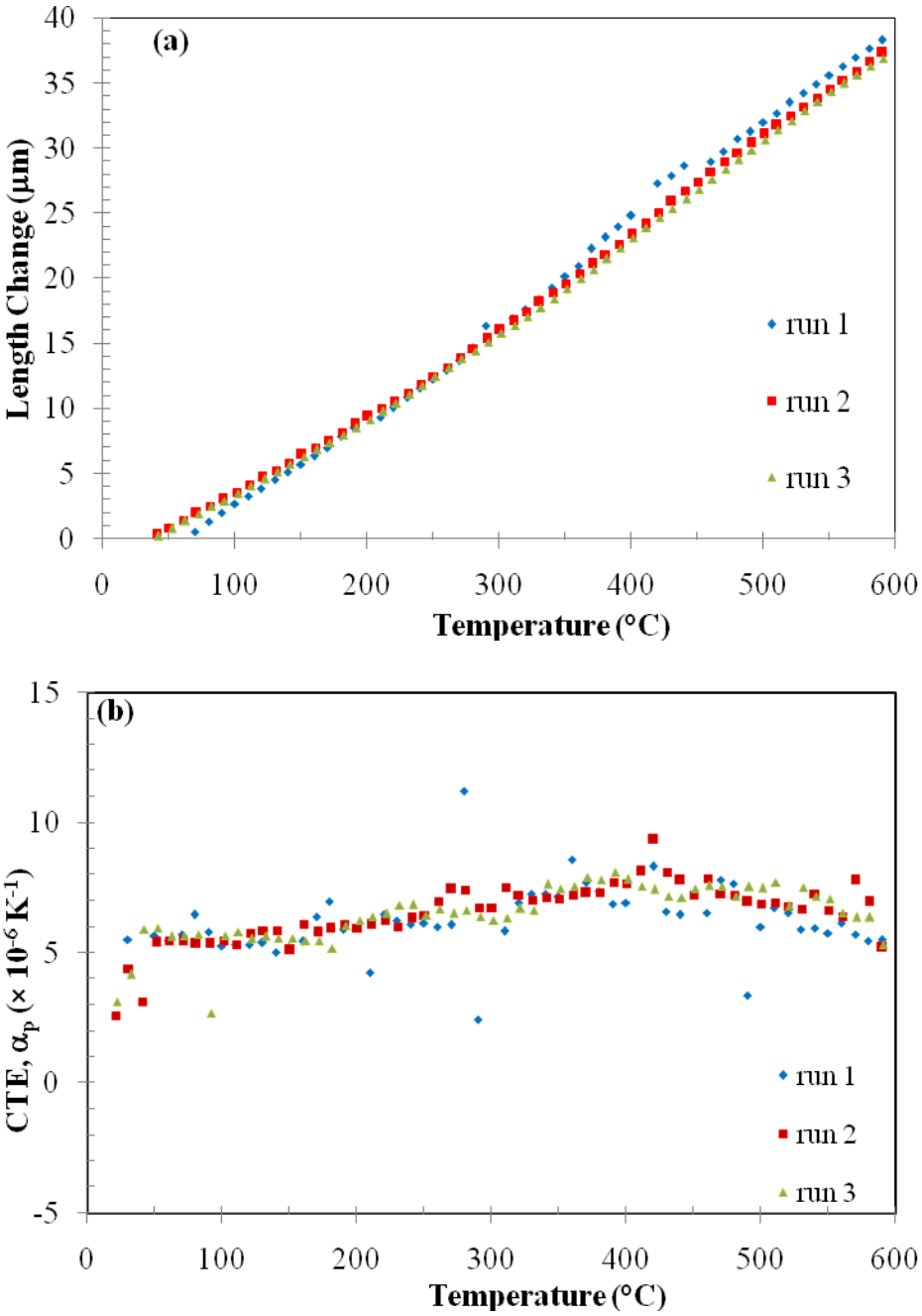

Figure 7.3: The length change (a) and CTE, α_P (b) as a function of temperature for annealed graphite composite 0:80:20 wt. % (NG:SG:Novolac).

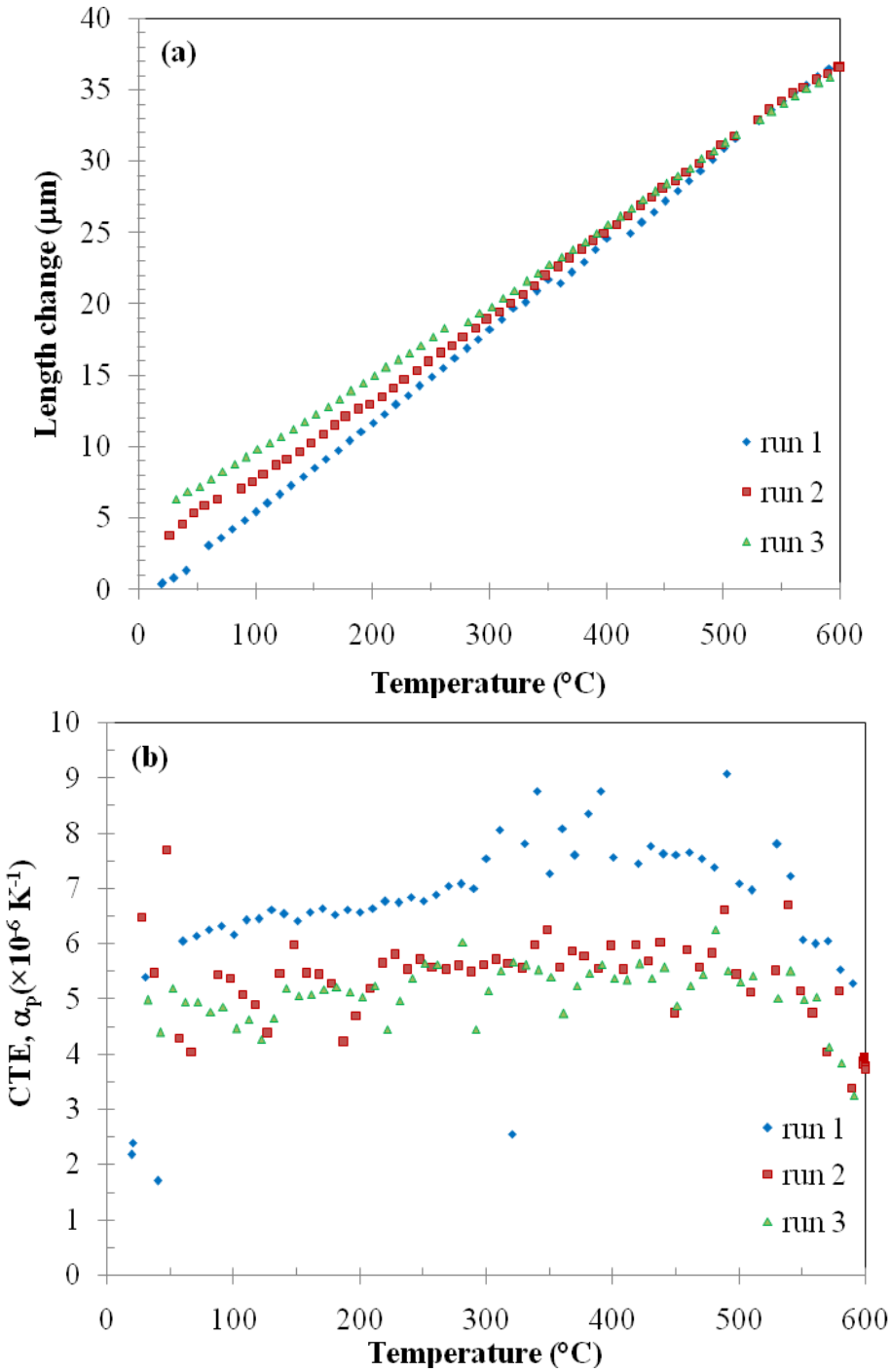

Figure 7.4: The length change (a) and CTE, α_P (b) as a function of temperature for annealed graphite composite 16:64:20 wt. % (NG:SG:Novolac).

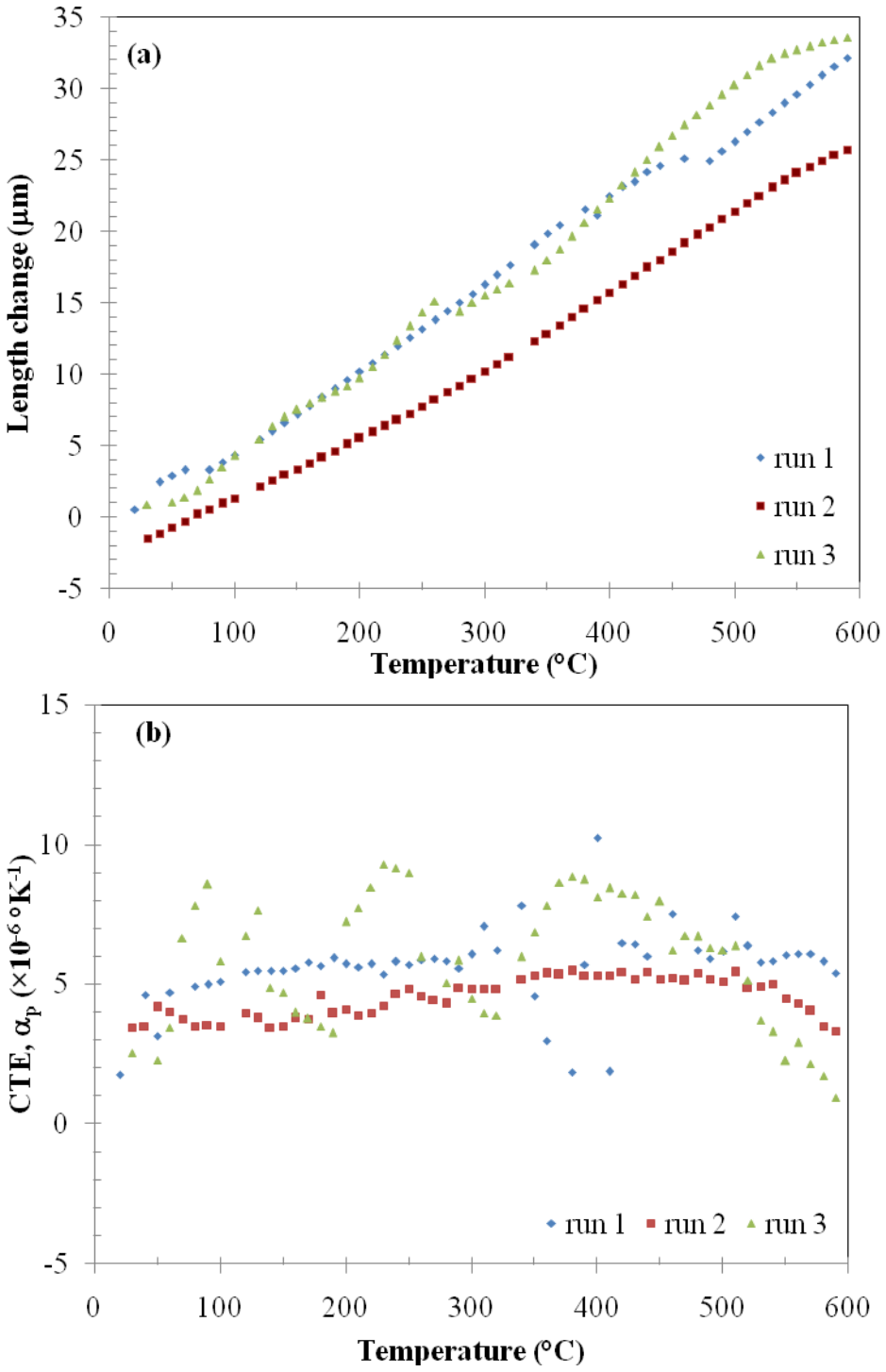

Figure 7.5: The length change (a) and CTE, α_P (b) as a function of temperature for annealed graphite composite 40:40:20 wt. % (NG:SG:Novolac).

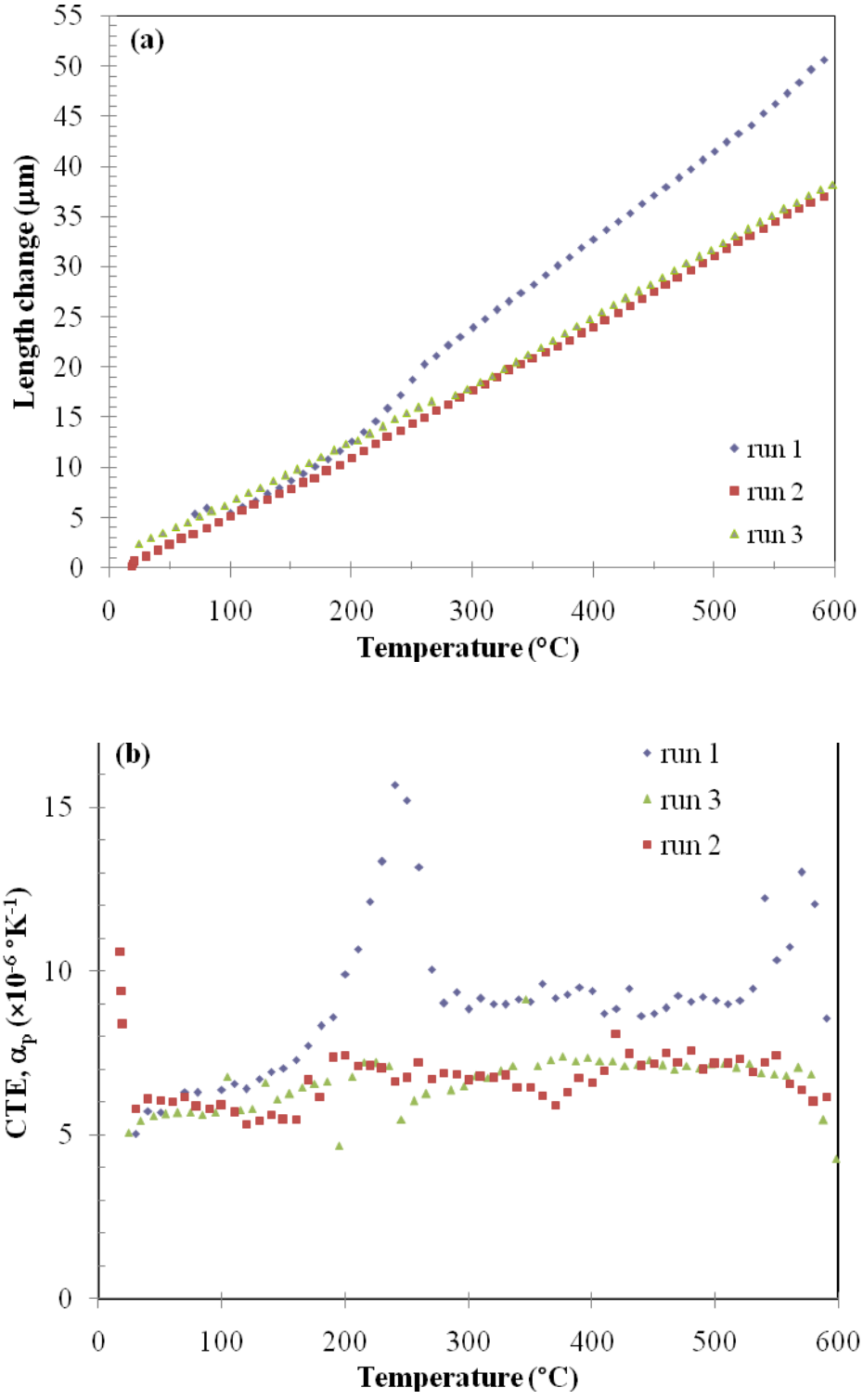

Figure 7.6: The length change (a) and CTE, α_P (b) as a function of temperature for annealed graphite composite 64:16:20 wt. % (NG:SG:Novolac).

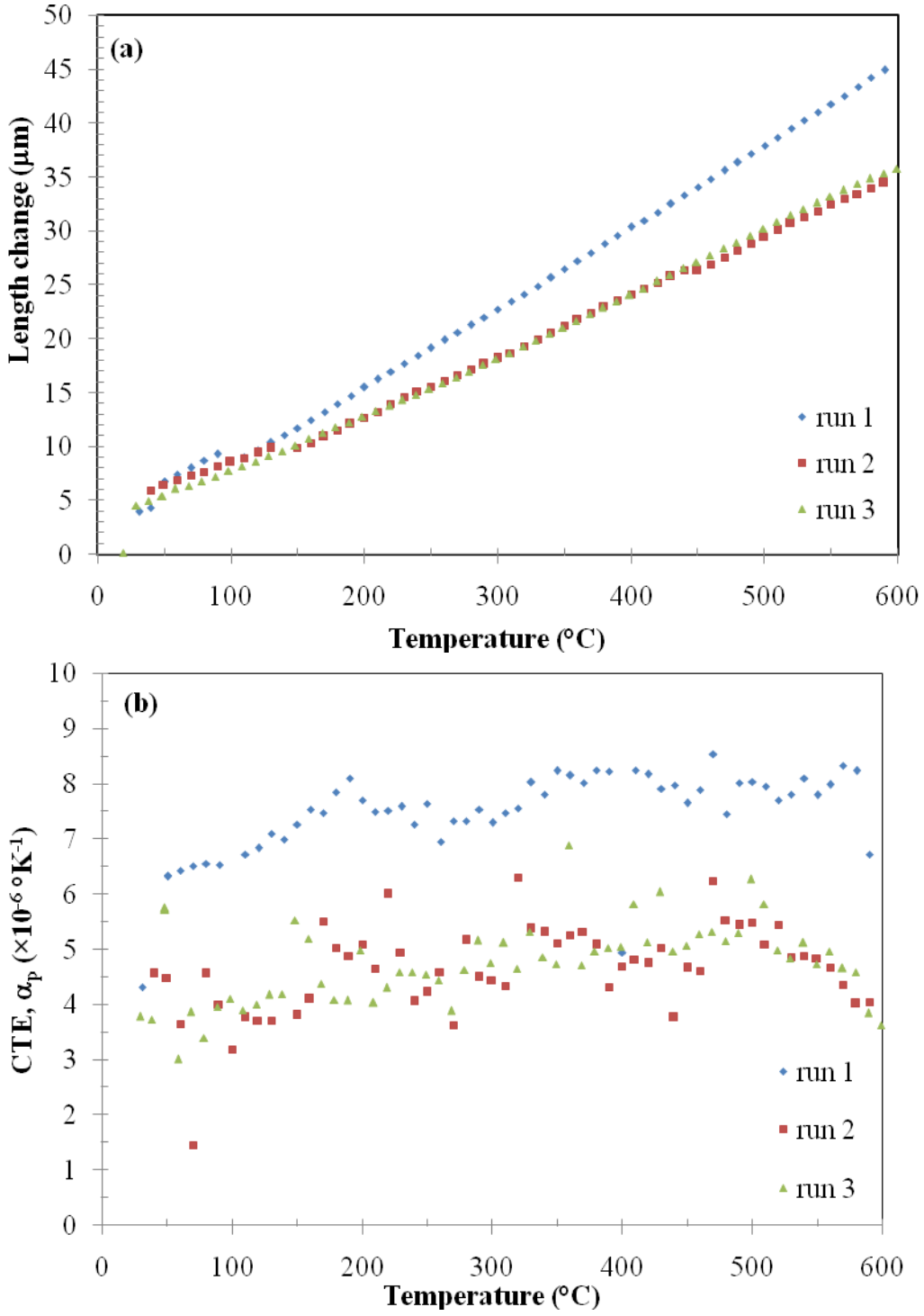

Figure 7.7: The length change (a) and CTE, α_P (b) as a function of temperature for annealed graphite composite 80:0:20 wt. % (NG:SG:Novolac).

Clearly a composite containing 64 wt.% NG showed slightly higher average α_P value than the other composites. Also it can be noted that composites containing mainly synthetic graphite expanded less in the pressing direction than those containing mainly natural graphite as a major component.

The average α_P values of the annealed graphite composites attained in this work were similar to reported literature CTE values of nuclear graphites recorded in the temperature range 20-120 °C, i.e. 5.3×10^{-6} K^{-1} for isotropic graphites and for anisotropic graphites 2.2×10^{-6} K^{-1} with grain and 3.8×10^{-6} K^{-1} against grain (Cohn et al., 2005). Hacker et al. (Hacker et al., 2000) also reported thermal expansion coefficients of extruded PGA graphite in this temperature range using dilatometry and obtained similar CTE values. For example, they reported that the average CTE in the direction parallel to extrusion direction was 2.5×10^{-6} K^{-1} while in the direction perpendicular to extrusion direction the average CTE value was 5.5×10^{-6} K^{-1}.

The spherical graphite matrix composites used in various gas cooled reactors (AVR, THTR and HTR-10) reported in literature showed lower CTE values (i.e. (2.43-2.89) $\times10^{-6}$ $^oC^{-1}$) in the direction parallel to equatorial plane of the spheres when compared to CTE values (i.e. 5.70-7.88) $\times10^{-6}$ $^oC^{-1}$) of the graphitic matrix composites obtained in the direction parallel to compression moulding direction. However, the said reported literature values are only based on the composition of 64:16:20 (NG:SG:Novolac wt.%.) and there are no reported literature values on other compositions.

The expansion measurements were also performed in the direction normal to pressing and similar expansion behaviour was observed as in the pressing direction. The maximum length change for a composite 0:80:20 was approximately 13 μm (see Figure 7.8(a)). The instantaneous α_N values, as shown in Figure 7.8(b), for this composite were in the range (0.0-5.6) $\times10^{-6}$ K^{-1}.

The average α_N value for this composite was (2.06±0.50) $\times 10^{-6}$ K^{-1}. A composite containing 16 wt.% NG (i.e. 16:64:20) had a maximum length change of 10 µm as it can be observed in Figure 7.9 (a). The instantaneous α_N values for this composite ranged from (0.3-5.1) $\times 10^{-6}$ K^{-1}. The average α_N value was (1.74±0.31) $\times 10^{-6}$ K^{-1}. A composite containing equal amount of the filler graphites, (see Figure 7.10) showed a maximum length change of 12.5 µm. The instantaneous α_N value observed were in the range (0.1-4.5) $\times 10^{-6}$ K^{-1}. The average α_N value obtained was (2.08±0.44) $\times 10^{-6}$ K^{-1}.

A composite containing 64 wt.% NG (i.e. 64:16:20) showed a maximum length change of 15 µm. Its α_N values were in the range (-1.6-10.3) $\times 10^{-6}$ K^{-1}. The average α_N value for this composite was (2.00±0.17) $\times 10^{-6} K^{-1}$. A composite containing only natural graphite and binder (i.e. 80:0:20) showed a maximum length change of approximately 15 µm. The α_N values for this composite ranged from (0.1-6.2) $\times 10^{-6}$ K^{-1}. The average α_N value for this composite was (1.91±0.45) $\times 10^{-6}$ K^{-1}. The measured CTE, α_N values were similar to reported literature values (Rind, 1981) (Schulze et al., 1981) (IAEA, June 2012) (Tang et al., 2008) (Cohn et al., 2005, Hacker et al., 2000) as shown in Table 7.1 and Table 2.2. The mean CTE values obtained in the direction perpendicular to pressing direction in this work were in the range (1.74-2.08)$\times 10^{-6}$ K^{-1} whilst those reported in literature were in the range (2.69-3.45)$\times 10^{-6}$ K^{-1}.

The annealed graphite composites showed to be expanding three times more parallel to compression moulding direction than in the direction normal to compression moulding direction. The length change also showed similar behaviour as the samples were much elongated in the pressing direction than in the direction perpendicular to pressing. In the pressing direction, the average CTE, α_p values seem to increase with the increase in the natural graphite content in the composite. The reason for this is that as the natural graphite content increase in the composite

(see Table 7.1), the open porosity decreases (i.e. bulk density increase) and therefore accommodation of expansion by the open porosity diminishes.

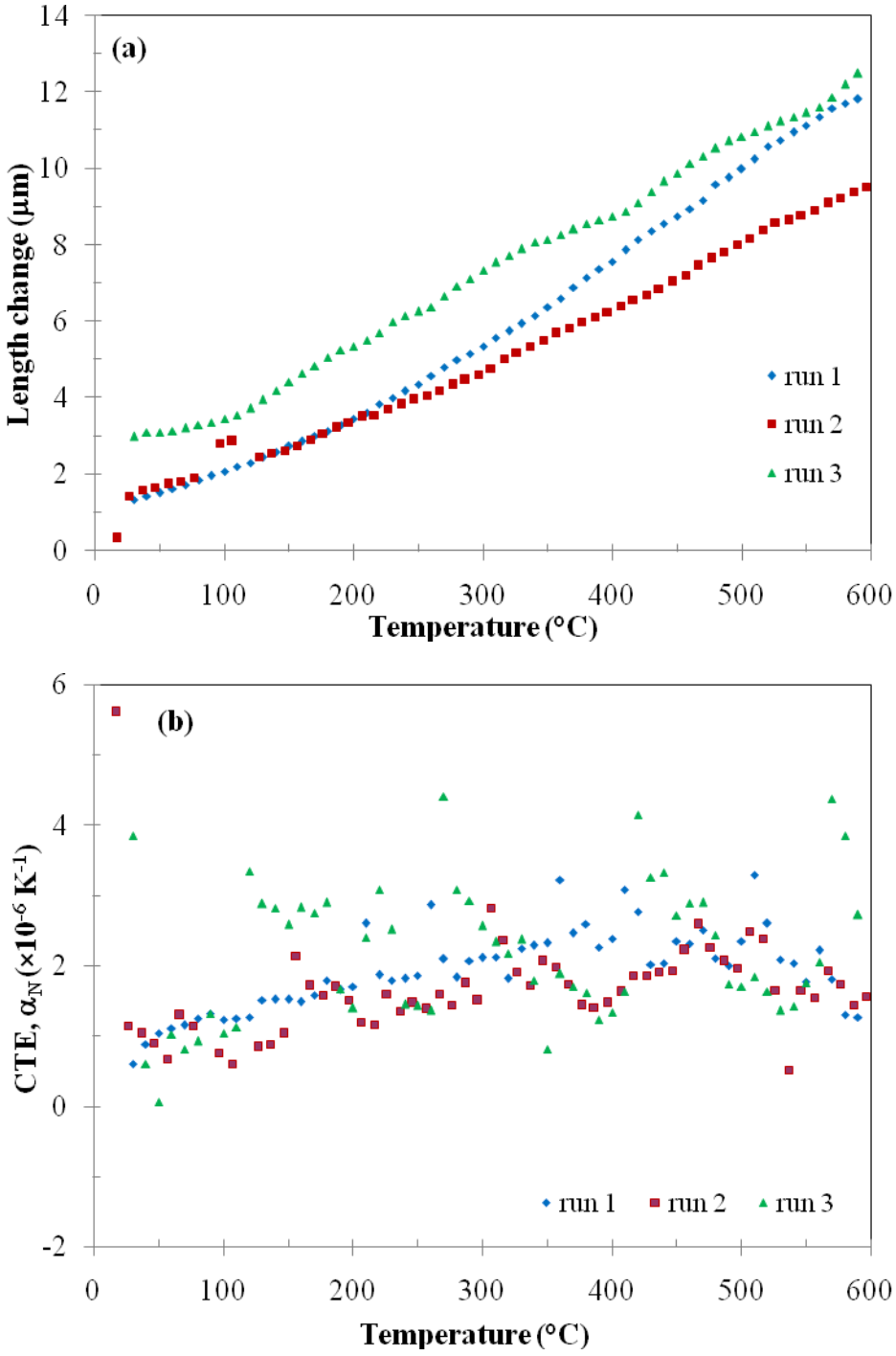

Figure 7.8: The length change (a) and CTE, α_N (b) as a function of temperature for annealed graphite composite 0:80:20 wt. % (NG:SG:Novolac).

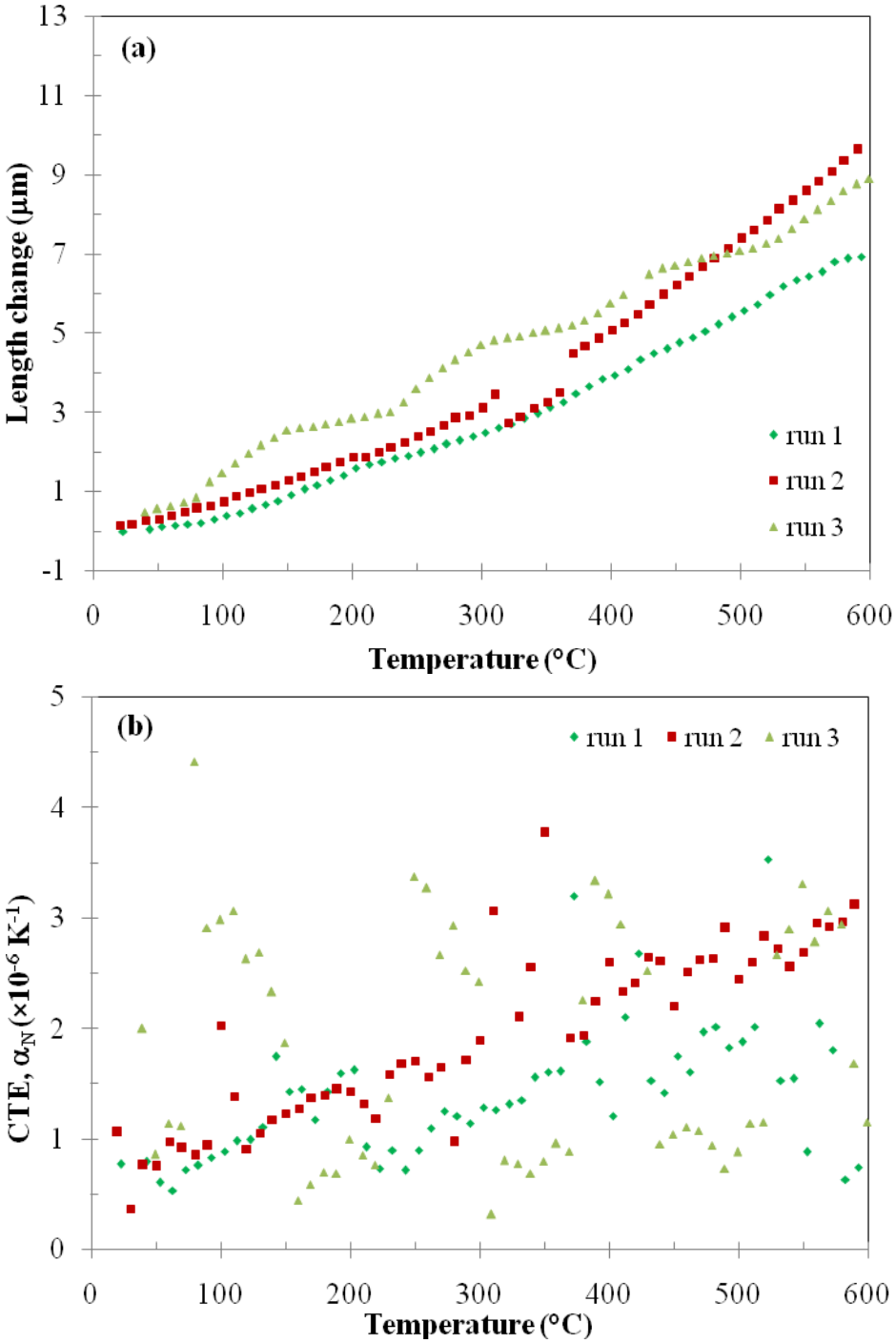

Figure 7.9: The length change (a) and CTE, α_N (b) as a function of temperature for annealed graphite composite 16:64:20 wt. % (NG:SG:Novolac).

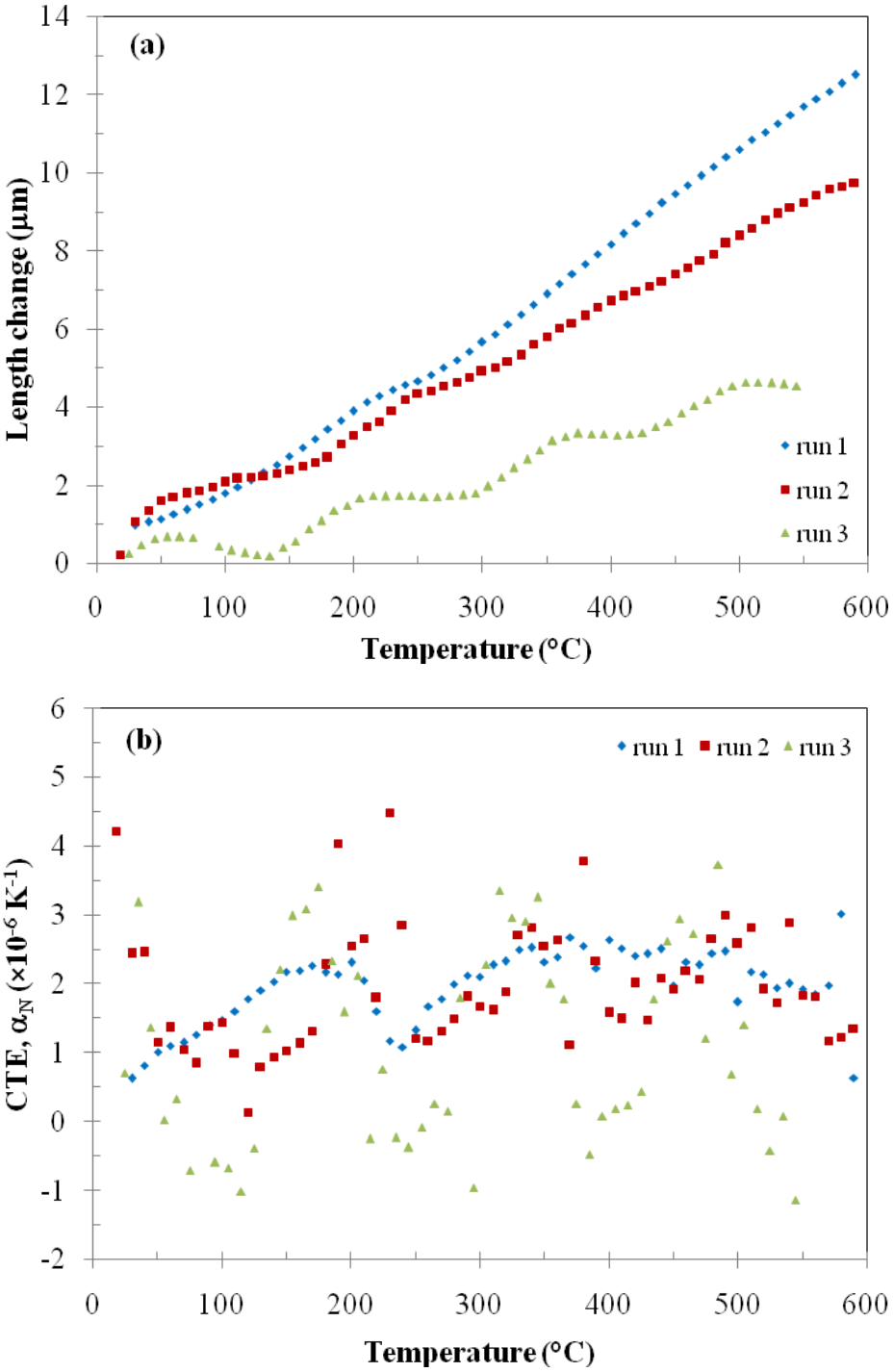

Figure 7.10: The length change (a) and CTE, α_N (b) as a function of temperature for annealed graphite composite 40:40:20 wt. % (NG:SG:Novolac).

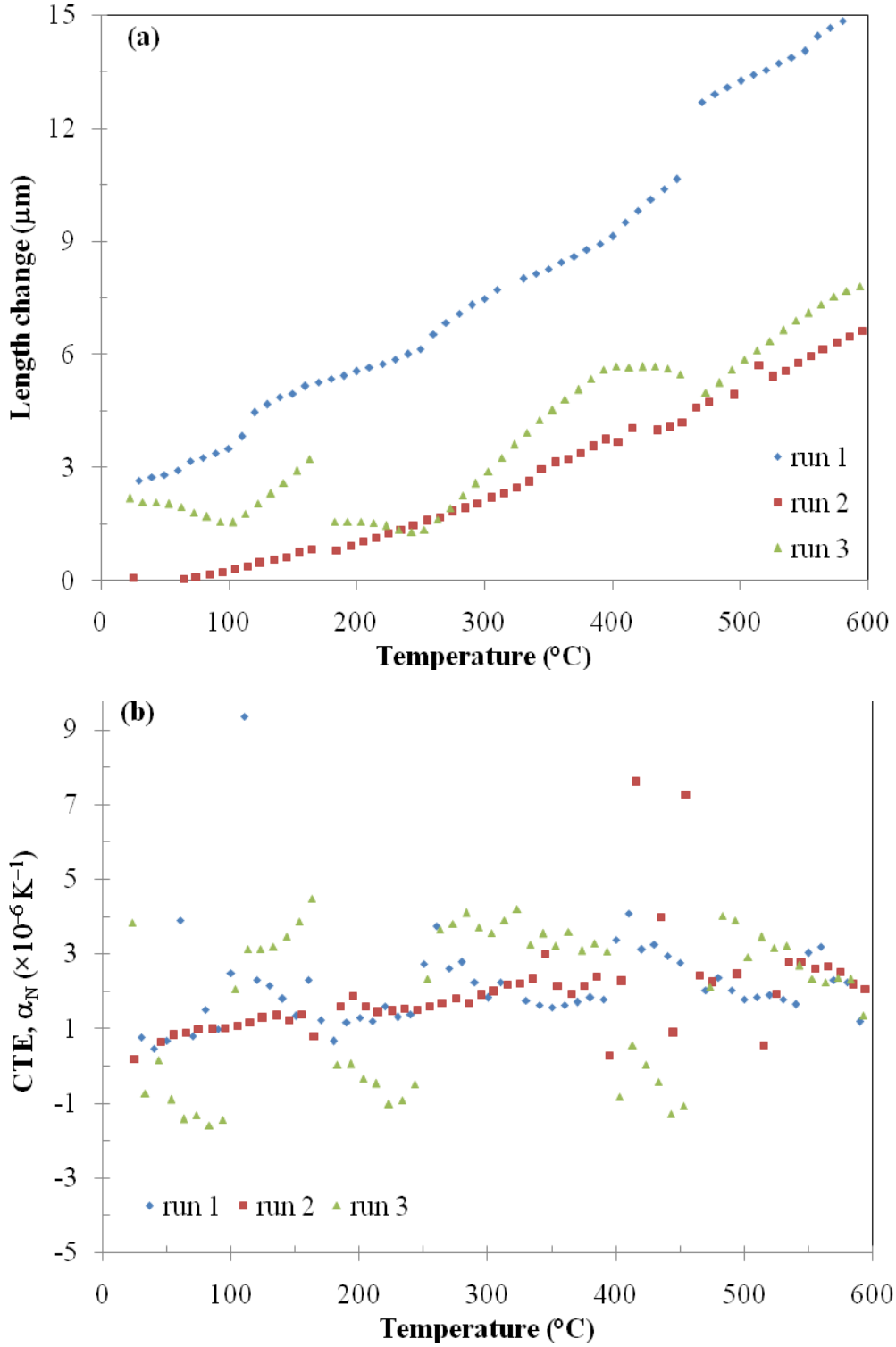

Figure 7.11: The length change (a) and CTE, α_N (b) as a function of temperature for annealed graphite composite 64:16:20 wt. % (NG:SG:Novolac).

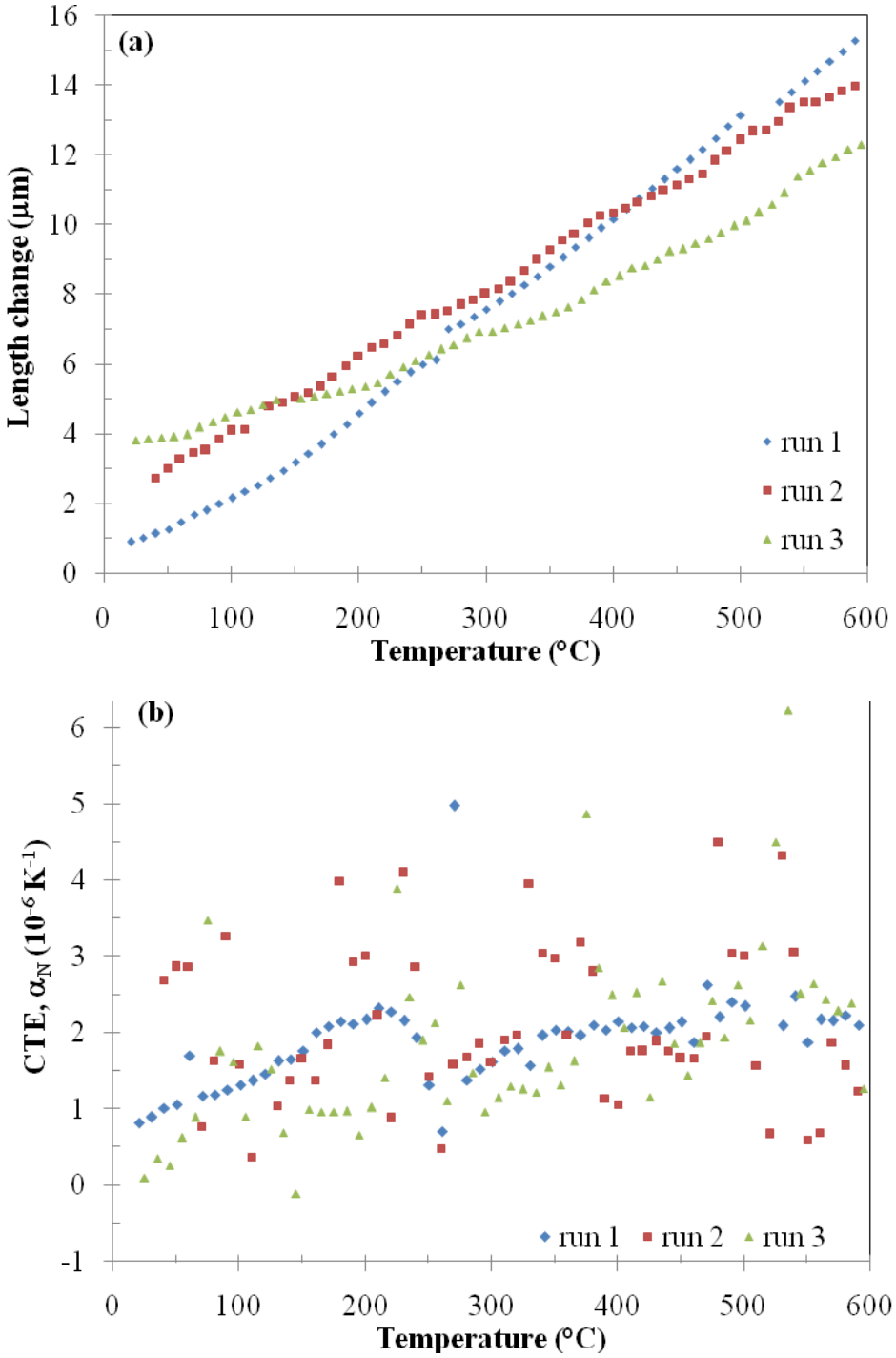

Figure 7.12: The length change (a) and CTE, α_N (b) as a function of temperature for annealed graphite composite 80:0:20 wt. % (NG:SG:Novolac).

The other important point is that there could be preferred crystal orientation in the direction of pressing. This phenomenon has been well documented (Sutton and Howard, 1962, Price and

Bokros, 1965). The increase in bulk density means that the natural graphite flake particles are more compressible than the needle-like synthetic graphite particles. It is interesting that the average CTE, α_N value were constant at approximately 2×10^{-6} K^{-1} irrespective of the composition and open porosity. The anisotropic ratio in expansion (α_p:α_N) in the temperature range 20-600 °C was greater than two for all the annealed graphite composites as shown in Table 7.1. This anisotropy was caused by the alignment of the graphite particles (i.e. flakes or needle cokes particles) during pressing as shown by optical micrographs in Figures 6.10-12. Clearly the graphite particles align themselves in the direction normal to pressing and therefore this causes them to expand more when they are heated from their sides or surfaces. When heated from their edges, which is the case when measuring expansion in the direction normal to pressing, the particles expands much less.

The graphite matrix composites reported in literature, see Table 7.1, showed to be isotropic in expansion in the temperature range 20-500 ºC. Their α_P:α_N ratios were all close to 1.0, this was mainly due to isostatic pressing employed during their fabrication which aligned the filler particles randomly in the spheres.

7.3 Xenon Flash Photolysis

The thermal conductivity of the annealed graphite composites was calculated from measured thermal diffusivity, specific heat capacity and density values at each measurement temperature. The bulk densities of the annealed graphite composites were predicted at each temperature using known thermal expansion and bulk densities of a thermographite reference sample. The predicted bulk densities as a function of temperature are shown in Figure 7.13. Generally, the bulk density decreases slightly with the increase in temperature in the composites. The decrease

is due to volumetric expansion as temperature increases as expected. The percentage decrease in the bulk density was in the range 1.81-1.85 % in all the composites. A composite containing 16 wt.% NG (16:64:20) showed larger bulk density values at each measurement temperature while the one containing only synthetic graphite and binder (0:80:20) showed lower bulk density values. A similar trend has been observed during room temperature measurements using pycnometry (see Table 6.5). The predicted bulk densities at 100 °C were lower than the room temperature bulk density values measured using pycnometry (see Table 6.5) by at most 7 %.

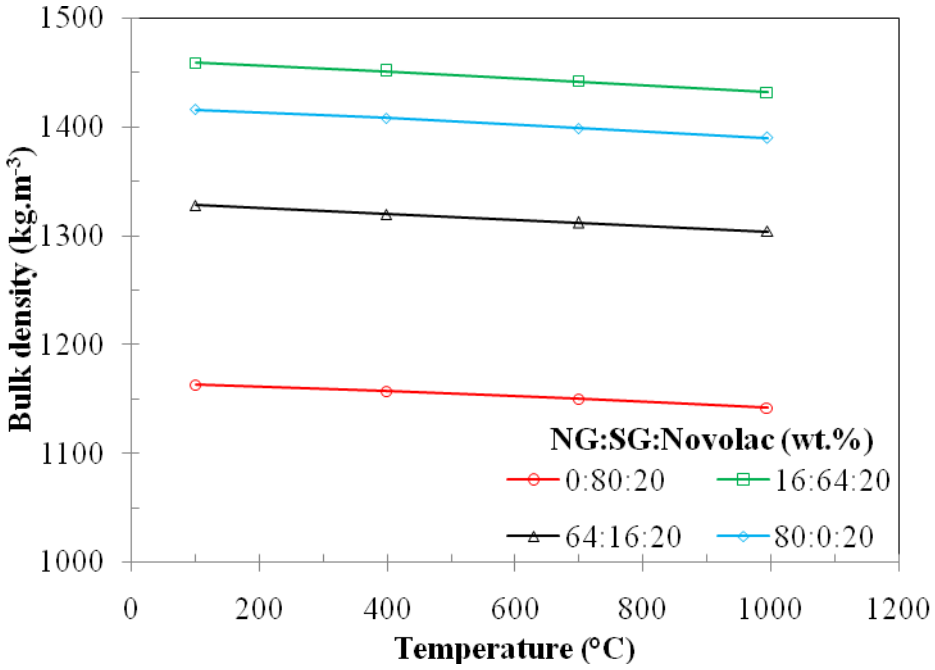

Figure 7.13: Temperature dependence of the bulk density, ρ, of the annealed graphite composites.

This gave us confidence in the predicted bulk density values we used in computing thermal conductivity. The temperature dependence of specific heat, C_p, values of the annealed graphite composites obtained in the compression moulding direction are shown in Figure 7.14. By

definition specific heat is the amount of heat (energy transfer) per unit mass that is required to raise the temperature of the material by one degree Celcius without any phase change. The specific heat increases with temperature for all the composites. A composite containing 16 wt.% NG (16:64:20) showed larger specific heat values at any measurement temperature than other composites. A composite containing only NG and binder, i.e. 80 wt.% NG (80:0:20), showed lower specific heat values than other composites.

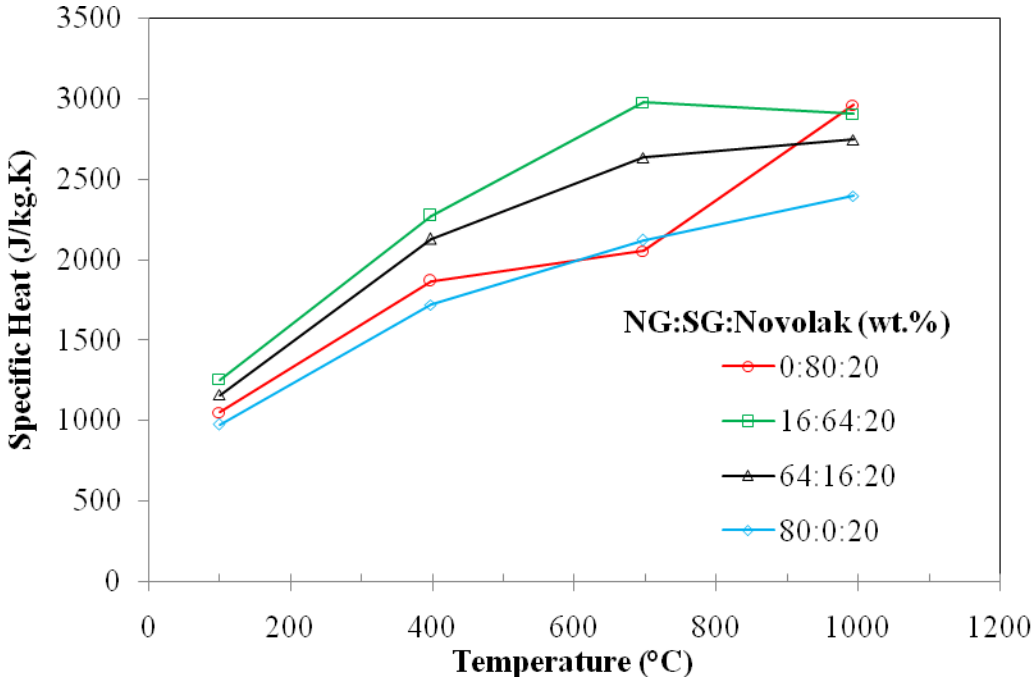

Figure 7.14: Temperature dependence of the specific heat, C_p, of the annealed graphite composites measured in the compression moulding direction.

The temperature dependence of thermal diffusivity, α, of the annealed graphite composites obtained in the compression moulding direction are shown in Figure 7.15. Thermal diffusivity is a measure of how fast the material can transfer heat from one 'hot' side to a 'colder' one. The

thermal diffusivity of the annealed graphite composites decreases with the increase in temperature. This is because in graphite heat transfer or conduction occurs mainly via lattice vibrations. As the temperature increases, phonon scattering becomes prominent. A composite containing 64 wt.% NG (64:16:20) showed larger thermal diffusivity values at a given measurement temperature whilst the one containing only synthetic graphite and binder (0:80:20) showed lower thermal diffusivity values. This is related to high open porosity and structural defects (as shown by XRD and Raman data) observed in the latter.

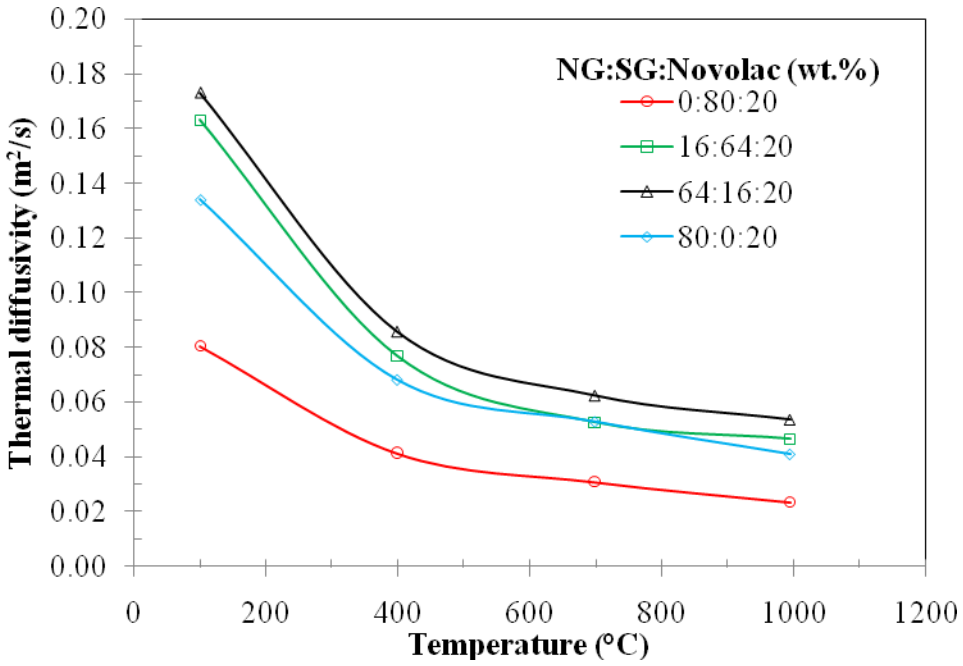

Figure 7.15: Temperature dependence of the thermal diffusivity, α, of the annealed graphite composites measured in the compression moulding direction.

From the predicted bulk density values (Figure 7.13) and measured specific heat (Figure 7.14) and thermal diffusivity values (Figure 7.15); the thermal conductivities of the annealed graphite composites were computed using Equation (4.6). The temperature dependence of thermal

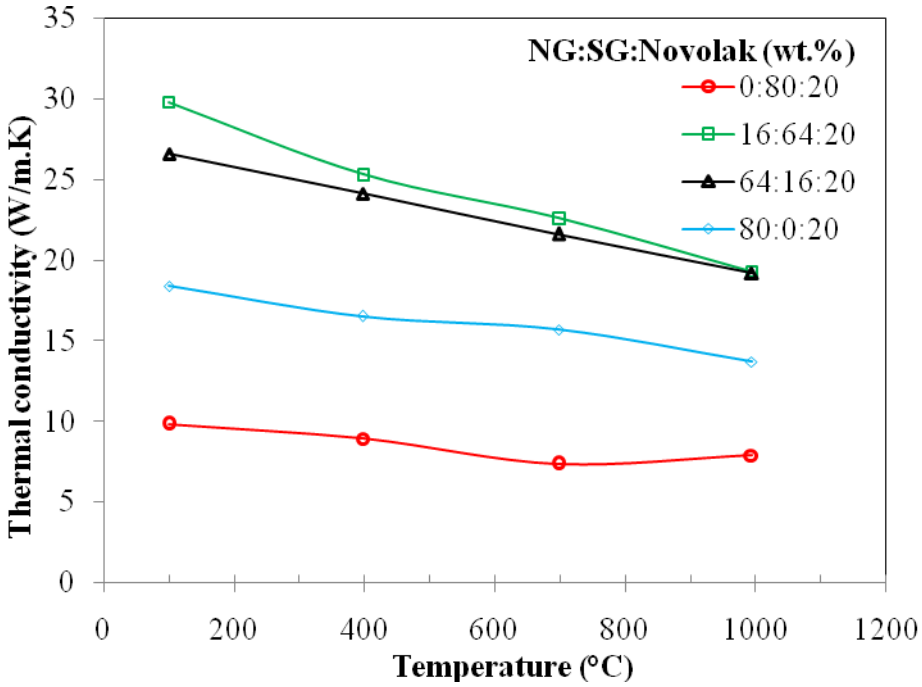

Figure 7.16: Temperature dependence of the thermal conductivity, κ, of the annealed graphite composites measured in the compression moulding direction.

conductivity of the annealed graphite composites measured in the direction of pressing is shown in Figure 7.16. Generally the thermal conductivity values decreased with increasing temperature for all the annealed composites studied. This is because in graphite (which is the main component in the composites) heat conduction occurs mainly via lattice vibrations. As the temperature rises, phonon scattering becomes more pronounced and thus the thermal conductivities diminish (Taylor et al., 1968, Kelly and Gilchrist, 1969). A composite containing only SG and binder, i.e. 0 wt.% NG (0:80:20), showed lower values of thermal conductivity at a given measurement temperature. The thermal conductivity for this composite decreased from 9.8 $W.m^{-1}.K^{-1}$ at 100 °C to 7.9 $W.m^{-1}.K^{-1}$ at 1000 °C (i.e. a 19.4% decrease). The composite containing 16 wt.% NG (16:64:20) showed higher thermal conductivities than other composites; it had a value of 29.8 $W.m^{-1}.K^{-1}$ at 100 °C and 19.3 $W.m^{-1}.K^{-1}$ at 1000 °C (35.4 % decrease). The

composite containing 64 wt.% NG (64:16:20) showed thermal conductivity values similar to those of 16 wt.% NG composite, i.e. 26.6 $W.m^{-1}.K^{-1}$ at 100 °C to 19.2 $W.m^{-1}.K^{-1}$ at 1000 °C (27.8 % decrease). The composite containing only NG and binder (80:0:20) showed values intermediate between the extremes; 18.4 to 13.7 $W.m^{-1}.K^{-1}$ at 100 and 1000 °C, respectively (decrease of 25.5 %). The contribution of the binder resin carbon to thermal conductivity values was very small since it had a very low thermal conductivity of approximately 0.3 $W.m^{-1}.K^{-1}$ at room temperature. In addition all the composites studied here contained the same amount of the binder resin and thus its influence should be the same. The composite containing only SG and binder showed lower thermal conductivity values possibly for the following reasons:

- It had a higher open porosity than other composites (i.e. 41 %); this also evident from the polarised micrograph in Figure 6.10(b). It is well known that thermal conductivity decreases with increase in open porosity because heat transfer across pores is slow and inefficient (Matsuo, 1980).
- Since these composites are polycrystalline and it has been shown that a composite containing 0 wt.% NG (0:80:20) had more structural disorder or defects than other composites (see XRD and Raman data), therefore the low thermal conductivity values could be due to phonon scattering effects at crystallite boundaries consistent with literature (Taylor et al., 1968, Kelly and Gilchrist, 1969).

The composites containing mainly NG flakes were easily compactable compared to those containing SG needle-like particles as evidenced by their high bulk densities. They also had larger aspect ratios, i.e. length: thickness ratio and therefore this is the reason why they conducted heat so well. This study found that the flakes orient themselves in the direction normal to pressing consistent with literature (Mariner and Sayir, 1999). However the thermal

conductivity values reported here were only obtained in the pressing direction due to sample geometry restrictions. The instrument as mentioned in the experimental section requires samples of 20 mm in diameter; unfortunately samples made in this work were 10 mm in height (see Figure 5.2) and therefore these measurements could not be made in the direction perpendicular to pressing direction. However we expect that the thermal conductivity values in the direction transverse to pressing could be significantly higher than those attained in the pressing direction because of the fact that it will be in the direction of the flakes.

The thermal conductivity values of the annealed graphitic composites measured at 1000 °C in this work were compared to the values of similar composites reported in literature as shown in Table 7.2. Generally the values obtained in the direction parallel to pressing (in this work) are lower than those of similar graphite matrix composites reported in literature. The thermal conductivities of the annealed graphitic composites containing only synthetic graphite and binder (0:80:20) and the one containing only natural graphite and binder (80:0:20) were very low compared to reported literature values, see Table 7.2.

Table 7.2: The thermal conductivity values at 1000 °C of the annealed graphitic composites in the compression moulding direction and literature values of similar composites.

Composition (NG:SG:Novolac) wt.%	**Thermal conductivity at 1000 °C ($W.m^{-1}K^{-1}$)**
0:80:20	7.9
16:64:20	19.3
40:40:20	-
64:16:20	19.2
80:0:20	13.7
A3-3 (AVR)[a]	26
A3-3(THTR)[a]	41
A3-3 (HTR-10)[b]	29.3
A3-27(AVR)[a]	44

[a](Rind, 1981, Schulze et al., 1981, IAEA, June 2012) [b](Tang et al., 2008)

However, the annealed graphitic composites containing 16:64:20 and 64:16:20 wt.% showed slightly closer thermal conductivity values at 1000 °C (i.e. 19.3 and 19.2 $W.m^{-1}K^{-1}$, respectively) compared to the values of the A3-3 matrix composites used in AVR and HTR-10 reactors having values of 26 and 29.3 $W.m^{-1}.K^{-1}$, respectively. The matrix composites A3-3 (THTR) and A3-27 (AVR) had very high thermal conductivity values compared to all composites made in this work. The reason for higher values observed for the literature composites is mainly due to their higher bulk density (1.70-1.74 $g.cm^{-3}$) as compared to the measured bulk densities (1.24-1.52 $g.cm^{-3}$) of the composites made in this work. It is also important to note that the literature values for AVR, THTR and HTR-10 are only based on the A3-3 and A3-27 matrices or composites. These composites contain only 64 wt.% natural crystalline graphite, 16 wt.% petroleum coke graphite and 20 wt.% phenolic resin.

7.4 Mechanical properties

7.4.1 Flexural Strength

The mechanical properties, i.e. flexural strength and modulus, were measured using four-point bending tests in accordance with ASTM standard C651-91 (Reapproved 2000). These properties were measured both in the direction of pressing and in the direction normal to pressing. The load-deflection curves of the annealed composite samples of various compositions attained in the pressing direction are shown in Figure 7.17 to Figure 7.20. All the composites showed linear load-deflection curves in the pressing direction except at initial lower deflection values.

The load-deflection curve for a composite containing only synthetic graphite and binder, i.e. 0:80:20, is shown in Figure 7.17. At least three samples per composition were tested. On average this composite experienced a catastrophic failure when a maximum load of 71.8 N was applied on it after which it was broken. The average maximum deflection for this composite was 0.22 mm. The bending or flexural strength (σ_P and σ_N) values for the composites, calculated using equation (4.8), are shown in Table 7.1. The average σ_p value for this composite was 8.61±0.59 MPa. The load-deflection curves for a composite containing 16 wt.% NG (i.e. 16:64:20) are shown in Figure 7.18. This sample experienced a catastrophic failure when the average maximum load of 91.6 N was applied. The average maximum deflection for this composite was 0.27 mm. The average σ_P value for this composite was 11.00±1.88 MPa. This shows that the slight increase in the natural graphite content to the synthetic graphite composite result in improvement in strength by about 28 %. The load-deflection curves for a composite containing equal amount of the filler graphites (i.e. 40:40:20) are shown in Figure 7.19.

Like in the other composites discussed, this composite also experienced a catastrophic failure.

The observed average maximum load at break was 41.3 N. The average maximum deflection for this composite was 0.22 mm. The average σ_P value for this composite was 4.96±1.26 MPa. Similar load-deflection curves were attained for a composite containing 64 wt.% NG as shown in Figure 7.20. This composite failed at the average maximum load of 85.2 N and the corresponding average maximum deflection on the samples was 0.30 mm. The average σ_P value for this composite was 10.23±2.12 MPa. A composite containing only natural graphite and binder (i.e. 80:0:20) was very weak and did not withstand the tests.

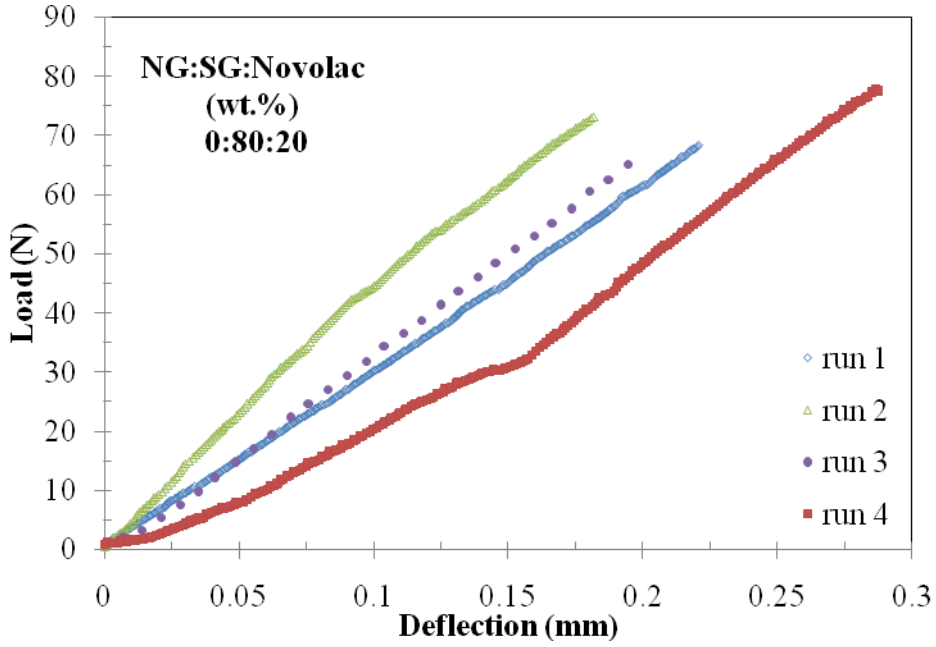

Figure 7.17: The load-deflection curves for samples of annealed graphite composite 0:80:20; the loading was done in the pressing direction.

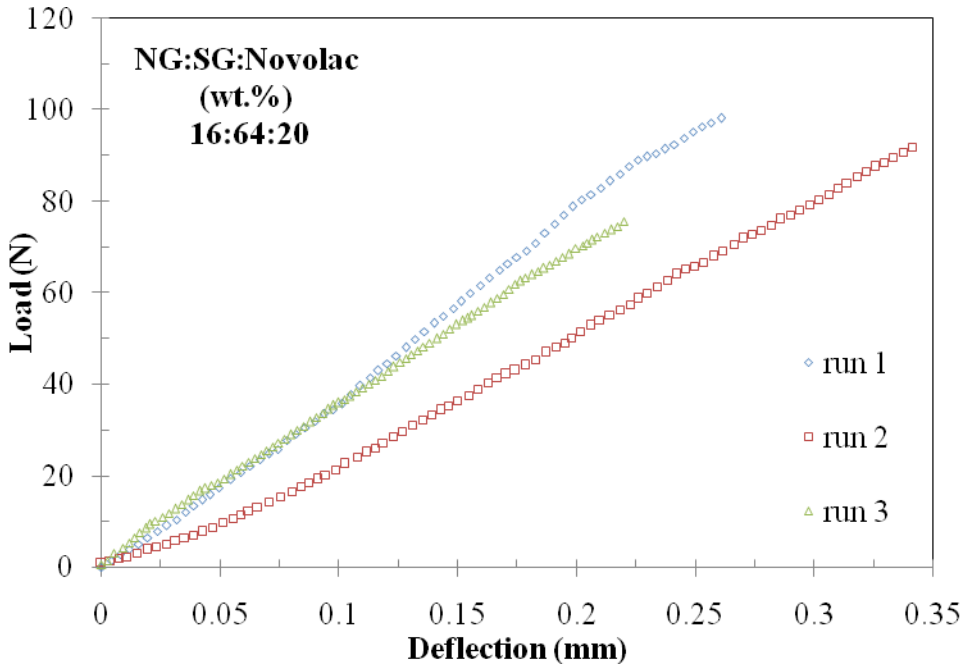

Figure 7.18: The load-deflection curves for samples of annealed graphite composite 16:64:20; the loading was done in the pressing direction.

Table 7.3: Flexural or bending strength of the graphite-carbon composites annealed (in a He atmosphere) at 1800 °C for 2 hours.

Green State Composition NG:SG:Novolac (wt.%)	**Bending strength, σ_P (MPa)**	**Bending strength, σ_N (MPa)**	**Anisotropy in strength (σ_P:σ_N)**
0:80:20	8.61±0.59	7.32±2.67	1.2
16:64:20	11.00±3.57	3.39±1.04	3.2
40:40:20	4.96±1.26	3.18±1.76	1.5
64:16:20	10.23±2.12	9.28±0.40	1.1
80:0:20	-	-	-

From this data we note that the composite containing 40 wt.% NG (i.e. 40:40:20) featured a lower flexural strength than other composites. This is peculiar because a composite containing only synthetic graphite and binder had higher open porosity (41.9 %) but it was much stronger under flexure than the 40:40:20 composite (having 33.6 % open porosity); see Figure 7.21. I do not fully understand what causes this behavior but we think it might be related to differences in the anisotropy of the different graphite particles during uniaxial compression moulding.

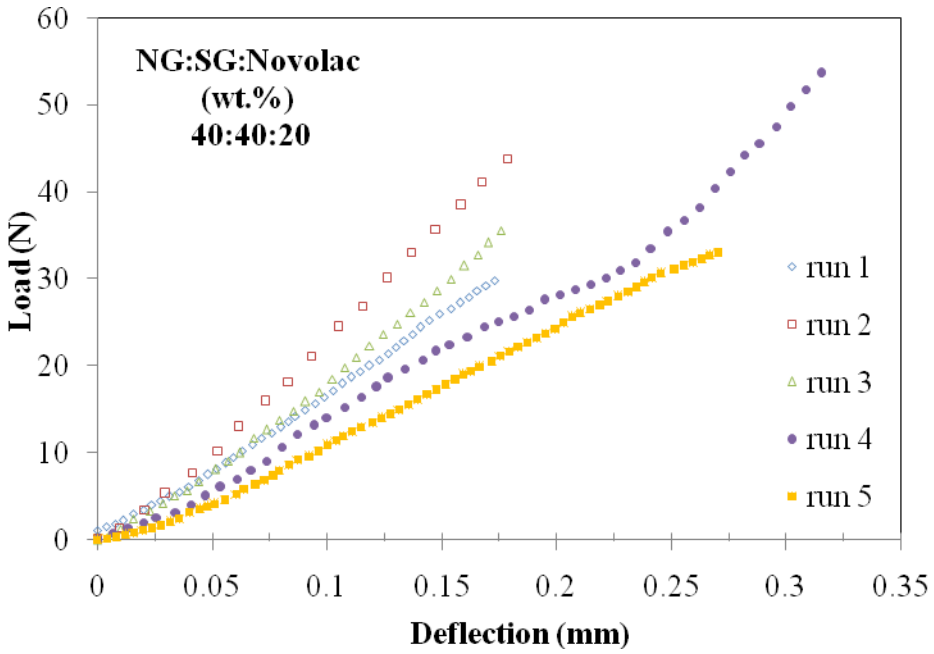

Figure 7.19: The load-deflection curves for samples of annealed graphite composite 40:40:20; the loading was done in the pressing direction.

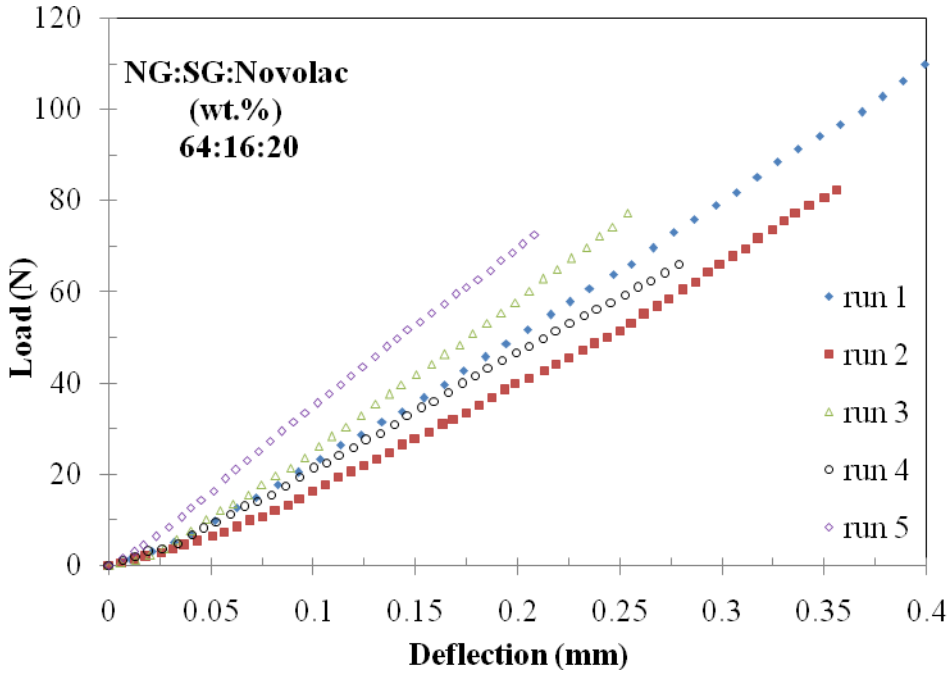

Figure 7.20: The load-deflection curves for samples of annealed graphite composite 64:16:20; the loading was done in the pressing direction.

Another important factor is that the mean particle size for the 40:40:20 composite was larger than that of the other composites (see Table 6.1) and therefore the particles in this composite could be weakly bonded to each other. This is partly an explanation for a weaker strength observed. This is consistent with reported literature that the larger the graphite particle size, the lower the flexural strength (Zhang et al., 2005). Another possibility is that there could be a compromise in flexural strength due to change in particles shape since the composite contains equal amount of flake-like and needle-like particles (Zhang et al., 2005, Heo et al., 2006). The flake-like particles seem to be more compressible than the needle-like particles as evidenced by the measured bulk densities. It can be seen in Figure 7.21 that the flexural strength in the pressing direction decreases linearly with increase in open porosity. The composites 16:64:20 and its mirror image, i.e. 64:16:20 showed larger flexural strength values than other composites. Both composites showed comparable flexural strength values. We have observed that a composite containing only natural graphite and binder (80:0:20) was much weaker as it failed on loading but when it was spiked with 16 wt % SG, the strength improved tremendously to 10.23±2.12 MPa. The same observation was noted when a composite containing only synthetic graphite and binder (0:80:20) was spiked with 16 wt.% NG; the flexural strength improved from 8.61±0.59 MPa to 11.00±3.57 MPa.

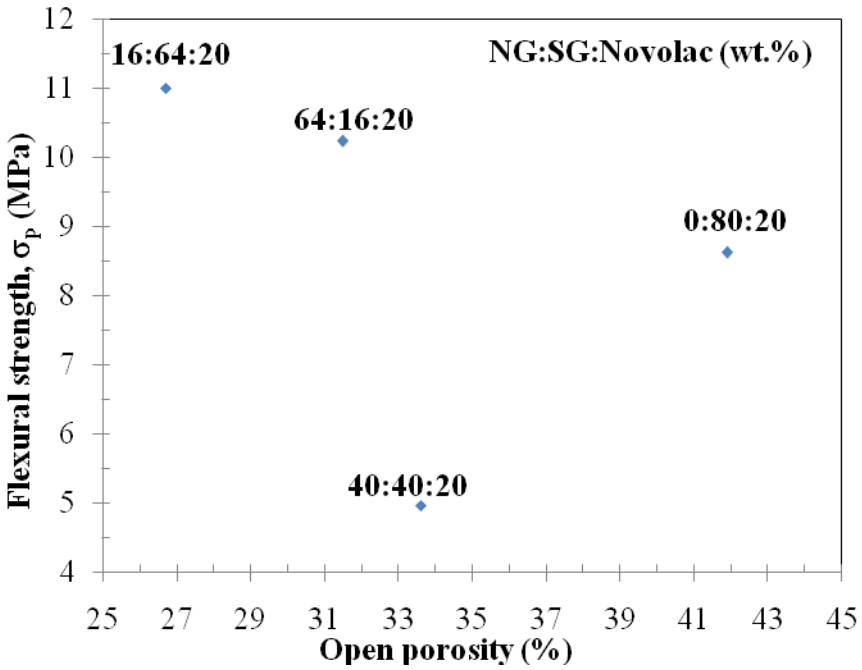

Figure 7.21: Flexural strength dependence on open porosity of the annealed graphite composites in the pressing direction.

This is interesting because it means that the filler graphite particles complement each other as far as flexural strength is concerned. The flexural strength of the annealed graphite composites was also measured in the direction normal to pressing. Non-linear load-deflection curves were also observed, as it was the case in the pressing direction, as shown in Figure 7.22-Figure 7.25. Like when loaded in pressing direction, all the annealed graphite composites showed a catastrophic failure when loaded in the direction normal to pressing. The load-defletion curves were all non-linear. A composite containing only synthetic graphite and binder (0:80:20) was broken when an average maximum load of 61 N was applied and the average deflection of 0.17 mm was observed. The average flexural strength (σ_N) for this composite was calculated to be 7.32±2.67 MPa. The load-deflection curve for a composite containing 16 wt.% NG (16:64:20) is shown in Figure 7.23.

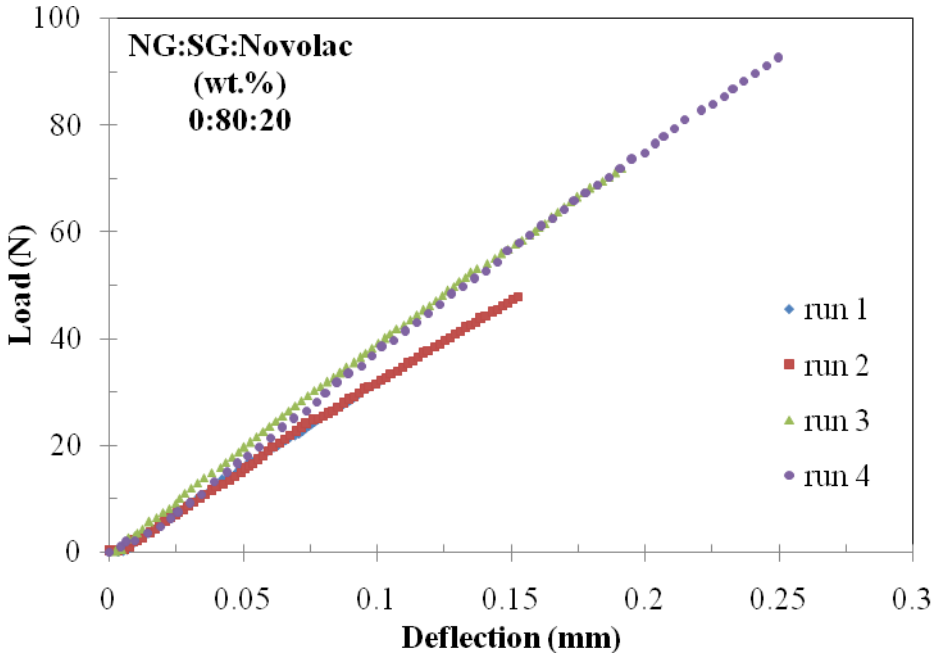

Figure 7.22: The load-deflection curves for samples of annealed graphite composite 0:80:20; the loading was done in the direction normal to pressing direction.

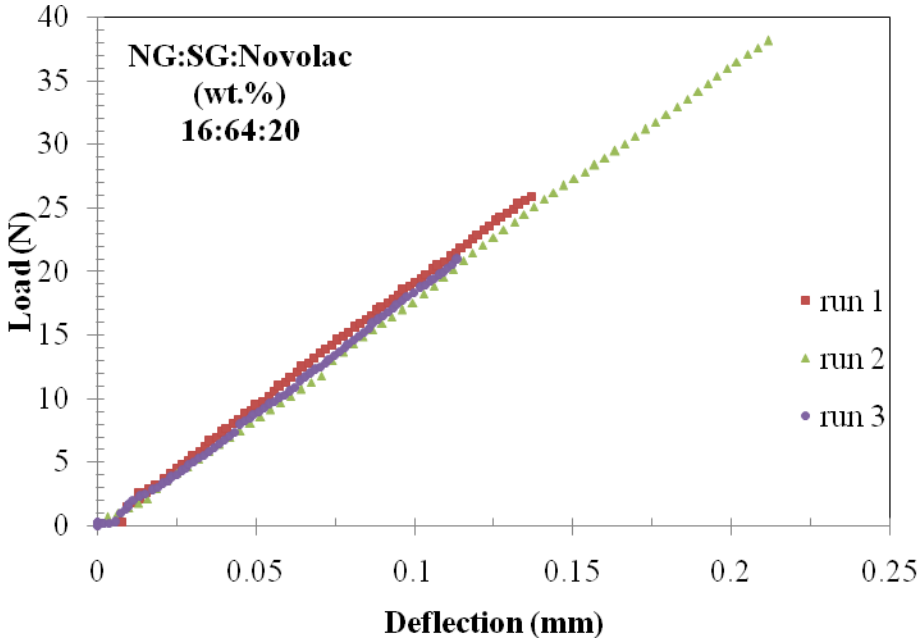

Figure 7.23: The load-deflection curves for samples of annealed graphite composite 16:64:20; the loading was done in the direction normal to pressing direction.

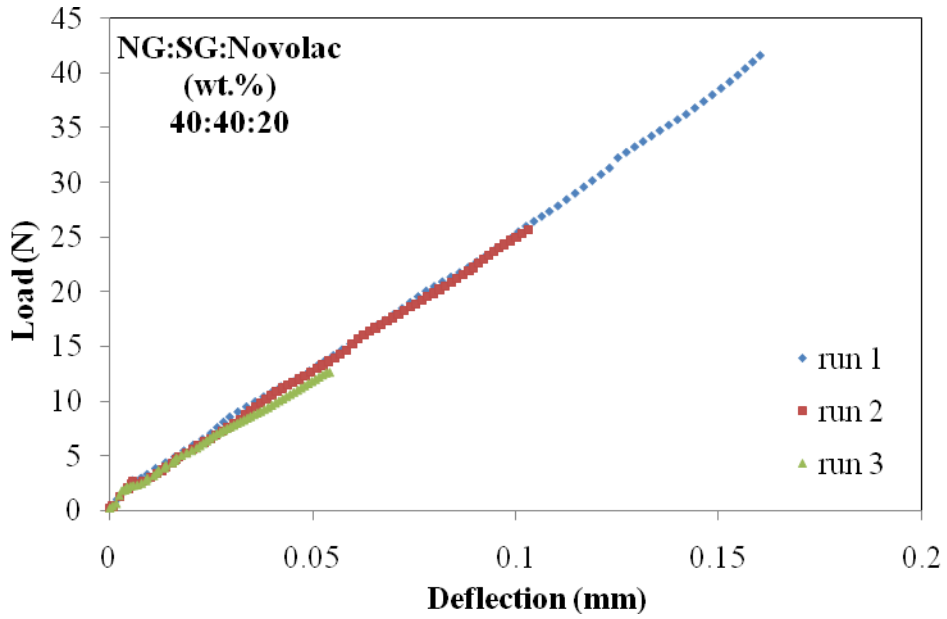

Figure 7.24: The load-deflection curves for samples of annealed graphite composite 40:40:20; the loading was done in the direction normal to pressing direction.

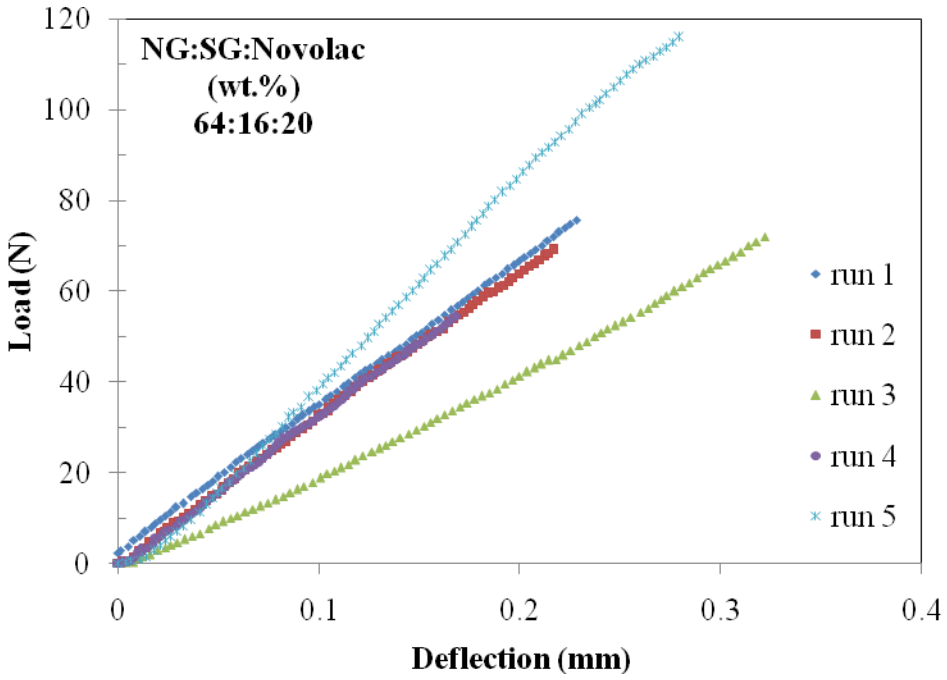

Figure 7.25: The load-deflection curves for samples of annealed graphite composite 64:16:20; the loading was done in the direction normal to pressing direction.

The average maximum load for this composite was 28.3 N and the corresponding deflection was 0.17 mm. The average flexural strength (σ_N) for this composite was calculated to be 3.39±1.04 MPa. The load-deflection curves for a composite containing equal amount of the graphite fillers are shown in Figure 7.24.This sample showed average loading capacity of 26.5 N and a corresponding average minimum deflection of 0.11 mm. This was the lowest deflection observed during the measurements. The average flexural strength value obtained in this case was 3.18±1.76 MPa. It is very interesting that as the natural graphite content in the composite increase up to 40 wt.% the strength (normal to pressing) decreases. This decrease could be attributable to the increase in stiffness resulting from the flake-like particle alignment; effectively the flakes are loaded on their edges. As such it becomes relatively easier to break the inter-particulate bond via the resin carbon in between the particles; this is consistent with literature (Heo et al., 2006). Suprisingly, a composite containing 64 wt.% NG showed the highest strength of 9.28±0.40 MPa. It also deflected more than other composites (0.25 mm), see Figure 7.25. This value is close to the one observed in the pressing direction; this was also observed for the synthetic graphite composite (0:80:20). It must be emphasized that this behavior was unexpected and the cause for this is unclear. It could be a combination of various factors, i.e. particle size effect, particle shape, degree of particle alignment, degree of crystallite orientation, the degree of inter-particulate binding, etc.

The annealed graphitic composites containing only synthetic graphite and binder (0:80:20) as well as the one containing 64 wt.% NG (64:16:20) showed to be quasi-isotropic in their observed flexural strengths. On the other hand, the composites containing 16 wt.% NG (16:64:20) and 40 wt. % NG (40:40:20) were anisotropic in flexural strengths. This could be caused by the variable degree of crystallite preferred orientation in these composites.

7.4.2 Flexural Modulus

The flexural modulus of the annealed graphite composites was calculated as the slope of the initial linear region in a stress-strain curve or as a slope of the stress-strain curve if the slope was constant in the entire curve. The stress-strain curves for the annealed graphite composites in the pressing direction are shown in Figure 7.26-Figure 7.29. The curves were generally non-linear at lower strains and became linear at higher strains. The flexural modulus was taken as the average slope obtained from each sample (called a run); the slopes were taken on the fitted data points as shown. The flexural modulli0 obtained are shown in Table 7.3.

The average flexural modulus, E_P, in the direction of pressing for a composite containing only synthetic graphite and binder (0:80:20) was 1.54±0.41 GPa. A composite containing 16 wt.% NG showed a slightly higher average flexural modulus of 1.70±0.32 GPa. This means that the stiffness of the composite increases slightly by spiking it with a minute (16 wt.%) amount of the natural graphite. However a composite having of equal amount of the filler graphites (40:40:20), had the lowest modulus value of 0.92±0.26 GPa. The observed lower modulus in this composite is understood to be caused by the fact that this composite had weaker bond between the flake-like natural graphite particles and needle-like synthetic graphite particles due to their incompatibility. This was also noted in the flexural strength measurement analysis. There could possibly be shearing during the test which would also cause a lower modulus. A composite containing 64 wt.% NG showed modulus value intermediate between the extremes with a value of 1.41±0.17 GPa. For this materials it is clear that a composite having equal amount of filler graphites is not desirable.

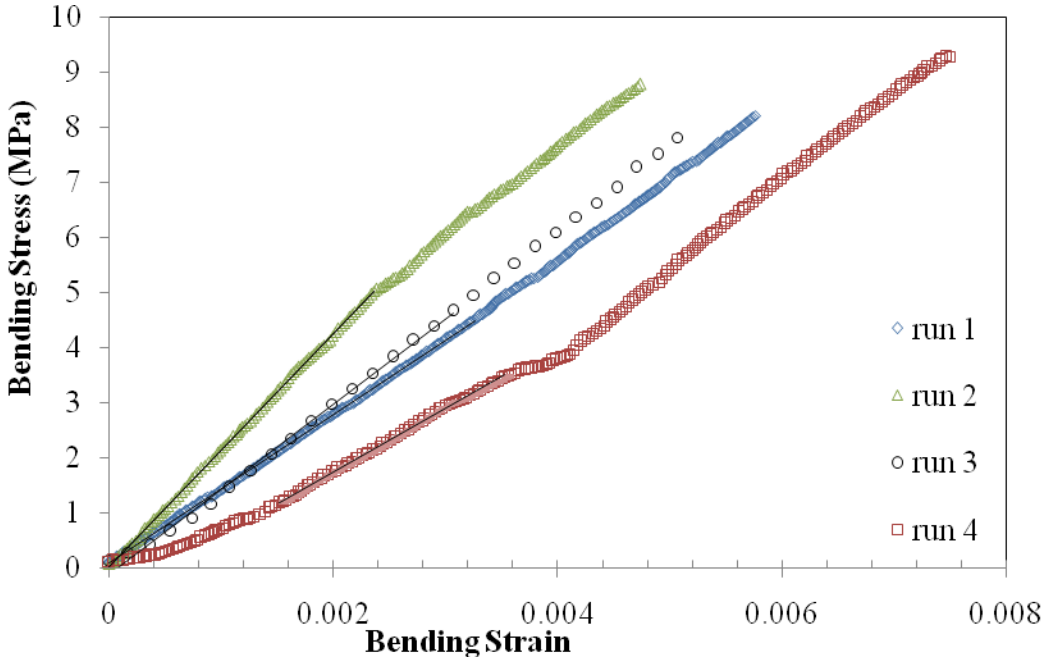

Figure 7.26: The four-point bending stress-strain curves for the annealed graphite composite 0:80:20 obtained in the pressing direction.

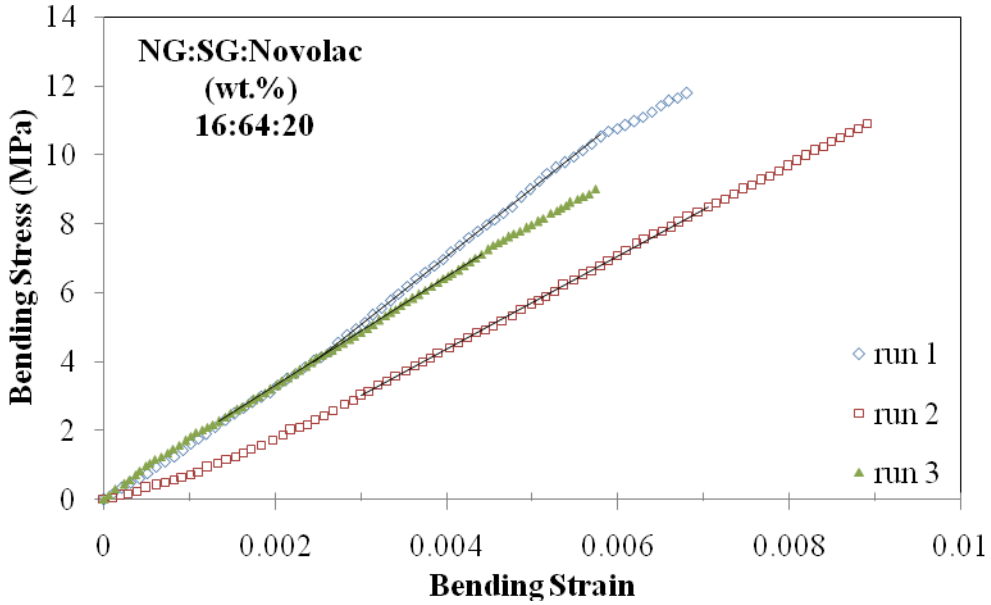

Figure 7.27: The four-point bending stress-strain curves for the annealed graphite composite 16:64:20 obtained in the pressing direction.

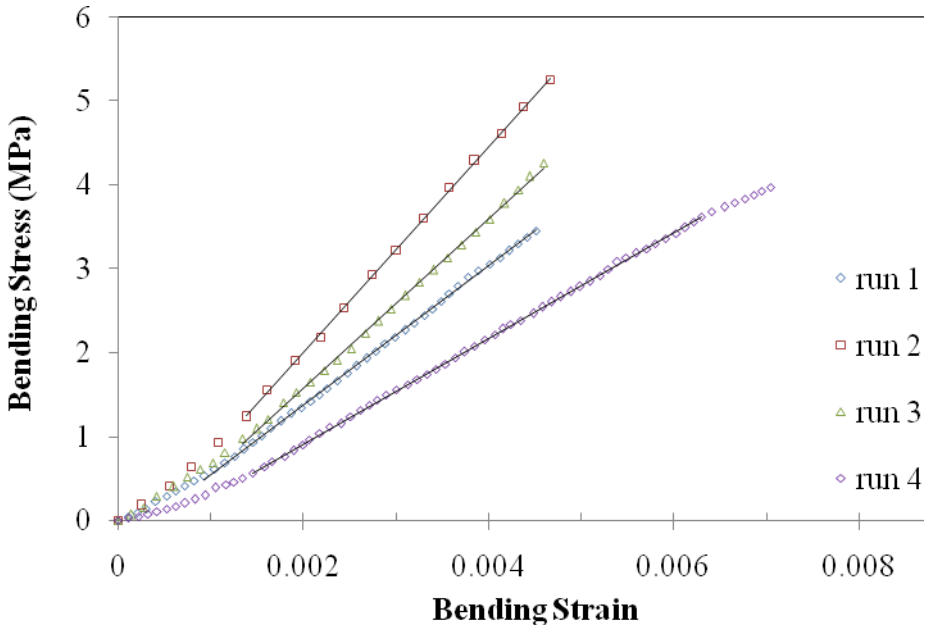

Figure 7.28: The four-point bending stress-strain curves for the annealed graphite composite 40:40:20 obtained in the pressing direction.

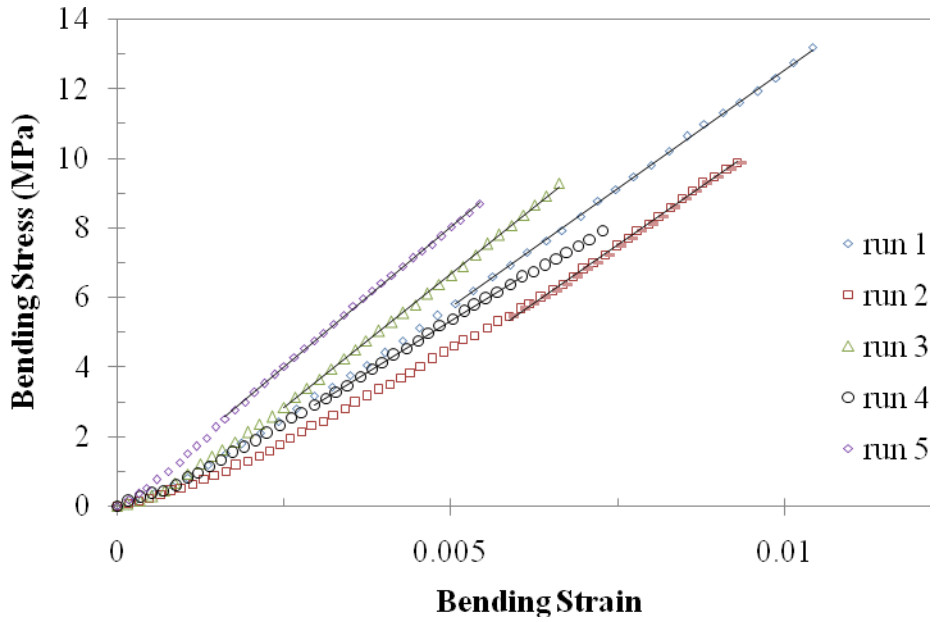

Figure 7.29: The four-point bending stress-strain curves for the annealed graphite composite 64:16:20 obtained in the pressing direction.

Table 7.4: Flexural moduli of the graphite-carbon composites annealed (in a He atmosphere) at 1800 °C for 2 hours.

Composition (NG:SG:Novolac) wt.%	**Sample or run**	**Flexural modulus, E_p (MPa)**	**Flexural modulus, E_p (GPa)**
0:80:20	run 1	1350.7	1.35
	run 2	2112.8	2.11
	run 3	1547.0	1.55
	run 4	1153.5	1.15
	Average	**1541±413.7**	**1.54±0.41**
16:64:20	run 1	1972.4	1.97
	run 2	1353.8	1.35
	run 3	1781.6	1.78
	Average	**1702.6±316.8**	**1.70±0.32**
40:40:20	run 1	828.71	0.83
	run 2	1226.4	1.23
	run 3	1010.3	1.01
	run 4	628.6	0.63
	Average	**923.5±255.1**	**0.92±0.26**
64:16:20	run 1	1365.0	1.37
	run 2	1328.0	1.33
	run 3	1542.6	1.54
	run 4	1186.0	1.19
	run 5	1613.0	1.61
	Average	**1406.9±171.5**	**1.41±0.17**

Generally the flexural moduli for these graphitic composites are very low when compared to nuclear graphites because of the fact that the bulk densities of the composites are low (1.24-1.52 $g.cm^{-3}$). The shear effect in the basal planes of the graphites and dislocation (defects) of atoms

also contribute to lower moduli observed. The observed lower moduli and strengths in the graphitic composites were due to variation in porosity, variation in the degree of particle alignment and the three phase nature of the composites.

References

BACON, G. E. (1950a) *Acta Crystallographica,* 3**,** 320.

BACON, G. E. (1950b) *Acta Crystallographica,* 3**,** 137.

BADENHORST, H., RAND, B. & W., F. W. (2010) Modelling of natural graphite oxidation using thermal analysis techniques. *Journal of Thermal Analysis and Calorimetry,* 99**,** 211-228.

BISCOE, J. & WARREN, B. E. (1942) *Journal of Applied Physics,* 13**,** 364-371.

BRAGG, W. H. & BRAGG, W. L. (1913) The structure of the diamond. *Nature,* 91**,** 557.

BROOKS, J. D. & TAYLOR, G. H. (1965) The formation of graphitising carbons from the liquid phase. *Carbon,* 3**,** 185.

BROWN, M. E. (1988) *Introduction to thermal analysis,* New York, Chapman & Hall.

BROWN, M. E. (2001) *Introduction to thermal analysis: techniques and Applications,* Dordrecht/ Boston/ London, Kluwer Academic Publishers.

CLARK, L. M. & TAYLOR, R. E. (1975a) Radiation loss in the flash method for thermal diffusivity. *Journal of Applied Physics***,** 714-719.

CLARK, L. M. & TAYLOR, R. E. (1975b) Radiation loss in the flash method for thermal diffusivity. *Journal of Applied Physics,* 46**,** 714-719.

COHN, J. G., STERN, E. W. & ETRIS, S. F. (2005) Graphite, Artificial IN KIRK-OTHMER (Ed.) *Kirk-Othmer Encyclopedia of Chemical Technology*. 5 ed., John Wiley & Sons.

CULLITY, B. D. (1978) Diffraction I: Directions of Diffracted Beams. IN COHEN, M. (Ed.) *Elements of X-ray diffraction.* Second Edition ed. Reading, Massachusetts, Menlo Park, California, London, Amsterdam, Don Mills, Ontario, Sidney Addison-Wesley Publishing Company, INC.

CUNNINGHAM, N., LEFEVRE, M., DODELET, J.-P., THOMAS, Y. & PELLETIER, S. (2005) Structural and mechanical characterization of as-compacted powder mixtures of graphite and phenolic resin. *Carbon,* 43**,** 3054-3066.

DRESSELHAUS, M. S., DRESSELHAUS, G., SAITO, R. & JARIO, A. (2004) Raman spectroscopy of carbon nanotubes. *Physics Reports,* 409**,** 47-99.

DRESSELHAUS, M. S., JORIO, A., HOFMAN, M., DRESSELHAUS, G. & SAITO, R. (2010a) Perspectives on carbon nanotubes and graphene Raman spectroscopy. *Nanoletters,* 10 751-758

DRESSELHAUS, M. S., JORIO, A. & SAITO, R. (2010b) Characterizing graphene, graphite and carbon nanotubes by Raman Spectroscopy. *Annual Review of Condensed Matter Physics,* 1**,** 89-108.

DUBOIS, J., AGACHE, C. & WHITE, J. L. (1997) The carbonaceous mesophase formed in the pyrolysis of graphitisable organic materials. *Material characterisation,* 39**,** 105-119.

EDWARDS, I. A. S. (1989) Structure in Carbons and Carbon Forms. IN MARSH, H. (Ed.) *Introduction to Carbon Science.* London, Butterworths.

FAZLUDDIN, S. (2002) Crack Growth Resistance in Nuclear Graphite *Department of Materials, School of Process, Materials Engineering.* Leeds, The University of Leeds.

FERRARI, A. C. & ROBERTSON, J. (2004) Raman spectroscopy of amorphous, nanostructured, diamond-like carbon, and nanodiamond. . *Philosophical Transactions of Royal Society A.,* 362**,** 2477-2512.

FIFIELD, F. W. & KEALEY, D. (Eds.) (1995) *Principles and Practice of Analytical Chemistry,* Glasgow, Blackie Academic and Professional.

FISCHBACH, D. B. (1971) IN PHILIP L WALKER, J. (Ed.) *Chemistry and Physics of Carbon.* New York, Marcel Dekker, INC. .

FITZER, E., KOCHLING, K. H., BOEHM, H. P. & MARSH, H. (1995) Reccomended terminology for the description of carbon as a solid. *Pure and Applied Chemistry,* 67**,** 473-506.

FRANKLIN, R. E. (1951a) *Proceedings of the Royal Society,* 209**,** 196-218.

FRANKLIN, R. E. (1951b) *Acta Crystallographica,* 4**,** 253-261.

GEIM, A. K. & NOVOSELOV, K. S. (March 2007) The rise of graphene. *Nature Materials,* 6**,** 183-191.

HACKER, P. J., NEIGHBOUR, G. B. & MCENANEY, B. (2000) The coefficient of thermal expansion of nuclear graphite with increasing thermal oxidation. *Journal of Physics D: Applied Physics,* 33**,** 991-998.

HAINES, P. J. (1995) *Thermal methods of analysis; Principles, Applications and Problems,* Glasgow, Blackie Academic and Professional.

HAYNES, R. (1927-) *Optical microscopy of Materials,* Glasgow International.

HEO, S. I., YUN, J. C., OH, K. S. & HAN, K. S. (2006) Influence of particle size and shape on electrical and mechanical properties of graphite reinforced conductive polymer composites for the bipolar plate of PEM fuel cells. *Advanced Composite Materials,* 15**,** 115-126.

HERGERT, W. & WRIEDT, T. (2012) *The Mie Theory,* Berlin Heidelberg, Springer-Verlag.

HODGKINSON, J. M. (2000) Flexure. IN HODGKINSON, J. M. (Ed.) *Mechanical Testing of Advanced Fibre Composites.* London, Cambridge: Woodhead Publishing, Ltd.

HODKIEWICZ, J. (2013) Characterizing carbon materials with Raman Spectroscopy. Madison WI, USA, Thermo Fischer Scientific Inc.

HOERNI, J. (1949) *Nature,* 164**,** 1045.

HOINKIS, E. & ROBENS, E. (1989) Surface area and porosity of unmodified graphitic matrices A3-27 and A3-3 (1950) and oxidized matrix A3-3 (1950). *Carbon,* 27**,** 157-168.

HONDA, T., SAITO, T. & HORIGUCHI, Y. (1972) *Tanso,* 72**,** 14.

HOUSKA, C. R. & WARREN, B. E. (1954) *Journal of Applied Physics,* 25**,** 1503.

HU, R. & CHUNG, T. C. (1996) *Carbon,* 43**,** 1181-1190.

HULL, A. W. (1917) *Physical review,* 10**,** 661.

IAEA (June 2012) Advances in High Temperature Gas Cooled Reactor Fuel Technology. Vienna, International Atomic Energy Agency.

IIJIMA, S. (1991) Helical microtubules of graphitic carbon. *Nature,* 354**,** 56-58.

JAGODZINSKI, H. (1949) *Acta Crystallographica,* 2**,** 298.

JIANG, W., NADEAU, G., ZAGHIB, K. & KINOSHITA, K. (2000) Thermal analysis of the oxidation of natural graphite-effect of particle size. *Thermochimica Acta,* 351**,** 85-93.

KELLY, B. T. (1981a) *Physics of Graphite,* London and New Jersey, Applied Science Publishers.

KELLY, B. T. (1981b) Physics of Graphite. London and New Jersey, Applied Science Publishers.

KELLY, B. T. & GILCHRIST, K. E. (1969) The basal thermal conductivity of highly oriented pyrolytic graphite as a function degree of graphitisation. *Carbon,* 7**,** 355-358.

KIPLING, J. J., SHERWOOD, J. N., SHOOTER, P. V. & THOMPSON, N. R. (1964) Factors influencing the graphitization of polymer carbons. *Carbon,* 1**,** 315-320.

KIPLING, J. J. & SHOOTER, P. V. (1966) Factors affecting the graphitisation of carbon: Evidence from polarised light microscopy. *Carbon,* 4**,** 1-4.

KIRK-OTHMER (2005) Graphite, Artificial. *Encyclopaedia of Chemical Technology.*

KLUG, H. P. & ALEXANDER, L. E. (1954) *X-ray procedures for polycrystalline material,* New York, Wiley.

KNOP, A. & PILATO, L. A. (1985) *Phenolic Resins: Chemistry, applications and performance.* Berlin, Heidelberg, New York,Tokyo, Springler-Verlag.

KO, T.-H., KUO, W.-S. & CHANG, Y.-H. (2001) Microstructural Changes of phenolic resin during pyrolysis. *Journal of Applied Polymer Science,* 81**,** 1084-1089.

KROTO, H. W., HEATH, J. R., O'BRIEN, S. C., CURL, R. F. & SMALLEY, R. E. (1985) C_{60}: Buckminsterfullerene. *Nature,* 318**,** 162-163.

KUDIN, N. K., OZBAS, B., SCHNIEPP, H. C., PRUD'HOMME, R. K., AKSAY, I. A. & FERRARI, R. (2008) Raman Spectra of Graphite Oxide and Functionalized Graphene Sheets. *Nano Letters,* 8**,** 36-41.

LAIDLER, D. & TAYLOR, A. (1940) *Nature,* 141**,** 130.

LEWIS, R. T. (1971) 12th biennial conference on carbon. Pittsburg, American Carbon Society.

LIPSON, H. & STOKES, A. R. (1942a) *Procedings of the Physics Society of London,* A181**,** 101.

LIPSON, H. & STOKES, A. R. (1942b) *Proceedings of the Physics Society of London.,* A181**,** 101.

MARINER, J. T. & SAYIR, H. (1999) High thermal conductivity composite and method. IN PATENT, U. S. (Ed.). United States of America, Advanced Ceramics Corporation, Lakewood, Ohio.

MARSH, H., MARTINEZ-ESCANDELL, M. & RODRIGUEZ-REINOSO, F. (1999) Semocokes from pitch pyrolysis: Mechanisms and kinetics. *Carbon,* 37**,** 363-390.

MARSH, H. & WARBURTON, A. P. (1970) Catalysis of graphitisation. *Journal of Applied Chemistry,* 20**,** 133-142.

MATSUO, H. (1980) The effect of porosity on the thermal conductivity of nuclear graphite. *Journal of Nuclear Materials,* 89**,** 9-12.

MCMILLAN, D. (1988) Von Ardenne and the scanning electron microscope. *Proceedings of the Royal Microscopy Society.*

MCMILLAN, D. (1995) Scanning Electron Microscopy 1928-1965. *Scanning,* 17**,** 175-185.

MEHNER, A.-W., HEIT, W., ROLLIG, K., RAGOSS, R. & MULLER, H. (1990) Spherical fuel elements for advanced HTR manufacture and qualification by irradiation testing *Journal of Nuclear Materials,* 171**,** 9-18.

MIAO, J.-Y., HWANG, D. W., NARASIMHULU, K. V., LIN, P.-I., CHEN, Y.-T., LIN, S.-H. & HWANG, L.-P. (2004) Synthesis and properties of carbon nanospheres grown by CVD using kaolin supported transition metal catalysts. *Carbon,* 42**,** 813-822.

MICROMERITICS (2009) Micromeritics Accupyc II 1340 Pycnometer. www.youtube.com.

MIE, G. (1908) Beiträge zur Optik trüber Medien, speziell kolloidaler Metallösungen. *Annalen der Physik,* 330**,** 377-445.

MURPHY, D. B. (2001) *Fundamentals of Light Microscopy and Electronic Imaging*.

MURTY, H. N., BIEDERMAN, D. L. & HEINTZ, E. A. (1977) Apparent catalysis of graphitisation. 3. Effect of boron *Fuel,* 56**,** 305-312.

NAKAMIZO, M., KAKKERECK, R. & P.L., W. (1974a) Laser Raman studies on carbons. *Carbon,* 12**,** 259-267.

NAKAMIZO, M., KAMMERECK, R. & P.L. WALKER, J. (1974b) Laser Raman studies on carbons. *Carbon,* 12**,** 259-267.

NICHOLLS, D. R. (2001) The Pebble Bed Modular Reactor. *Transactions of the Royal Society of South Africa,* 56**,** 125-130.

NICHOLLS, D. R. (2002) The Pebble Bed Modular Reactor. *South African Journal of Science,* 98**,** 31-35.

NIGHTINGALE, R. E. (1962) *Nuclear graphite,* London, Academic press.

NOVOSELOV, K. S., GEIM, A. K., MOROZOV, S. V., JIANG, D., ZHANG, Y., DUBONOS, S. Y., GRIGORIEVA, I. V. & FIRSOV, A. A. (2004) Electric field effect in atomically thin carbon films. *Science,* 306**,** 666-669.

PARKER, W. J., JENKINS, R. J., BUTLER, C. P. & ABBOT, G. L. (1961) Flash method of determining thermal diffusivity, heat capacity and thermal conductivity. *Journal of Applied Physics,* 32**,** 1679-1684.

PARTHASARAY, G., SREEDHAR, B. & CHETTY, T. R. K. (2006) Spectroscopic and X-ray diffraction studies on fluid deposited rhombohedral graphite from the Eastern Ghats mobile belt, India. *Current Science,* 90**,** 995-1000.

PRAWER, S. & NEMANICH, R. J. (2004) Raman spectroscopy of diamond. *Philosophical Transactions of Royal Society A.,* 362**,** 2537-2565.

PRICE, R. J. & BOKROS, J. C. (1965) Relationship between preferred orientation, thermal expansion, and radiation-induced length changes in graphite. *Journal of Applied Physics,* 36**,** 1897-1997.

RICHARDSON, J. H. (1971) *Optical Microscopy for the Materials Sciences,* New York, MARCEL DEKKER, INC.

RIND, W. (1981) Transport of fission products in matrix and graphite. IN HOINKIS, E. (Ed.) *Proceedings of a coloquim held at the Hahn-Meitner-Institut* Berlin, Germany, Hahn-Meitner-Institut fur kernforschung Berlin Gmbh.

RULAND, W. (1965) X-ray studies on the structure of graphitic carbons. *Acta Crystallographica,* 18**,** 992-996.

SCHERER, P. (1918) Bestimmung der Größe und der inneren Struktur von Kolloidteilchen mittels Röntgenstrahlen. . *Göttinger Nachrichten,* 2**,** 1.

SCHETTINO, V., PAGLIAI, M. & CARDINI, G. (2002) The Infrared and Raman spectra of fullerene C70. DFT calculations and correlation with C60. *Journal of Physical Chemistry A.,* 106**,** 1815-1823.

SCHULZE, R. E., SCHULZE, H. A. & RIND, W. (1981) Report of the Keruforschungslage Julich, Graphic Matrix Materials for Spherical HTR Fuel Elements.

SMITH, K. C. A. & OATLEY, C. W. (1955) The scanning electron microscope and its field of application. *British journal of applied physics* 6**,** 391-399.

SPRENGLING, G. R. & FREEMAN, J. H. (1950) The reaction of phenol with formaldehyde. *Journal of American Chemical Society,* 72**,** 1982-1985.

SUTTON, A. L. & HOWARD, V. C. (1962) The role of porosity in the accomodation of thermal expansion in graphite. *Journal of Nuclear Materials,* 7**,** 1897-1907.

TAMARI, S. (2004) Optimum design of constant-volume gas pycnometer for determining the volume of solid particles. *Measurement Science and Technology,* 15**,** 549-558.

TANG, C., FU, X., ZHU, J., ZHAO, H. & TANG, Y. (2012) Comparison of two irradiation testing results of HTR-10 fuel spheres. *Nuclear Engineering and Design,* 251**,** 453-458.

TANG, C., LI, Z., ZHOU, Y. & FU, X. (2008) Irradiation testing of matrix material for spherical HTR-10 fuel elements. *Nuclear Engineering and Design,* 238**,** 2886-2892.

TANG, C. H., TANG, Y., ZHU, J. G., ZOU, Y. W., LI, J. O. & NI, X. O. (2002) Design and manufacture of the fuel element for 10 MW high temperature gas-cooled reactor. *Nuclear Engineering and Design,* 218**,** 91-102.

TAYLOR, R., GILCHRIST, K. E. & POSTON, L. J. (1968) Thermal conductivity of polycrystalline graphite. *Carbon,* 6**,** 537-544.

TRUCANO, P. & CHEN, R. (1975) *Nature,* 258**,** 136.

TUINSTRA, F. & KOENIG, J. L. (1970) Raman spectrum of graphite. *Journal of Chemical Physics,* 53**,** 1126-1130.

WANG, Y., ALSMEYER, D. C. & MCCREERY, R. L. (1990) Raman spectroscopy of carbon materials: structural basis of observed spectra. *Chemistry of Materials,* 2**,** 557-563.

WARREN, B. E. (1941) X-ray diffraction in random layer lattices. *The Physical Review,* 59**,** 693-698.

WARREN, B. E. & GRINGRIICH, N. S. (1934) *Physical Review,* 46**,** 368-399.

WEBB, P. A. (2001) Volume and Density Determinations for Particle Technologists. Micromeritics Intruments Corporation.

WELHAM, N. J. & WILLIAMS, J. S. (1998) Extended milling of graphite and activated carbon. *Carbon,* 36**,** 1309-1315.

WENDLANDT, W. W. (1964) *Thermal methods of analysis,* New York, Interscience Publishers.

WOLF, R. (2001) Manufacture of bulk carbon and bulk graphite. IN B. RAND, S. P. A., M. F. YARDIM (Ed.) *Design and Control of Structure of Advanced Cabon Materials for Enhanced Performance*

Dordrecht/Boston/London, Kluwer Academic Publishers.

ZHANG, J., ZOU, Y.-W. & HE, J. (2005) Influence of graphite particle size and its shape on performance of carbon composite bipolar plate. *Journal of Zhejiang University Science,* 6A**,** 1080-1083.

ZHAO, H. S., LIANG, T. X., ZHANG, J., HE, J., ZOU, Y. W. & TANG, C. H. (2006) Manufacture and characteristics of spherical fuel elements for the HTR-10. *Nuclear Engineering and Design*, 236**,** 643-647.

CHAPTER 8: CONCLUSIONS AND FUTURE WORK

8.1 Conclusions

Model graphite-carbon composites with potential use as encasement materials in fuel pebbles were prepared by uniaxial cold compression moulding. They were prepared from mixtures of natural and synthetic graphite powders with a fixed amount (20 wt.%) of a phenolic novolac resin as binder. Analysis of the particles size distributions of the raw graphite powders and the annealed graphite composite powders showed that there was some agglomeration of particles after resin incorporation into the graphite mixtures. X-ray diffraction studies showed that the graphitic composites had hexagonal crystal structure after annealing at 1800 °C. Raman spectroscopy showed the presence of structurally disordered phase derived from the novolac phenolic resin carbon.

Optical microscopy showed different microstructures for the raw graphites and composites; the natural graphite comprised flake-like particles while the synthetic graphite consisted of needle-like coke particles as well as some fine-grained mosaics. The needle-coke particles were indistinguishable from the flakes on the micrographs of the annealed composites. The particles or flakes tend to align themselves normal to pressing direction. All the composites showed similar morphologies having compacted filler particles and very smooth surfaces. The bulk density of the annealed graphitic composites increased with the increase in the natural graphite content. A composite containing only synthetic graphite and binder (0:80:20) was the most porous of all the composites studied.

Thermogravimetric analysis studies showed that the synthetic graphite powder was more stable in air than the natural graphite powder. This was due to the presence of impurities and defects in the latter. The graphitic composites were stable in air up to 650 °C. Composites containing mainly synthetic graphite filler (0:80:20 and 16:64:20) showed lower linear coefficient of thermal expansion values than the ones containing mainly natural graphite (64:16:20 and 80:0:20) in the direction of pressing. All composites showed constant linear expansion coefficients values of approximately 2×10^{-6} K^{-1} in the direction normal to pressing. Therefore there was anisotropy in expansion observed in these composites; an anisotropic expansion ratio of at least 2.8 was observed. This anisotropy was due to alignment of particles during compression moulding.

Thermal conductivity values (in the pressing direction) of the graphitic composites decreased with increase in temperature. A composite containing only synthetic graphite and binder (0:80:20) showed smaller thermal conductivity values than other composites at any measurement temperature. This was due to its high open porosity and probably phonon scattering on crystal boundaries. It was interesting to observe that the thermal conductivity values of the composites containing compositional mirror images (i.e. 16:64:20 and 64:16:20) were similar at each measurement temperature and were higher than the ones made from each individual graphite.

The four point bending flexural strength measurements showed that a composite containing equal amount of the filler graphites (i.e. 40:40:20) had the lowest strength than all the composites in both directions. This was attributed to incompatibility of the flake-like and needle-like particles. A composite containing 16 and 64 wt.% NG showed higher bending strength values in the direction of pressing than other composites. A composite containing 64 wt.% NG showed a larger bending strength in the direction normal to pressing as well. An anisotropy in strength was

observed in the composites containing 16 and 40 wt.% NG while the other composites were quasi-isotropic. The flexural modulus data followed the same trend as the strength data. From this data it is clear that the composite containing 64 wt.% NG has the best mechanical properties.

This work demonstrated the complimentary properties of the graphite fillers in the composites. The needle-like synthetic graphite was purer, more crystalline and thermally stable in air. A composite of this graphite showed lower expansion and thermal conductivity values in the pressing direction than composites containing mainly natural graphite. This composite showed intermediate flexural strength. On the other hand, the flake-like natural graphite was less pure and thermally stable than the synthetic one. A composite made from this graphite had a larger thermal expansion coefficient and best mechanical properties than the one containing synthetic graphite. A composition having close to best properties for use in making pebbles encasement is the one containing 64 wt.% NG (64:16:20). The reason is that it satisfies most of the requirements for this application, such as high density, high thermal conductivity, high mechanical strength, high air oxidation resistance and low expansion coefficient although further densification is required.

8.2 Future Work

- It would be very interesting to study the effect of irradiation (with protons or neutrons) on the microstructure and properties of the graphitic composites studied in this work. This would provide an insight into how would the microstructure be affected and therefore how the properties would be after irradiation. That is whether or not there would be enhancement in properties? If not how are the properties deteoriating with irradiation dose or temperature?
- The effect of using other fabrication techniques (extrusion and isostatic pressing) on structure and properties is also very vital. It would be interesting to see whether the anisotropy in properties could be entirely eliminated by employing isostatic pressing.
- What effect will the use of other binders such as epoxides in making the composites have on microstructure and properties? What effects will the use of other graphite fillers from other organic sources, e.g. anthracine oil derived graphite, naphthalene derived graphite or a coal tar pitch derived graphites?
- What would the effect of densification by application of high molding pressure (>13 MPa) be on properties?